Università degli Studi di Napoli "Federico II"

**Dottorato in Tecnologie Innovative
per Materiali, Sensori e Imaging**

- 20° ciclo -

Intrinsic Josephson π-junctions
for novel devices

Karin Cedergren

Coordinatore:
Prof. Giancarlo Abbate

<u>anno accademico 2008 - 2009</u>

Table of Contents

Introduction

Complex metal oxides are a particularly interesting group of materials exhibiting a broad spectrum of intrinsic functionalities such ferroelectricity, High Critical Temperature Superconductivity (HTS), colossal magnetoresistance, and multiferroics behavior. These materials are highly interesting for basic physics and chemistry as well as for a wide range of novel applications. Their properties are easily tuned by subtle changes of doping, external pressure magnetic or electric field.

At present, for HTS, a complete microscopic theory explaining the pairing mechanism in these novel superconductors is still missing. It is instead well established that the superconductive ground state is characterized by an unconventional d-wave symmetry of order parameter. The two basic features of the d-wave symmetry, the "π" shift of the phase between orthogonal directions and the presence of nodal directions, lead to a new phenomenology, which characterizes the Josephson effect. We refer to the natural existence of Josephson π junctions, to the spontaneous nucleation of half integer flux quanta (semifluxons) in frustrated loops or at the discontinuity point between a conventional "0" and "π" junction; to the existence of an unconventional Josepshon current phase relation characterized by non-negligible high order harmonics.

Josephson junctions with a built-in π phase shift have huge potentialities for both basic studies and applications. The first prediction, that the ground state of a Josephson junction can involve a π shift, dates back to the late seventies, and refers to structures with magnetic impurities. However, it is important to point out that it is not until the discovery of HTS, that the concept of π Josephson Junctions (JJs) has been experimentally demonstrated.

In this thesis, we have used the concept of intrinsic π-Josephson junctions made of all HTS to fabricate novel devices, with new potentialities for digital and quantum superconductive electronic.

The technological feasibility of this research activity is based on a new kind of YBCO biepitaxial Josephson junctions developed at the University of Napoli (in the past years). During this thesis work the biepitaxial technique has been implemented at the University of Chalmers by using a pulsed laser technique for the deposition of thin films instead of sputtering (used in all previous works). The completely different nature of the deposition process and of the parameters involved in the two techniques has implied a huge effort for the analysis and optimization of the growth conditions.

The choice of the biepitaxial junctions for our research has been driven a) by its flexibility and b) by the unique structural and transport properties of the grain boundaries that can be fabricated.

Indeed the biepitaxial technique allows the simultaneous control of both the in-plane and the out-of-plane mutual orientation of the grains forming the junction, to engineer atomically flat junction interfaces by the proper use of vicinal cut substrates, sensibly

improving the quality of the structures. The possibility to control the junction quality at the atomic level is extremely important in HTS because of the short coherence length in these materials.

Josephson junctions with a π phase discontinuity along the barrier may have a ground state where spontaneous flux is generated at the discontinuity point [1]. This flux is quantized corresponding to half flux quanta (semifluxon). It is due to spontaneous currents originated to compensate the π discontinuity.

Semifluxons are "novel" objects in solid state physics. They are pinned at the discontinuity point and can have positive or negative polarity. A semifluxon of either polarity represents the ground state of the system and is therefore much less sensitive to fluctuations due to influence of the environment compared to ordinary fluxons in long Josephson junctions. This makes them very attractive for applications in information and storage processing in both the classical and the quantum regime. In addition their resemblance with spin 1/2 particles makes them interesting also for other purposes. The similarity between an array of semifluxons and a system of spin 1/2 particles can be possibly used as a tool to simulate and study energy bands and levels in large systems of spins.

In this thesis we have focused on the feasibility of the biepitaxial technique to study the static and dynamics properties of a semifluxon in corner like junctions. The transport properties of biepitaxial grain boundaries are strongly affected by the presence (unavoidable) of faceting at submicron and nanometer scale. The existence of 0-π facets along the grain boundary line modifies the otherwise net step-like profile of the phase along the interface. It is therefore an issue to establish if in such conditions the spontaneous nucleation of a semifluxon still occurs at the corner of 0-π-junctions.

This is a very fundamental step towards the employment of our technology in more complex designs. At present most of research on the static arrangement of semifluxon in long 0-π-JJs has been carried out by using a hybrid technology, which combines low and high critical temperature superconductors. Some aspects of the dynamics of semifluxon have been investigated by the recently developed S(I)-F (ferromagnet)-S junctions with the insulating barrier (I) introduced to reduce dissipation, and by a standard Nb-AlOx-Nb technology [2,3] ,where a pair of current injectors creates a 0-π discontinuity [4,5]. However in this last configuration, semifluxons are induced by current injection and do not represent the ground state of the system.

This thesis deals with the first combined study of static and dynamic properties of semifluxons in all YBa$_2$Cu$_3$O$_{7-\delta}$ (YBCO) HTS grain boundary junctions. We have fabricated corner 0-π-junctions by the biepitaxial technique and imaged them with Scanning Superconductive Quantum Interference Device Microscope (SSM). For these junctions, we have analyzed in details their dynamics. This study is the first which allows to correlate in an unambiguously way the new features of the dynamics of 0-π-junctions with the presence of a semifluxon (visualized by SSM) at the discontinuity point.

Outline of this thesis

The thesis consists of 8 chapters:

Chapter 1 briefly summarizes the basic properties of low and high critical temperature superconductors.

Chapter 2 gives the basis of the theory of Josephson junctions and SQUIDs for s-wave superconductors. It also analysis new Josephson based structures realized by using the d-wave symmetry of High critical Temperature Superconductors (HTS). The effect of extrinsic features, like the presence of faceting along the barrier profile in d-wave Josephson junctions, is also presented. The experimental graphs presented in this chapter refer to samples fabricated and measured during this thesis.

Chapter 3 presents a short overview of the most used methods to fabricate low and high critical temperature superconductive devices.

Chapter 4 deals with the fabrication methods used to realize the samples of this thesis. For completeness, it is also given a very short description of the morphological and structural thin film characterization techniques.

Chapter 5 presents a complete analysis of the growth of the thin film employed in this thesis and of their structural and morphological properties. The growth habits of the grain boundaries are inferred by a detailed Transmission Electron Microscopy analysis.

Chapter 6 describes an experiment meant to reveal the contribution of the large penetration depth in the c-axis direction of YBCO to the kinetic inductance of thin film. By this experiment, we have also derived the angular dependence of the London penetration depth.

Chapter 7 describes the behavior in magnetic field of the corner 0-π Josephson junction fabricated in this thesis

Chapter 8 assesses the presence of a semifluxon at the discontinuity point of 0-π Josephson junction by SSM. Here we also study new aspects of dynamics of these junctions.

Chapter	1

Brief summary of the basic properties of superconductivity

1.1 Conventional superconductivity

One of the basic properties of superconductors is the sharp transition to a non-resistive state when the sample is cooled down below a certain material-dependent temperature known as the *critical temperature* (T_c). A supercurrent, up to a certain critical value, can be transported without experiencing any resistivity.

A superconductor is not only an ideal conductor but also a perfect diamagnet. In the presence of an external magnetic field shielding currents are generated to screen the magnetic flux from the interior of the superconductor. The effect is known as the *Meissner effect*. The magnetic field can only penetrate a certain distance into the superconductor known as the *London penetration depth* (λ_L) which is material dependent.

In the superconducting state electrons with opposite spin and momentum, near the Fermi surface, form cooper pairs by interacting with the phonons (quantized vibrations) of the lattice. The length scale over which the electrons in the pair are coupled is called the coherence length ξ and can, in low temperature superconductors (LTS), be up to a micrometer. The cooper pairs forms a condensate of electrons, all occupy the lowest energy level, and the superconducting state can be described by a single macroscopic wave function. It is quantum mechanically allowed for all electrons to coexist in the lowest energy level since the net spin of the Cooper pairs is zero and they can be

regarded as bosons. The wave function (or order parameter, OP) is described by:
$\Psi(r) = |\Psi(r)|e^{i\varphi(r)}$ where φ is the phase and $|\Psi(r)|$ is the amplitude of the wave. In LTS
the wave function has the form of an S-wave. To break up a pair a finite energy is
required that is equal to the binding energy in the pair.

1.2 High Temperature Superconductors

High temperature superconductors (HTS) are copper oxide compounds. They have
perovskite structure and the center atoms in the cell differ between the various
compounds. Superconducting oxides are layered materials with an anisotropic unit cell.
The unit cell for one of the most common HTS, $YBa_2Cu_3O_{7-x}$ (YBCO), is shown in figure
1.1. The CuO_2 planes (see figure) contain mobile charge carriers and are believed to be
the source for the superconductivity. The coupling between the CuO_2-planes is quite
weak and hence the superconductivity in c-axis direction is weaker compared to ab-plane
transport. This anisotropy is clearly shown in the properties of the HTS. Generally the
carrier density in HTS is considerably lower compared to that in LTS which results in an
increased London penetration depth. Because of the anisotropy in HTS, λ_L is also highly
dependent on the direction of current transport. For screening currents flowing in the ab-
plane the penetration depth, λ_{ab}, is around 130nm [6]. This can be compared to a
penetration depth in Nb, one of the most commonly used LTS, which has a penetration
depth of 44nm. The penetration depth for YBCO for current transport in c-axis direction
is around 1 μm. Furthermore the coherence length in HTS is much shorter compared to
that in LTS. As a result thermal fluctuations become more important and defects like
impurities and grain boundaries give a larger impact on the current transport. For
comparison between the critical temperature, coherence length and London penetration
depth for some typical low respective high temperature superconductors see table 1.1
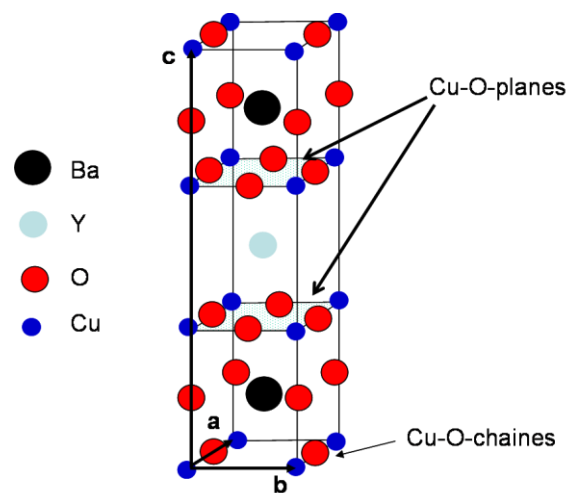
Figure 1.1:   Unit cell for $YBa_2Cu_3O_{7-\delta}$

The microscopic origin of the superconducting phenomena in HTS is not yet fully understood, but it is well established that the OP has an unconventional symmetry. After being an issue of discussion for more than a decade it is by now unambiguously determined by a number of phase sensitive experiments that the shape of the OP is predominantly d-wave. The energy gap varies in k-space according to:

$\Delta(k) = \Delta_0 (\cos(k_x a) - \cos(k_y a))$, which corresponds to a wave function with four lobes in orthogonal directions and nodal lines at 45º angle with respect to the lobes (see figure 1.2). In addition there is a phase changes of π between adjacent lobes. The lobes of the OP are oriented with the a and b directions of the CuO_2 planes. A discussion whether there is a complex subdominant s-wave OP (allowed by symmetry reasons) is still ongoing.

Material	T_c [K]	λ [nm]	ξ [nm]
LTS:			
Al	1.175	50	1600
Pb	7.19	39	83
Nb	9.25	44	40
HTS:			
YBCO	93	130	1.5
(La/Sr)CuO_4	36	100	2.5

Table 1.1: Critical temperature, London penetration depth and coherence length for some common superconductors. For the high temperature superconductors the value for the penetration depth and coherence length for current transport in the *ab*-planes has been given
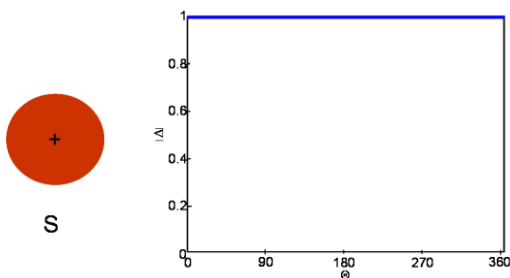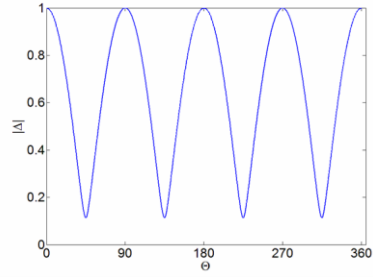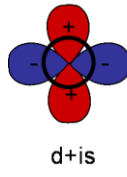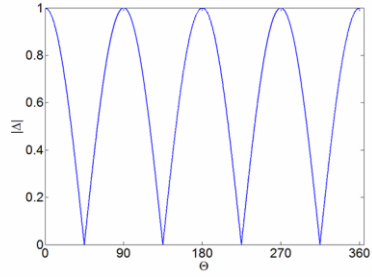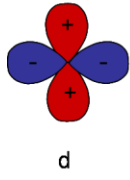
Figure 1.2: s-wave, d-wave and d+is-wave OP respectively.

Chapter 2

General Theory of Josephson Junctions

2.1 The Josephson effect

2.1.1 Conventional Josephson junctions

A Josephson junction (JJ) consists of two superconducting electrodes separated by a thin barrier of a non superconducting material. If the barrier is thin enough a supercurrent can be carried across the junction from one superconducting electrode to the other. The current depends on the phase difference between the electrodes according to [7,8,6]:

$$I_s = I_c \sin \varphi \qquad \qquad 2.1$$

Here φ is the difference between the phase of the order parameters in the two electrodes and I_c , the *critical current*, is the maximum current that can flow through the junction without dissipation. The evolution of the phase difference across the junction as a function of time is given by the expression:

$$\frac{\partial \varphi}{\partial t} = \frac{2e}{\hbar} V \qquad \qquad 2.2$$

Equation 2.1 and 2.2 are referred to as the *Josephson dc effect* and *ac effect* respectively and the device has gotten its name after Brian Josephson who predicted such a behavior in 1963. One year later it was experimentally verified by Anderson and Rowell.
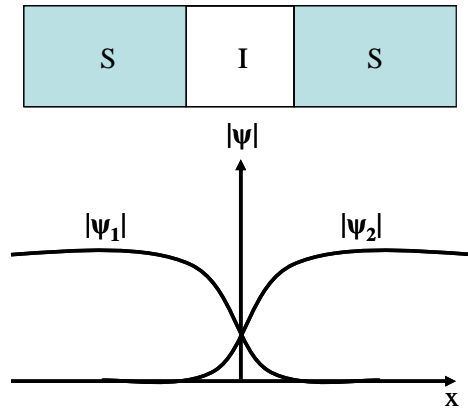
Figure 2.1:   (a) The simplest form of a Josephson junction, two superconductors are separated by a thin insulator. (b) Overlap of the wave functions across the junction

2.1.2 Pi-junctions

With the discovery of the cuprate superconductors it became possible to introduce an additional "intrinsic" phase shift of π across the junction (it should be noted here that also in LTS junctions an intrinsic phase shift can be added by using a ferromagnetic barrier [9-11]). If an additional phase shift of π is present in the junction the dc Josephson effect becomes:

$$I_s = I_c \sin(\varphi + \pi) = -I_c \sin \varphi \qquad\qquad 2.3$$

It is worth noting that this expression is equivalent to the current flowing in the opposite direction across the junction. In figure 2.2 the two types of junctions are shown. To the right a conventional "0-junction" and to the left a "π-junction" with an additional phase shift of π due to the orientation of the order parameters.
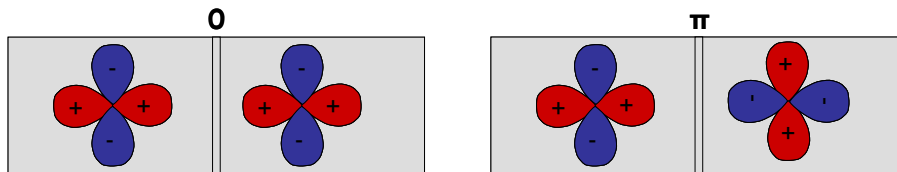
Figure 2.2:   In a 0-junction (left) the phase shift across the junction is characterized by the overall phase shift φ. In a π-junction (left) there is an additional phase shift across the junction due to tunneling between lobes of different sign. The resulting phase difference is the overall phase shift plus π, $\varphi+\pi$.

2.1.3 Second harmonic in the current phase relation

The first Josephson equation originates from the more general Fourier expansion of the current phase relation across the junction:

$$I_s(\varphi) = \sum_{n \geq 1} I_{c_n} \sin(n\varphi)$$

2.4

In its simplest form corresponds to the formula given by equation 2.1, but for some special cases more than the first harmonic has to be considered. For superconductors with a d-wave OP the second harmonic has to be taken into account for certain orientations of the OPs, i.e. when the OP is oriented so that current transport occurs simultaneously from two lobes of different sign. This may happen in junctions where the order parameter of one electrode is rotated 45° with respect to the other. For this junction configuration it has been shown that Josephson current phase relation assumes the form [12-14][15] :

$$I_s = I_{c1} \sin \varphi - I_{c2} \sin 2\varphi$$

2.5

2.2 RCSJ-model

From the Josephson equations it is easily shown that a Josephson junction works as a nonlinear inductance. The derivative with respect to time of equation 2.2 gives:

$$\frac{dI}{dt} = I_c \cos\varphi \frac{d\varphi}{dt}$$

2.6

Substituted into equation 2.1 and rearranged we arrive at the expression:

$$V = \frac{\hbar}{2eI_c \cos\varphi} \frac{dI}{dt}$$

2.7

which shows that the junction acts like an inductor with the inductance:

$$L_J = \frac{\hbar}{2eI_c \cos\varphi}$$

2.8

11

A way to model the behavior of a Josephson junction is to include a resistor and a capacitor in parallel with the junction. This circuit is often referred to as the RCSJ model (resistively and capacitively shunted junction model) and consists of lumped elements as building blocks (see fig 2.3).

The resistor accounts for the dissipation due to quasiparticles in the finite voltage regime and the capacitor is related to the dielectric nature of the barrier. An additional contribution to the capacitance can arise from the capacitance between the electrodes and the substrate. In specific cases (for example devices built on substrates with high dielectric constant) such a contribution to the total capacitance can play an important roll.
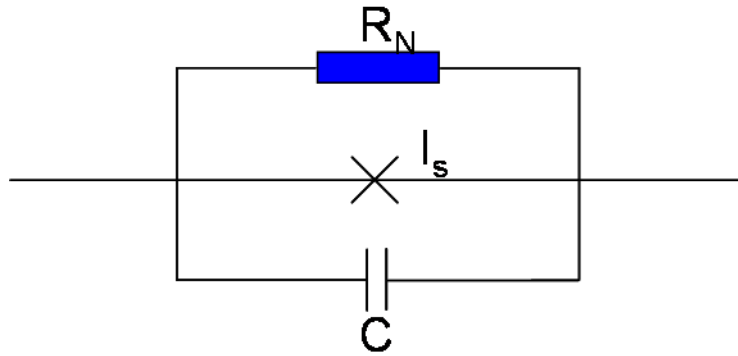
Figure 2.3:   RCSJ-circuit with lumped element to model a Josephson junction. The resistor represents the normal state resistance R_N of the junction. The capacitor accounts for the capacitance across the junction as well as stray capacitances between the junction and the substrate.

The total current through the device can be written:

$$I_{bias} = I_s(\varphi) + \frac{V}{R_N} + C\frac{dV}{dt} \qquad 2.9$$

By expressing V as $\hbar/2e \cdot d\varphi/dt$ (second Josephson equation) and substituting it in 2.9 the equation can be written as a second order differential equation with respect to the phase:

$$I_{bias} = I_s \sin\varphi + \frac{\hbar}{2eR_N}\frac{d\varphi}{dt} + \frac{\hbar C}{2e}\frac{d^2\varphi}{dt^2} \qquad 2.10$$

Equation 2.10 has a close analogy with the equation of motion of a particle moving in a washboard shaped potential given by:

$$U(\varphi) = -E_J \cos\varphi - \frac{\hbar I}{2e}\varphi \qquad\qquad 2.11$$

$E_J = (\hbar/2e)I_c$ is the *Josephson energy* and $E_J \cos\varphi$ is the *coupling energy* for the system. The particle is represented by a "phase particle" with "mass" $M_\varphi = (\hbar/2e)^2 C$ subjected to a drag force according to: $-(\hbar/2e)^2(1/R)(d\varphi/dt)$. The mechanical analogue with the phase particle moving in the washboard potential is illustrated in figure 2.4.
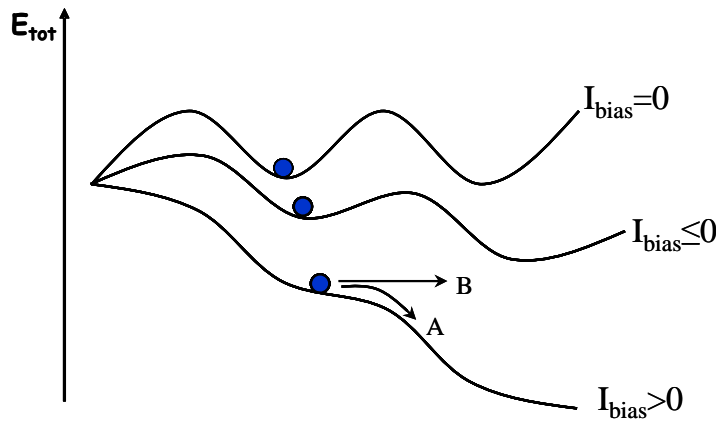
Figure 2.4:   The phase particle moving in a washboard potential. When the bias current exceeds the critical current the junction enters the running mode. The trajectory of the particle depends on the dissipation. If the dissipation is high the particle suffers from energy losses and follows the trajectory pointed out by the arrow A.

The position of the particle in the mechanical analog is associated with the phase difference, the velocity with the voltage, the mass with the capacitance, viscosity with the conductance, and the tilt of the washboard with the bias current.

When the bias current is increased from zero the tilt and shape of the washboard is changed as seen in figure 2.4. When the bias current exceeds the critical current the phase particle starts to move along the potential with a trajectory defined by the dissipation of the system. It is common to introduce the dimensionless *Stewart-McCumber parameter* also referred to as the *damping parameter*, $\beta_C = 2eI_c R_N{}^2 C/\hbar$. The Stewart-McCumber parameter is proportional to the quality factor, $Q = \sqrt{\beta_C}$ of the junction which in turn corresponds to the dissipation, $\alpha = 1/Q$. In the mechanical analogue β_C corresponds to the damping of the particle moving in the potential.

2.2.1 Over-damped junctions

If $\beta_C \ll 1$ the junction is called over-damped and the capacitance can be neglected and equation 2.10 reduces to:

$$I = I_c \sin\varphi + \frac{\hbar}{2eR_N}\frac{d\varphi}{dt}$$

2.12

When the bias current is much larger than the critical current, the superconducting part can be neglected compared to the current passing through the resistor and the current voltage curve, *IV curve*, looks similar to the one for a normal resistor. For smaller currents where the contribution from the sinusoidal supercurrent is no longer negligible the current voltage characteristics can be obtained by integrating equation 2.12. The resulting equation is given by:

$$\langle V \rangle = R_N \sqrt{I^2 - I_c^2}$$

2.13

where $\langle V \rangle$ is the d.c voltage obtained by considering the time average of the phase φ solution of equation 2.12 [16].
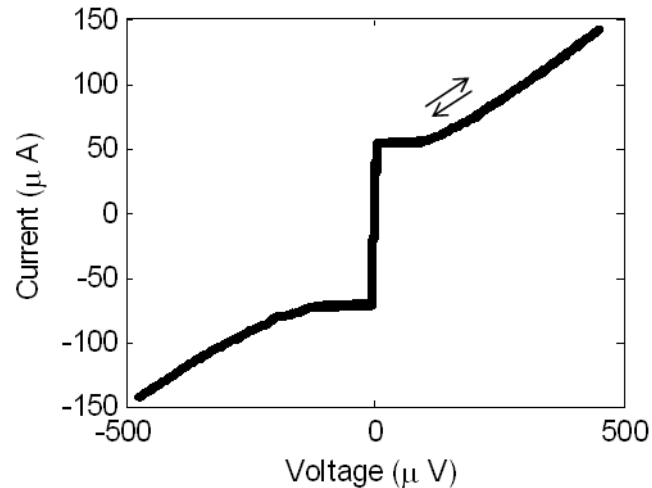
Figure 2.5:   Non-hysteretic IV-curve of an over-damped current biased junction.

In the mechanical analogue, when I=0, i.e. no current is sent through the junction, the shape of the washboard potential is similar to the one depictured on top of figure 2.4. The phase particle is trapped in a minimum of the potential. By increasing the current the potential is tilted more and more, but for currents I< I_c the phase particle is still trapped in

a local minimum (here we are neglecting the thermal fluctuations which may kick the particle out of the minimum for $I \le I_c$). This corresponds to the superconducting state where no voltage is generated across the junction. When the bias current exceeds the critical current the particle will escape from the local minimum and start to roll down the slope. This state corresponds to the so called running state where a voltage ($V = \hbar/2e \cdot \dot{\varphi}$) is generated across the junction.

When the dissipation is high the particle moves along the trajectory given by the arrow A in figure 2.4. Due to the dissipation it loses energy. When the bias current is reduced to the critical current the particle will be trapped in a new potential minimum.

2.2.2 Under-damped junctions

If $\beta_C \gg 1$ the junction is referred to as under-damped. In this case the capacitance is too large to be neglected and to obtain the relation between the averaged voltage and the applied current equation 2.10 has to be solved numerically.

Instead a qualitative understanding can be obtained by using the mechanical analogue. If the bias current increase from zero and exceed the critical current the phase particle follows a trajectory similar to the one indicated by B in figure 2.4. The result is an abrupt switch to the running state. To go from the running state back to the non-resistive state the tilt of the potential has to be such that the trajectory of a particle starting from the maximum of one potential well (point 1 figure 2.6) hits the following well near the top. The total energy of the particle is given by the initial energy minus the dissipated energy. For low dissipations the particle will not re-trap until the bias current reaches a value much smaller than the critical current (see figure 2.6). The result is an IV-curve with hysteresis as seen in figure 2.7.
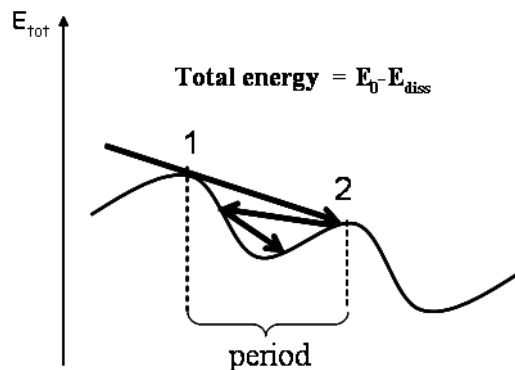
Figure 2.6:   A phase particle re-trapping into a local minimum. For low dissipation the re-trapping occur at a bias current lower than the critical current resulting in a hysteretic curve. Larger hysteresis in the IV curve corresponds to lower dissipation.
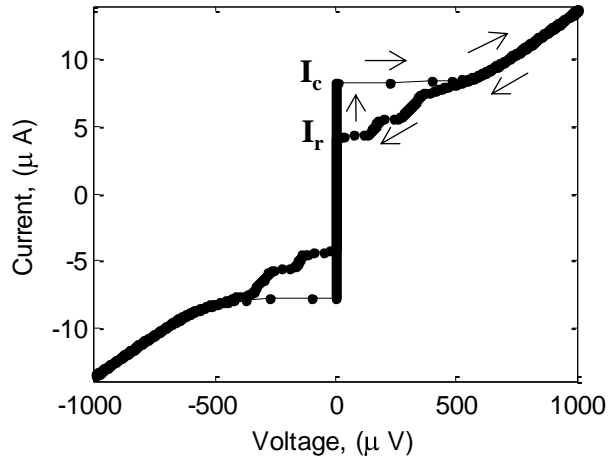
Figure 2.7:   Hysteretic IV-curve for an underdamped current biased junction. The
               junction is a HTS junction fabricated with the biepitaxial technique. (The
               step like resonances in the retrapping current are LC resonances)

The retrapping current is inversely dependent on the quality factor and is given by the
expression:

$$I_R \approx \frac{4I_c}{\pi Q} \qquad \qquad 2.14$$

It is possible to estimate β_C from the hysteresis of the IV-curve by using the *Zappe
approximation*:

$$\beta_C \approx \frac{2 - (\pi - 2)I_R/I_C}{(I_R/I_C)^2} \qquad \qquad 2.15$$

2.3 Josephson Effect in the presence of an external magnetic field

2.3.1 Conventional junctions

The response of a Josephson junction to an external magnetic field is an important tool
for applications of the Josephson effect. In a similar way as a superconductor screens the
magnetic field the junction screens the field from its interior. The field will only penetrate
a certain distance into the junction given by the Josephson penetration depth:

16

$$\lambda_J = \sqrt{\frac{\Phi_0}{2\pi\mu_0 dJ_c}}$$
2.16

here d is the magnetic thickness of the junction which is the sum of the barrier thickness and the London penetration depth on each side (see figure 2.8). The width of the junction with respect to the Josephson penetration depth determines the "magnetic length" of the junction. It's an important measure since it rules how the junction responds to an external magnetic field. If the length of the junction, L, is shorter than the penetration depth i.e. $L < \lambda_J$, the magnetic field will penetrate the junction area in a uniform way. If instead the junction is magnetically long, $L > \lambda_J$, fluxon dynamics starts to play an important role [16]. The Josephson penetration depth depends both on the critical current density and London penetration depth. Both properties vary with crystal orientation for the HTS Josephson junctions. The Josephson penetration depth can therefore vary substantially also between junctions with the same dimensions.

An external magnetic field will modulate the phase shift across the junction and introduce a phase gradient. The phase shift across the junction depends on the field and the position according to:

$$\varphi(x) = \frac{2\pi d}{\Phi_0} Hx$$
2.17

Here d is the "magnetic" thickness of the junction (see figure 2.8), H is the external magnetic field and x is the position along the junction. The expression is derived by integrating the generalized London equation [17], $\vec{\nabla}\varphi = \Lambda \vec{J}_s + (2\pi/\Phi_0)\vec{A}$, around the contour shown by the dashed line in figure 2.8. Here $\vec{J}_s$ is the screening currents generated by the magnetic field with vector potential $\vec{A}$, $\Phi_0 = 2.07 \cdot 10^{-15} W/m^2$ is the flux quantum and $\Lambda = m/\rho e\hbar$ where m is the mass of the electron and ρ the density of the Cooper pairs. The integration path is chosen well inside the superconductor where the supercurrents are zero.
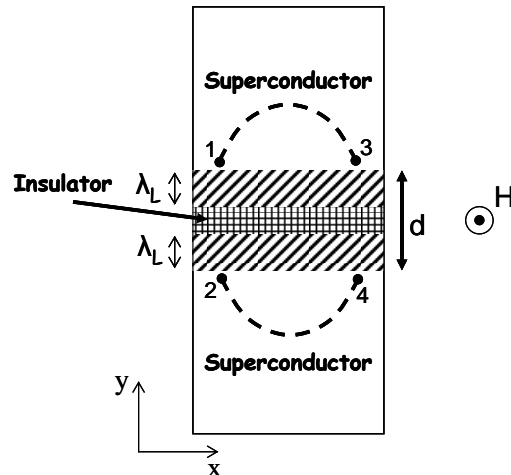
Figure 2.8:   Josephson junction consisting of two electrodes separated by an insulating
               barrier. The magnetic thickness, d, is represented by the thickness of the
               insulator plus the London penetration depth, λ_L, on each side. The
               integration path is marked by the dashed line in the figure.

If 2.17 is substituted into the first Josephson equation for the current density and
integrated across the area of the junction (the junction is here considered to be rectangular
with a uniform current density) one obtain the following expression for the critical
current:

$$I_c = I_c(0)\left|\frac{\sin(\pi\Phi/\Phi_0)}{(\pi\Phi/\Phi_0)}\right|$$
2.18

Φ is the flux through the junctions magnetic area $w(2\lambda + d)$, where w is the width of
the junction. Equation 2.18 is plotted in figure 2.9. The obtained pattern is equivalent to
the diffraction pattern for light through a narrow slit, the *Fraunhofer pattern*.
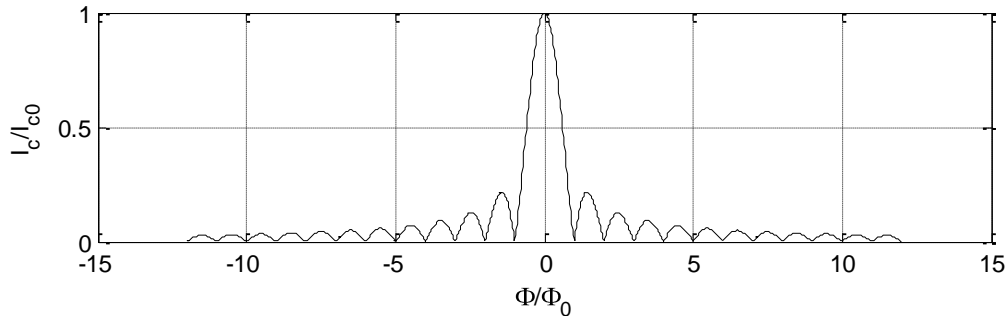
Figure 2.9:   Critical current as a function of the applied magnetic flux for an ideal
               junction with rectangular cross section area, uniform current distribution
               and no intrinsic phase shift.

It should be noted here that the expression in 2.18 is valid only for junctions with a
uniform current distribution. For junctions with a non-uniform current distribution, which
is the most common situation in HTS Josephson junctions (JJ), one has to make a
difference between magnetically short and long junctions. In short junctions the
Fraunhofer pattern will be modified when the current density is not uniform but it will
remain symmetric for positive and negative applied fields around a mirror plane through
H=0. In long junctions effects due to the self field generated by the Josephson current
becomes important and the symmetry is lost. For such junction it is not possible to get an
analytical expression of I_c(B). In this case the equation $J = J_c \sin\varphi(x)$ has to be
numerically integrated over the junction area with the appropriate boundary conditions
which depend on the specific geometry employed [16].

18

2.3.2 Junctions with intrinsic phase shifts

If an additional phase shift of π is added to the junction the pattern will be exactly the same since the physical situation is just that the direction of the current in the junction is reversed. By introducing a somewhat more complex situation where half the junction experience an additional phase shift of π while the other half doesn't, we have created a so called 0-π-junction (in contrast to the "regular" junction described above that in this nomenclature is referred to as a 0-junction). The d-wave OP in the cuprates provides an excellent opportunity to fabricate such junctions. In a 0-π-junction the extra phase shift in half of the junction has to be taken into account. As a result the critical current as a function of the magnetic field will become:

$$I_c = I_c(0)\left|\frac{\sin^2(\pi\Phi/\Phi_0)}{(\pi\Phi/2\Phi_0)}\right| \qquad 2.19$$

The phase shift across the junction as a function of position, x, along the barrier and the plot of the corresponding $I_c(B)$ pattern (equation 2.19) is shown in figure 2.10. Note that there is a minimum in critical current for zero magnetic field.

(a)

(b)

19
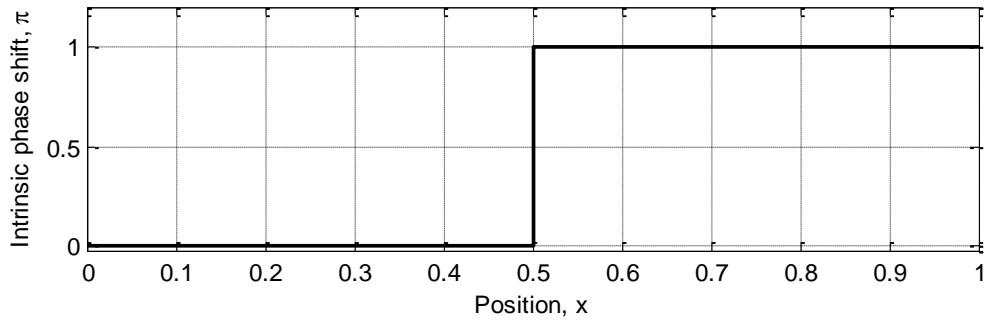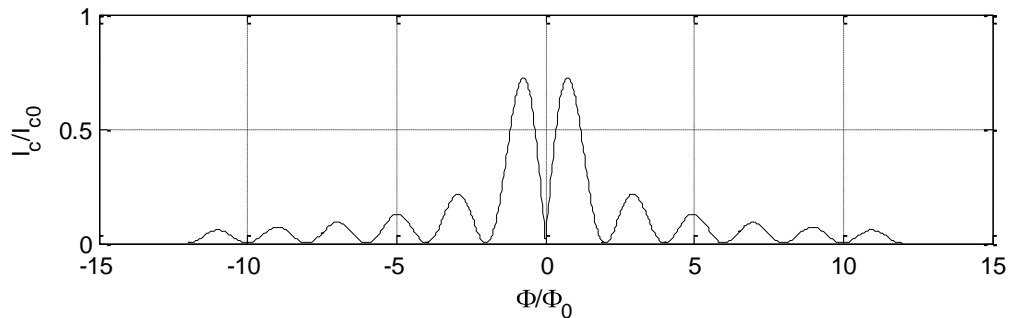
Figure 2.10:   (a) Intrinsic phase shift across the junction as a function of position. (b) Critical current as a function of the applied magnetic flux for an ideal 0-π-junction with rectangular cross section area, uniform current distribution and equal length for the 0-part and the π-part. Note that in this case the critical current present an absolute minimum for a zero external field in contrary to fig 2.9.

0-π-junctions created between s-wave and d-wave superconductors were used in the early stage of HTS as a tool to determine the symmetry of the OP. Figure 2.11a shows a sketch of such a corner junction used in a well known experiment by van Harlingen et al [18].

In the work presented in this thesis both electrodes in the 0-π-junctions are made of HTS materials. To achieve a 0-π junction, the OP in one of the two electrodes should be rotated with respect to the other only for a part of the barrier. The sketch in figure 2.11b illustrates a typical all HTS junction where the different orientations of the OP are obtained by choosing different crystal orientation for the two electrodes. Such an approach is not trivial and requires a complicated fabrication method involving epitaxial thin film growth on a substrate with appropriate lattice parameters. The procedure is described in further details in chapter 3 and 4.

(a)   **(b)**
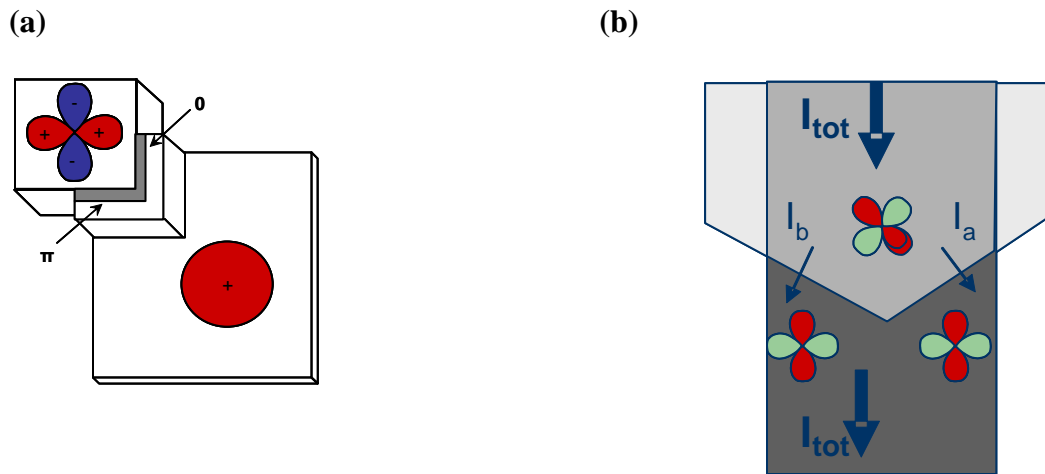
Figure 2.11:   (a) Corner shaped 0-π-junction between HTS and LTS. This type of superconductor was used to probe the symmetry of the OP in the early stages of HTS. (b) An all HTS 0-π-junction. Note that the OP on one side has to be rotated with respect to the OP on the other side in order to create a junction with a 0-π discontinuity of the phase.

2.3.3 Arbitrary π facets in a JJ

In real HTS junctions the barrier interface is not straight, there will always be a certain amount of faceting. Such microfacets may induce phase shifts along the junctions and as a result the $I_c(B)$ pattern will deviate from the ideal situations presented in previous paragraphs. In the following figures the Ic(B) pattern corresponding to different configurations of 0 and π facets are shown:

(a)

(b)

(c)
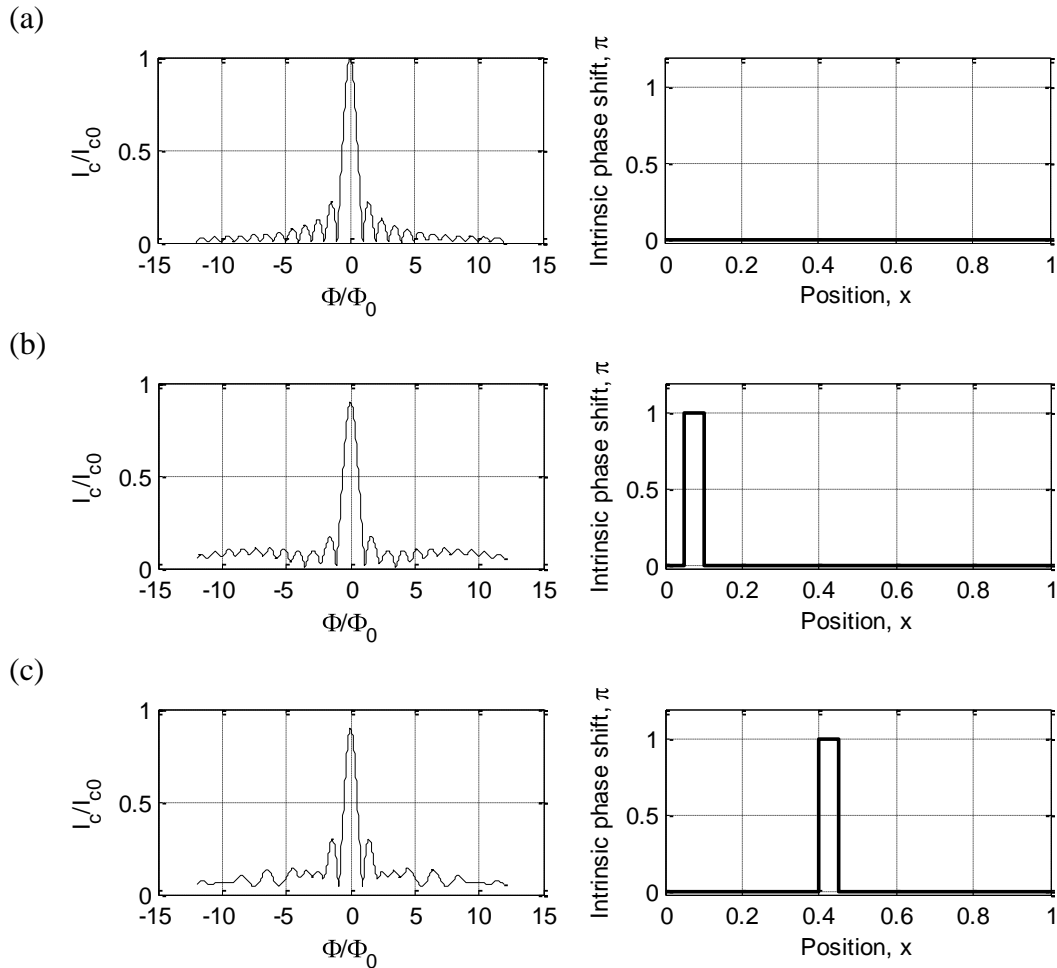
Figure 2.12:   Example of how a single π-facet changes the Fraunhofer pattern of a 0-junction. Note also the influence of the position of the π-facet on the resulting magnetic pattern.

(a)

(b)

(c)
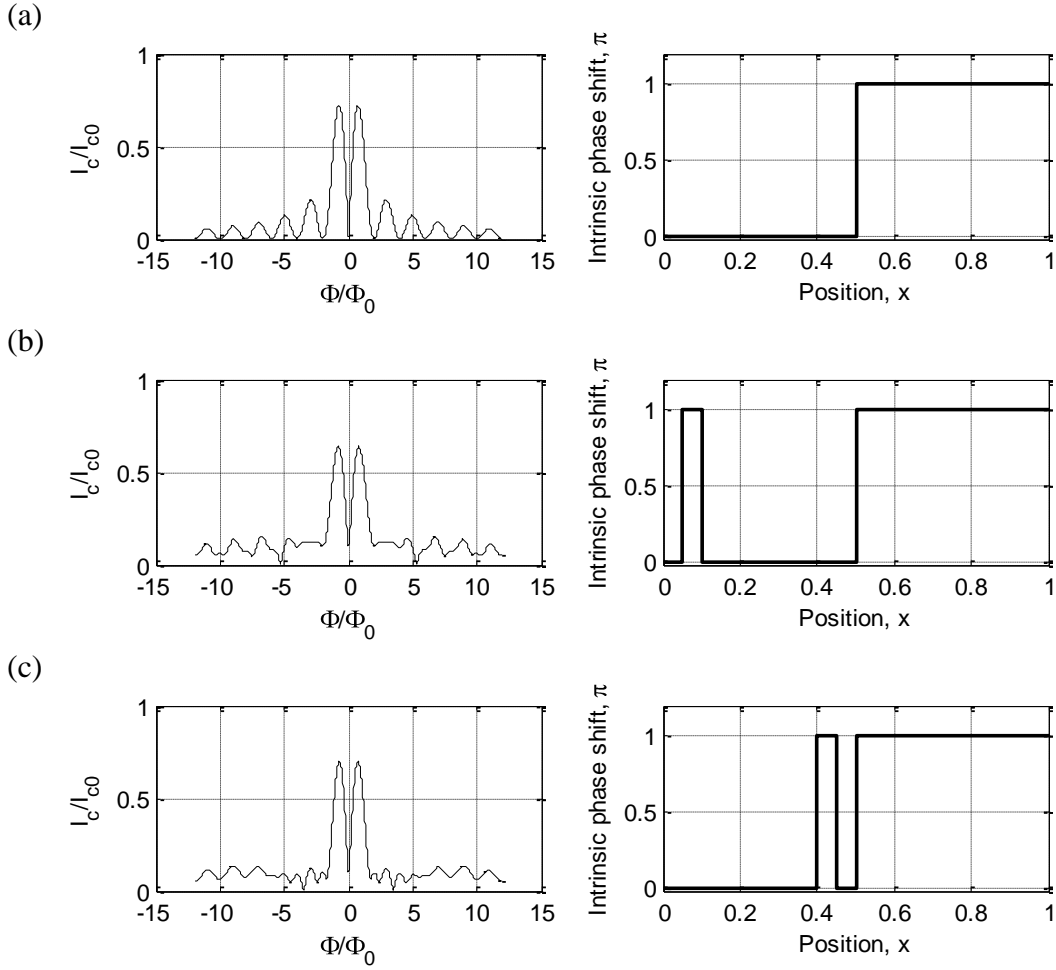
Figure 2.10:   (a) An ideal 0-π-junction. (b) and (c) show how a single π facet on the 0-side changes the ideal magnetic pattern
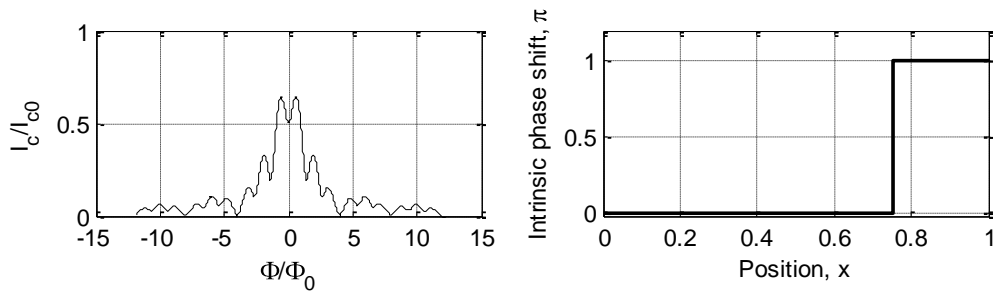
Figure 2.14:   A non uniform 0-π-junction where the π-facet is considerably shorter than the 0-facet

(a)

(b)

(c)

(d)
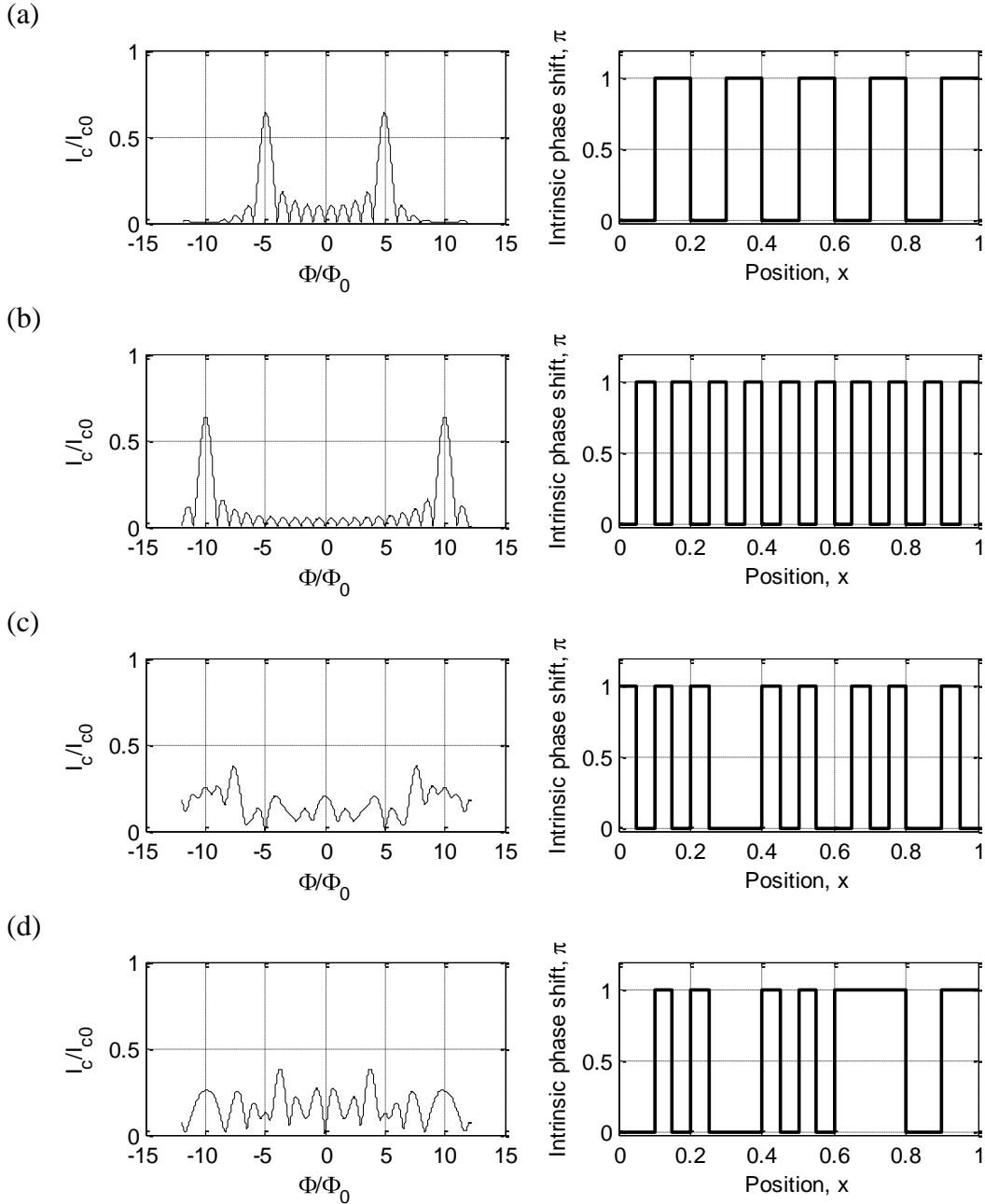
Figure 2.15: A regular faceting typically reduces the central lobes and produces larger peaks at the sides (a) and (b). The number of facets determines the distance between the larger side lobes. In (c) a 0-junction with random faceting is shown and in (d) a 0-π-junction with random faceting. From figure (d) it is clear that as long as there is a majority of π-facets on one side and 0-facets on the other the junction will preserve its 0-π-behaviour of the magnetic pattern with a local minimum at zero magnetic field.

2.3.4 Long 0-π-junctions

The magnetic patterns for the 0-π-junctions in previous paragraphs have been considering magnetically short junctions. The depth of the minimum in the critical current at zero magnetic field is reduced by increasing the magnetic length of the junction. Figure 2.16 shows the critical current as a function of the field for different values of L/λ_J where L is the length of the junction and λ_J is the Josephson penetration depth. The figure has been retrieved from Kirtley et al [19].
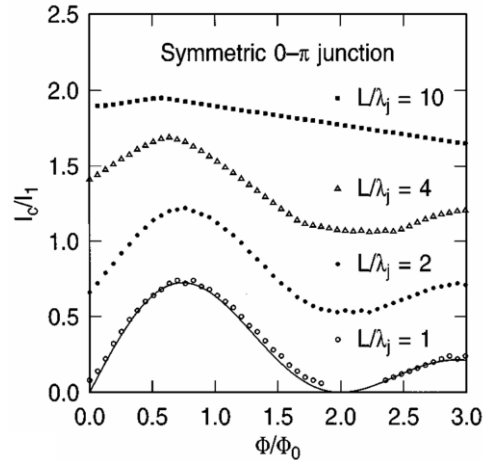
Figure 2.16:   Critical current as a function of magnetic field for symmetric 0-π-junctions of different length. Note the flattened shape of the curve for larger values of L/λ_J.

2.3.4 Semifluxons in 0-π-junctions

In paragraph 2.3.2 it was shown that the intrinsic phase difference across the junction for a 0-π-junction had a discontinuity point where it changed from 0 to π. The effect on the I_cB pattern in the short junction limit was a minimum in critical current for zero magnetic field. It was also shown that for long junctions the characteristic 0-π-behaviour changed into a pattern more similar to that for conventional 0-junctions but with a flattened main lobe. For 0-π-junctions with $\lambda_J > L$ the ground state of the system is characterized by the presence of spontaneous flux at the discontinuity point. The flux is quantized and takes the value of half a flux quantum [20]. The observation of semifluxons in frustrated Josephson systems like 0-π-junctions or superconducting loops interrupted by an odd number of π-junctions is one of the most striking evidence of the d-wave symmetry in HTS [21].

2.3.5 Influence of the faceting on the critical current.

In paragraph 2.3.3 the influence of π-facets was described. However, also facets with a small deviation from the nominal interface, that do not necessarily introduce a π-shift along the barrier, play a role. Tunneling between two lobes gives a higher critical current than tunneling into a node. It can be shown that for an arbitrary mis-orientation angle between the OPs of the two electrodes, the critical current density of an all d-wave junction can be written [22]:

$$J_c = J_{c0}(n_x{}^2 - n_y{}^2)_L (n_x{}^2 - n_y{}^2)_R \sin\varphi \qquad 2.20$$

where J_c is the maximum critical current density and n_x and n_y are the projections of the unit vector n onto the crystallographic axes in the right (R) and left (L) electrode respective and φ is the phase difference across the junction. It turns out that the angular dependence of the order parameter has a large influence on the current and has to be considered for devices made of cuprate superconductors. On one hand it provides an additional tool for tuning the critical current besides geometric scaling of the junctions, On the other hand the presence of microfaceting along the barrier will result in a non uniform current density distribution.

2.4 Superconducting Quantum Interference Device (SQUID)

2.4.1 Conventional d.c-SQUID
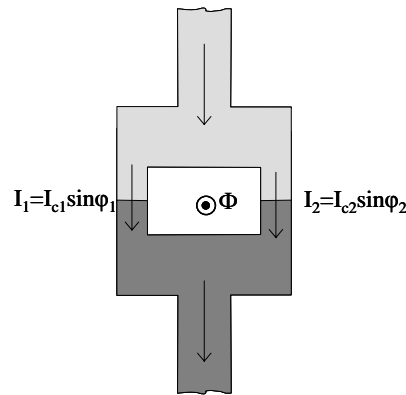
Figure 2.17:   dc-SQUID

If two junctions are incorporated in parallel in a superconducting loop the resulting device is called a d.c. Superconducting QUantum Interference Device (SQUID). The total current through the SQUID is given by adding the currents flowing through each junction: $I_s = I_1 + I_2$ where $I_1 = I_{c1}\sin\varphi_1$ and $I_2 = I_{c2}\sin\varphi_2$ according to the first

Josephson equation (see figure 2.17). In a magnetic field φ_1 and φ_2 are related to each other by the flux through the loop area according to:

$$\varphi_1 - \varphi_2 = 2\pi \frac{\Phi}{\Phi_0} \qquad 2.21$$

where Φ is the total flux through the loop [16].

Substituting 2.21 into the expression for the total current and rearranging it using simple algebraic relation an expression for the current as a function of the flux is obtained:

$$I_s = 2I_c \cos\frac{\pi\Phi}{\Phi_0} \sin\left(\varphi_2 + \frac{\pi\Phi_0}{\Phi}\right) \qquad 2.22$$

Here we have neglected the inductance of the loop and assumed that $I_{c1} = I_{c2} = I_c$ The phase φ_2 will change according to the bias current and hence the maximum super current that can be sent through the SQUID will modulate as a function of the magnetic flux through the loop according to:

$$I_s = 2I_c \left|\cos\left(\frac{\pi\Phi}{\Phi_0}\right)\right| \qquad 2.23$$
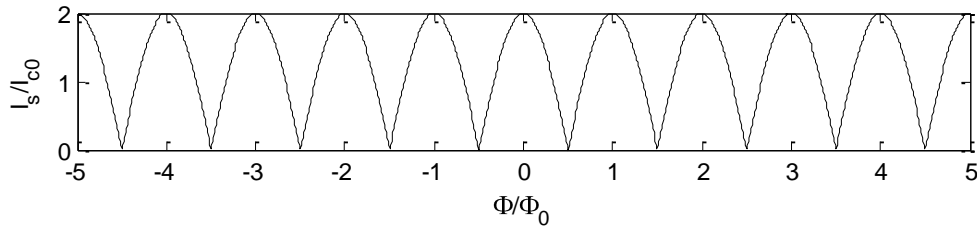
Figure 2.18:   Modulation of the critical current as a function of the applied flux for a conventional dc-SQUID.

In general the self inductance of a SQUID cannot be neglected and Φ will represent the total flux through the loop given by the external field plus the flux induced by the inductance of the SQUID. In an external field screening currents, I_{sc}, are circulating in the SQUID loop and if the inductance is large they will generate a magnetic flux opposite to the externally applied one. The total flux is then given by:

$$\Phi = \Phi_e - LI_{sc} \qquad 2.24$$

A measure of the self inductance of the loop is given by the parameter $\beta_L = 2LI_c/\Phi_0$. For a negligible self inductance the magnetic pattern is always symmetric, but an

asymmetry of the critical currents of the two junctions can reduce the modulation depth of the magnetic pattern. In a SQUID with self inductance the modulation depth is reduced if β_L is increased. For a SQUID with self inductance plus an asymmetry in the junctions the situation becomes more complex and one cannot get an analytical expression of $I_c(B)$. The symmetry around zero field is generally lost in a similar way to the situation of a long junction with a non uniform current density. Typically the pattern becomes slanted as seen in the $I_c(B)$ pattern in figure 2.19.
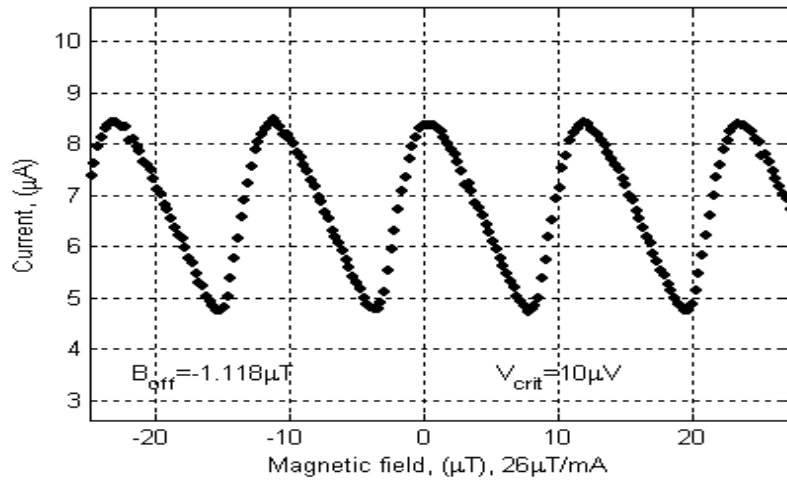
Figure 2.19:   Modulations of the critical current as a function of external magnetic field. Here the slanted behavior typical for SQUIDs with non-negligible inductance is seen. For HTS junctions there is quite often a non-uniformity in the current density.

The total inductance has both a geometrical and a kinetic component according to:

$$L_{tot} = L_{geo} + L_{kin} \qquad\qquad 2.25$$

The geometric inductance, L_{geo}, is defined by the energy of the magnetic filed that is generated by the current flowing through the circuit. The kinetic term, L_{kin}, is associated with the part of the energy that is converted into kinetic energy of the current carriers. It depends both on the geometry and the London penetration depth of the electrodes.

2.4.2 π-SQUIDs

Following the same line of argumentation as before, just including the extra phase shift in the expression for one of the junctions one gets: $I_1 = I_{c1} \sin \varphi_1$ and $I_2 = I_{c2} \sin(\varphi_2 + \pi)$, the maximum supercurrent will depend on the magnetic field as follows:

$$I_s = 2I_c \left| \sin\left(\frac{\pi \Phi}{\Phi_0} \right) \right| \qquad\qquad 2.26$$

here $I_{c1} = I_{c2} = I_c$
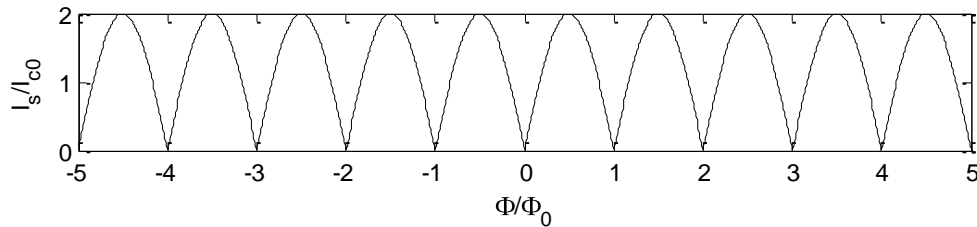
Figure 2.20:   Modulation of the critical current as a function of the applied flux for an ideal dc-SQUID where one junction is a conventional 0-junction and the other junction a π-junction. Note the zero value of the critical current at zero external field.

Squids with one 0-junction and one π-junction can in an all HTS technology be fabricated in the same way as the corner 0-π-junctions as seen in the illustration in fig 2.21.
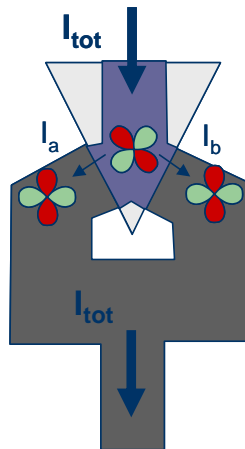
Figure 2.21:   HTS π-SQUID. One junction is a conventional 0-junction and the other a π-junction.

28

2.5 SQUIDs with distributed junction

For the SQUIDs discussed so far the junctions have been considered to be point contacts without any spatial distribution. If we also consider the interference pattern in the junctions themselves, the Fraunhofer pattern and the SQUID modulations are superimposed. The number of SQUID modulations per junction modulation is given by the ratio of the flux through the junction area and the flux through the loop area Φ_{junc}/Φ_{loop}. The larger this ratio is the larger number of SQUID modulations are found inside each Fraunhofer lobe. In figure 2.22 the resulting Ic(B) pattern is shown for a conventional 0-SQUID with distributed junctions and a π-SQUID with distributed junctions. The ratio Φ_{junc}/Φ_{loop} is 0.2. If the flux through the junction area is decreased, for example by shortening the junctions to half the width, so the ratio becomes $\Phi_{junc}/\Phi_{loop} = 0.1$ the modulation pattern changes as seen in figure 2.23. The junction modulations are seen on a much larger scale for the magnetic field and each Fraunhofer lobe contains a larger number of SQUID modulations. This is important to consider when making 0-π-SQUIDs. It can be difficult to distinguish between a 0-SQUID and a 0-π-SQUID if there are too many modulations inside the main Fraunhofer lobe. In real junctions there is also a non-negligible inductance that modifies the modulation pattern and together with a non-uniform current density it can shift the maxima and minima of the pattern.
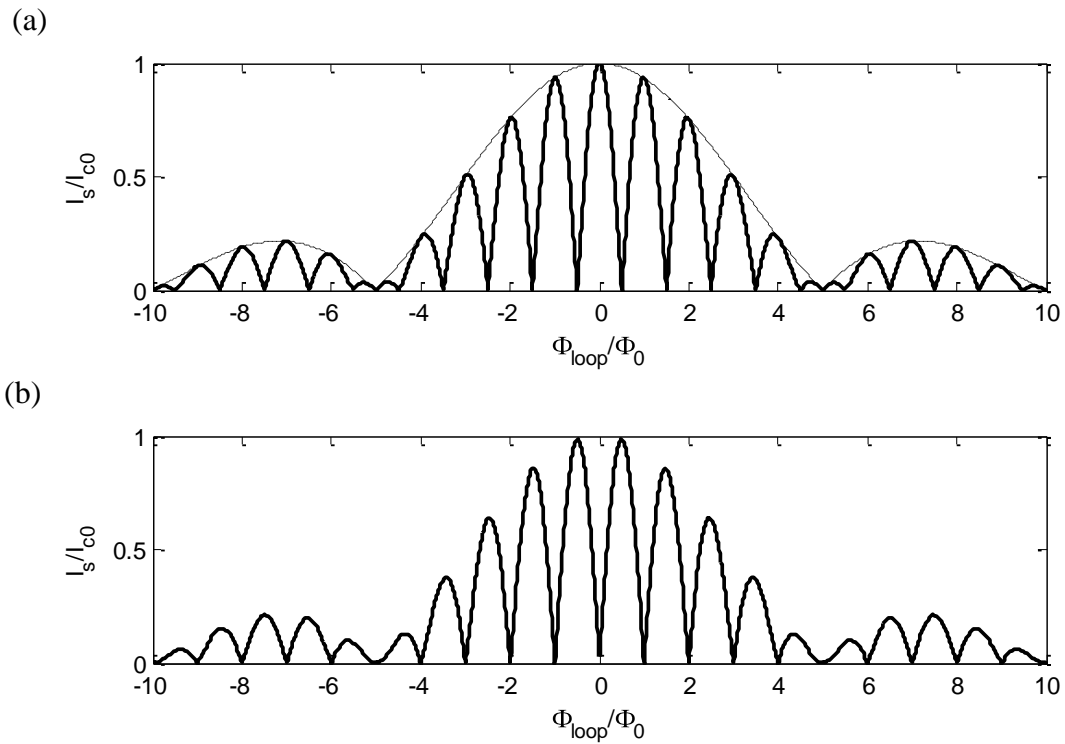
Figure 2.22:   Ic(B) pattern for a 0-SQUID (a) and a π-SQUID (b) in terms of flux
through the loop for SQUIDs with distributed junctions. Here
$\Phi_{junc}/\Phi_{loop} = 0.2$. The dashed line in (a) shows the envelope of the
Fraunhofer pattern.

(a)
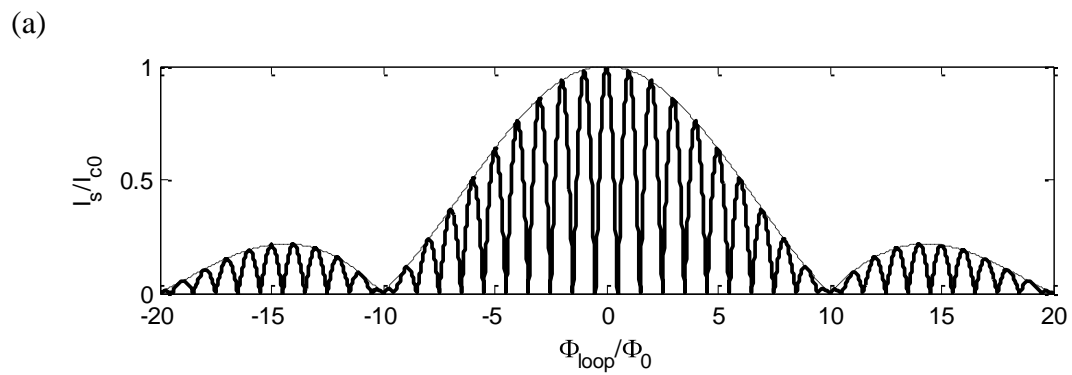
(b)
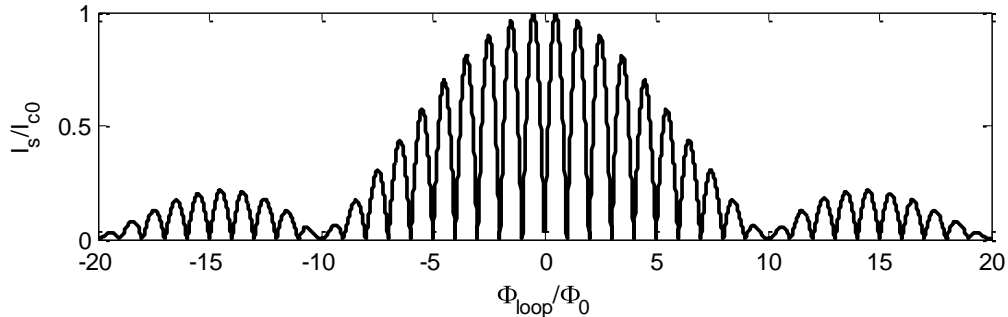
Figure 2.23:   Ic(B) pattern for a 0-SQUID (a) and a 0-π-SQUID (b) with distributed
junctions. $\Phi_{junc}/\Phi_{loop} = 0.1$.

The self inductance in a non-uniform SQUID can shift the maxima and minima of the
modulations. This fact makes it very hard to distinguish between a conventional "0"
squid and a "π" SQUID. A way to increase the credibility of the experiments is to fix the
ratio Φ_{junc}/Φ_{loop} to a value that gives a moderate number of SQUID modulations inside
the Fraunhofer envelop. It was seen in figure 2.22 and 2.23 that it increases the possibility
to distinguish between a maximum and a minimum since the amplitude of the SQUID
modulations is modulated by the Fraunhofer envelope.

When designing a HTS SQUID it is difficult to foresee the exact ratio of the flux between
the junction area and the loop area of the SQUID due to flux focusing effects [23-26] and
faceting at the interface. Figure 2.24 shows a magnetic pattern of two of our SQUIDs,
one 0-SQUID and one 0-π-SQUID, both made with HTS electrodes (YBCO). The
SQUIDs are symmetric with a geometric loop area of 10µm^2 and a junction width of
5µm. Note that the 0-SQUID in (a) shows an almost ideal pattern where the Fraunhofer
envelope can be seen superimposed on the SQUID modulations. The π-SQUID doesn't
show similar ideal behavior. However, the complementary behavior to the 0-SQUID,
with a minimum in critical current at zero magnetic field is clearly visible. Figure 2.25
show an Atomic Force Microscope[1] (AFM) image of a 0-SQUID from the same sample.

---

[1] See chapter 4

(a)
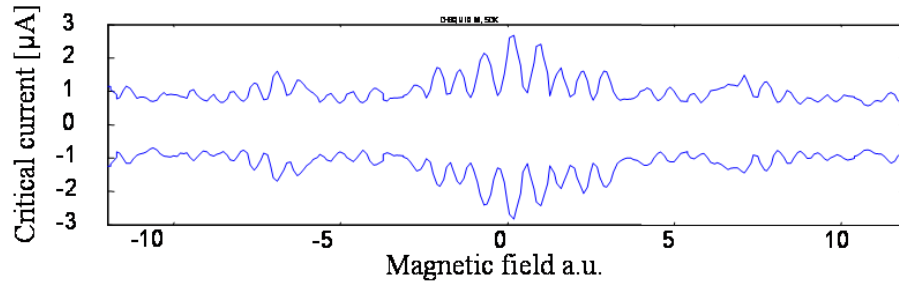
(b)
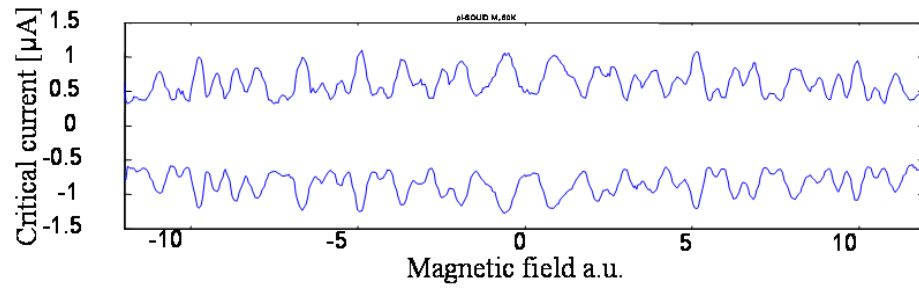
Figure 2.24: $I_c(B)$ pattern for a 0-SQUID (a) and a π-SQUID (b) fabricated with the biepitaxial technology. In both devices the loop area is 10 μm^2 and the junction width 5 μm for each junction.
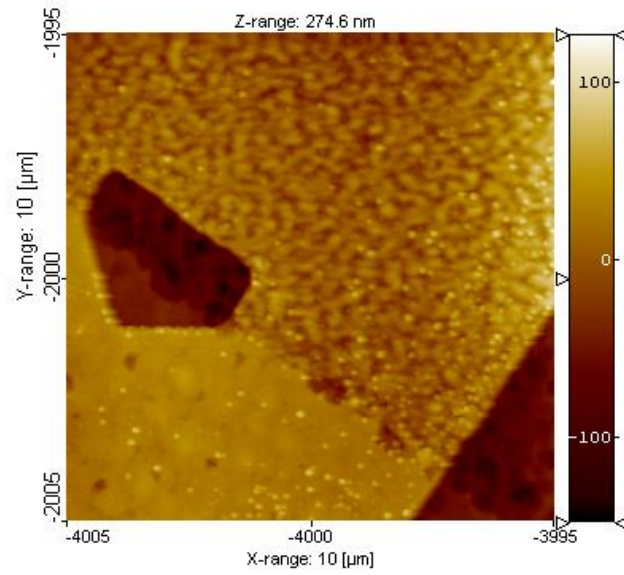
Figure 2.25:   AFM image of part of a 0-SQUID fabricated in YBCO. The different structure of the two electrodes is a result of different crystal orientations.

Realization of Josephson Junctions

3.1 LTS/HTS multilayer Josephson Junctions

Josephson junctions in LTS materials have been fabricated since the discovery of the Josephson effect in the sixties. In LTS there is no directionality of the OP that has to be considered when designing Josephson junctions like in the case of the HTS. Moreover the long coherence length makes small defects and interfaces between domains less important. The properties of LTS Josephson junctions can be tuned with a high accuracy by the fabrication procedure and the reproducibility is high.

One common way of making LTS Josephson junctions is to use double angle evaporation to deposit the electrodes and oxidation of the material to create the barrier. Niobium and Aluminum are the most used materials and they are both processed in similar ways. The method is as follows:

- A bridge like structure is created with photoresist on the substrate (commonly the substrate is silicon or silicon with a top layer of silicon oxide if an isolating substrate is required).

- The Aluminum is evaporated onto the sample with an incident angle as seen in figure 3.1.

- The electrode is oxidized in situ by filling the chamber with oxygen of a certain pressure during a certain time. The thickness of the oxide layer can be controlled very precisely in this way.

- The second electrode is evaporated with an angle from the opposite side.

The result is an Al/AlO$_{3-\delta}$/Al junction with a very well defined barrier thickness. The method is popular because of its simplicity. Only thermal evaporation in needed for the deposition of the electrodes and the oxidizing is made in situ. Niobium can be used the same way, but since it hardly oxidize in a uniform way a thin layer of Aluminum is evaporated on top of the first electrode and is oxidized forming an Nb/Al/AlO$_{3-\delta}$/Al junction.
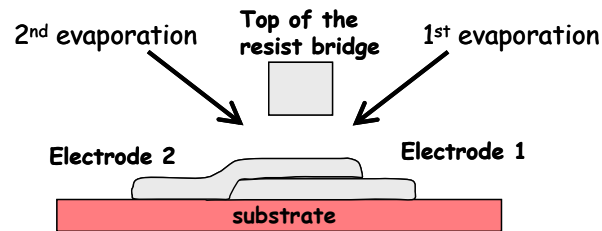
Figure 3.1:   General idea of the double angle evaporation technique for LTS JJ. The first electrode is evaporated onto the substrate and after oxidation the second electrode is evaporated in situ.

Another widely used technique for Nb and Al is the trilayer technique where the insulating barrier, usually an oxide like for the previous method, is sandwiched between two electrodes deposited by sputtering (see figure 3.2). The devices are patterned after the deposition of the films. A somewhat similar structure to the two mentioned above is the ramp-edge structure depictured in figure 3.3 It has been used also for junctions between high and low temperature superconductors and for all high Tc-superconductors [27]. After deposition of the bottom electrode it is patterned by lithography and Ar ion etching. The etched surface can be reconstructed by depositing new layer of the superconductor followed by the barrier and the second electrode.
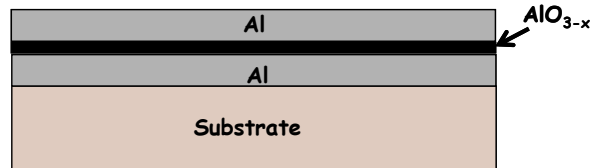
Figure 3.2:   Trilayer structure with two aluminum electrodes and aluminum oxide barrier.
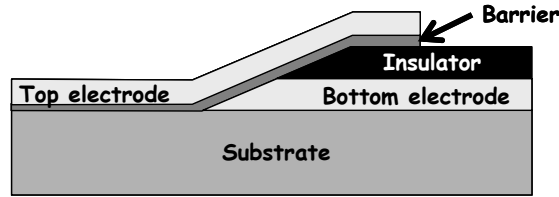
Figure 3.3:   Ramp edge junction.

3.2 Grain boundary Josephson junctions

Due to the short coherence length (both in *ab*-plane and in c-axis direction) grain boundaries (GB) between otherwise crystalline YBCO will present a weakened superconductivity. Depending on the orientation of the two grains the grain boundary interface may show Josephson effect [28,29]. There are a number of different ways to produce grain boundaries. They all require a controlled growth of the superconductor which is provided by epitaxial growth of the film onto a substrate with matching lattice parameters. The most common ways to reproducibly obtain GB JJ are the bicrystal, biepitaxial and step edge technique.

3.2.1 Bicrystal samples

The simplest way to create a GB junction is the bicrystal method where two substrates of different crystallographic orientation are glued together. An artificial GB is created between the superconducting domains grown on top of this structure. The GB is generally characterized by a region of disorder and is usually suffering from oxygen loss, strong enough to make it act as a weak link. The bicrystal samples can be characterized by defining the mis-orientation angle between the two films. The mis-orientation of the second film with respect to the first can be defined by the axis where the rotation happens and by the angle. We have tilt grain boundaries if the rotation happens outside the gain boundary plane, twist if the rotation is in the grain boundary plane. In figure 3.4 two bicrystal samples are shown. One characterized by a [001]-45° tilt of the YBCO and the other characterized by a [100]-45° tilt. Figure 3.5 it is shown a transmission electron microscope image of the GB area for a bicrystal junction of the type presented in figure 3.4b.

(a)
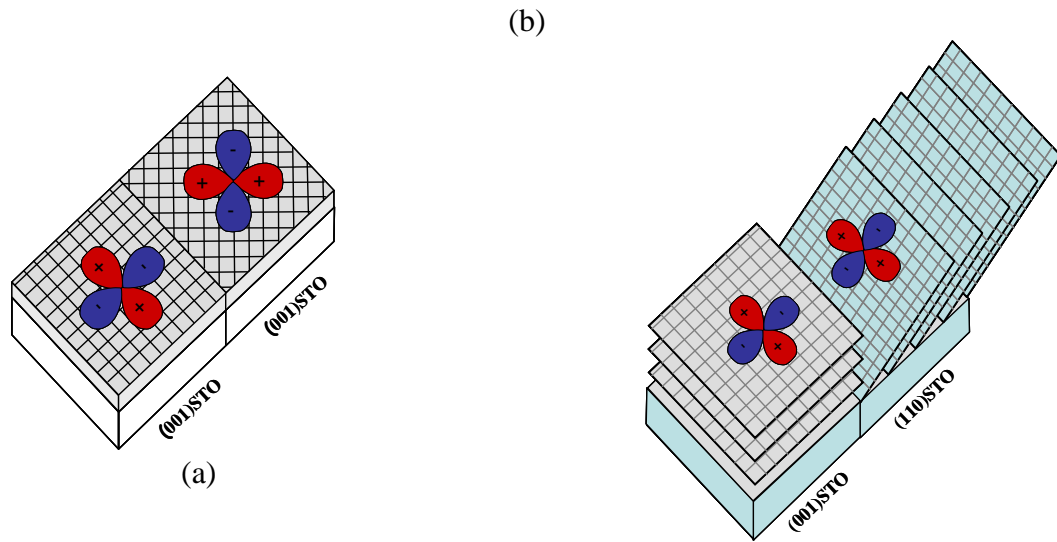
Figure 3.4:   (a) [001]-45º tilt bicrystal sample and (b) [100]-45º tilt bicrystal sample.
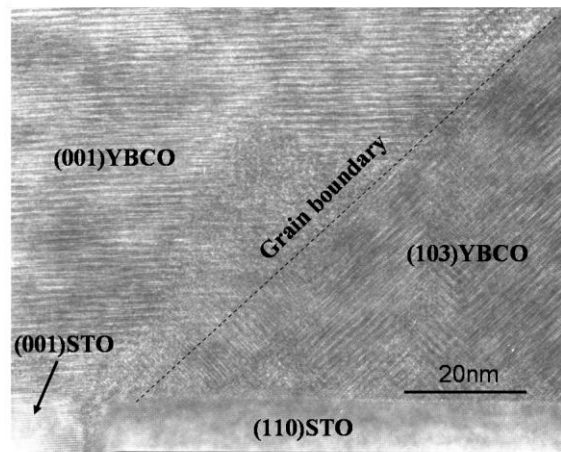
Figure 3.5:   Transmission Electron Microscope image of a cross section of a bicrystal junction. The two different crystal orientations of the YBCO on top of the bicrystal substrate are clearly visible. The interface between the two YBCO orientations, the grain boundary, is marked with the dashed line.

A big disadvantage of the bicrystal method is the limitations in the design of complex circuits. The junctions have to be placed along the GB line and that does not leave much flexibility to design more complicated structures. For the fabrication of corner junctions three or four substrates glued together are required. Such devices have been fabricated successfully [30,31] but only one device per tri/tetra crystal can be obtained.

37

3.2.2 Step edge junctions

Step-edge junctions [32,33] are fabricated by etching a step with a certain angle into the substrate. By choosing the right type of substrate film nucleating on the step can grow with another orientation compared to the film nucleation on the horizontal surfaces as seen in figure 3.6.
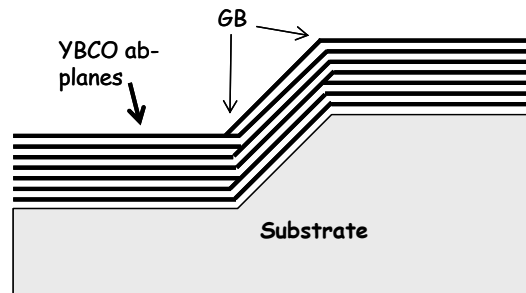
Figure 3.6:   Schematic illustration of a step-edge junction.

3.2.3. Biepitaxial junctions

The biepitaxial technique is conceptually very similar to the bicrystal technique but provides for a considerably larger flexibility in circuit design. Instead of gluing two substrates together a *seedlayer* is deposited onto the substrate. After the deposition it is patterned and removed from parts of the substrate. When the superconducting film is deposited on top it grows with one crystal orientation on the seedlayer and another orientation on the bare substrate. The difference is that with the biepitaxial technique the artificial GB can be formed anywhere on the sample. It is easily understood that for fabrication of 0-π-junction, in the form of corner junctions, this is a huge advantage. Moreover GBs with different structural and transport properties can be fabricated on the same chip. There are several drawbacks though. A step between the surface of the substrate and the surface of the seedlayer is unavoidable which makes the growth mechanisms much more complicated and the GBs less reproducible. In addition, the seedlayer makes the fabrication procedure a multilayer process which is more complicated, especially since the seedlayer has to be patterned by a method requiring many different steps (see chapter 4) before the superconductor can be grown on top. In figure 3.7 a schematic picture of a biepitaxial sample is shown. Here (110) STO is used as substrate and (110) CeO2 as seedlayer providing for (103) YBCO orientation on the bare substrate and (001) YBCO orientation on the seedlayer. Note how different GBs can be obtained by varying the orientation of the seedlayer edge with respect to one of the in plane directions of the substrate.
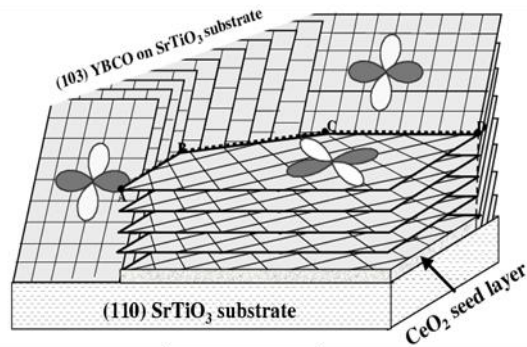
Figure 3.7: STO/CeO$_2$/YBCO biepitaxial sample. By patterning the seedlayer in an appropriate way Josephson junctions can be created anywhere on the chip. The orientation of the seedlayer edge with respect to one of the in plane directions of the substrate effect the properties of the GB. The two limiting orientations are characterized by a [100]-45° tilt + [001]-45° tilt (defined in this thesis as 0° GB angle) and a [100]-45° twist + [001]-45° tilt (defined as 90° GB angle).

Chapter **4**

Fabrication and analysis techniques of biepitaxial GB Josephson Junctions and measurements of the devices

This chapter is intended to give an overview of the fabrication procedure and analysis techniques used to characterize the junctions. In the previous chapter it was mentioned that the thin films LTS junctions usually are made by thermal evaporation of the material onto the substrate. Simple thermal evaporation is not sufficient for complex materials like oxides consisting of more than one kind of atoms since it is an equilibrium process and different atoms will have different evaporation rates and the result will be a non-stoichiometric film. Instead a non-equilibrium process like pulsed laser deposition (PLD) or sputter deposition have to be used. Both methods have its advantages and drawbacks. The samples in this thesis have mainly been fabricated by PLD, but the reason for that is merely the availability of this technique in our laboratory.

Even though the general idea for the sample fabrication is quite simple (the device is built layer by layer from bottom and up) it includes a large number of steps. When the seedlayer has been deposited it has to be removed from part of the substrate. This is done by Ar-ion etching. The parts that should not be removed have to be covered by a mask which in our case is done either by spinning photoresist directly on the sample and expose with UV-light or by depositing carbon and then pattern it by spinning e-beam resist on top and using e-beam lithography. The latter procedure is much more complicated. The advantage to use a very hard mask (carbon) is that it is only slightly effected by the etching procedure which allows sharper edges of the etched structure. E-beam lithography has also a far better resolution and for sub-micron devices it is the best option.

4.1 Fabrication - overview

The steps involved in the fabrication are reviewed below in order to give an overview of the fabrication method.

1. A thin (110) CeO_2 film around 10 nm is deposited by PLD onto a (110) STO substrate

2. 500Å of amorphous carbon is deposited on top of the sample by thermal evaporation

3. A lift-off layer, consisting of a polymer that is easily dissolved in acetone, is spun and baked on top of the carbon. It allows us to obtain the required "undercut" profile. A thicker layer of e-beam resist is then spun on the lift-off layer.

4. E-beam is used to expose the sample according to the desired pattern.

5. Development in a mixture of isopropanol and water removes the parts of the resist that has been exposed to the e-beam together with the lift-off layer under it.

6. O_2-plasma ashing removes lose traces of residual resist that might not have been gone during the developing.

7. Cr-deposition by thermal evaporation

8. Lift off in hot acetone. The chromium on top of the bilayer is removed.

9. Ashing by O_2-plasma removes the residual carbon that isn't protected by the Cr.

    Now the mask is in place and the sample is ready for etching of the unprotected CeO_2.

10. Ar-ion etching (the Cr on top of the carbon mask is removed during the etching and part of the carbon is etched away)

11. The remaining carbon mask is removed by O_2-plasma ashing.

12. The YBCO film is grown by PLD

13. A gold film is deposited by thermal evaporation

14. A thin layer of photoresist is spun and baked on top of the sample.

15. UV-exposure of the photoresist to define the gold pads configuration.

16. Development of the photoresist in MF319 developer solution..

17. Ar-ion etching

18. Removal of the resist in hot acetone

19. Gold evaporation 500Å as a protective layer (or, some gold is allowed to remain in the etching process)

20. Carbon evaporation

21. Step 3-9 are repeated to create a carbon mask for patterning of the YBCO

22. Ar-ion etching of the YBCO

23. O2-plasma ashing to remove the carbon mask

24. Additional Ar-etching to remove the gold layer on top of the YBCO electrodes.

11)

(110)CeO₂

(110)STO

12)

(110)CeO₂

(110)STO

13)

(110)CeO₂

(110)STO

14)

(110)CeO₂

(110)STO

15) UV

(110)CeO₂

(110)STO

16)

(110)CeO₂

(110)STO

17) Ar-ion etching

(110)CeO₂

(110)STO

(110)CeO₂

(110)STO

18)

(110)CeO₂

(110)STO

19)

(110)CeO₂

(110)STO

20)

(110)CeO₂

(110)STO

21)

(110)CeO₂

(110)STO

22) Ar-ion etching

cr

(110)CeO₂

(110)STO

(110)CeO₂

(110)STO

43
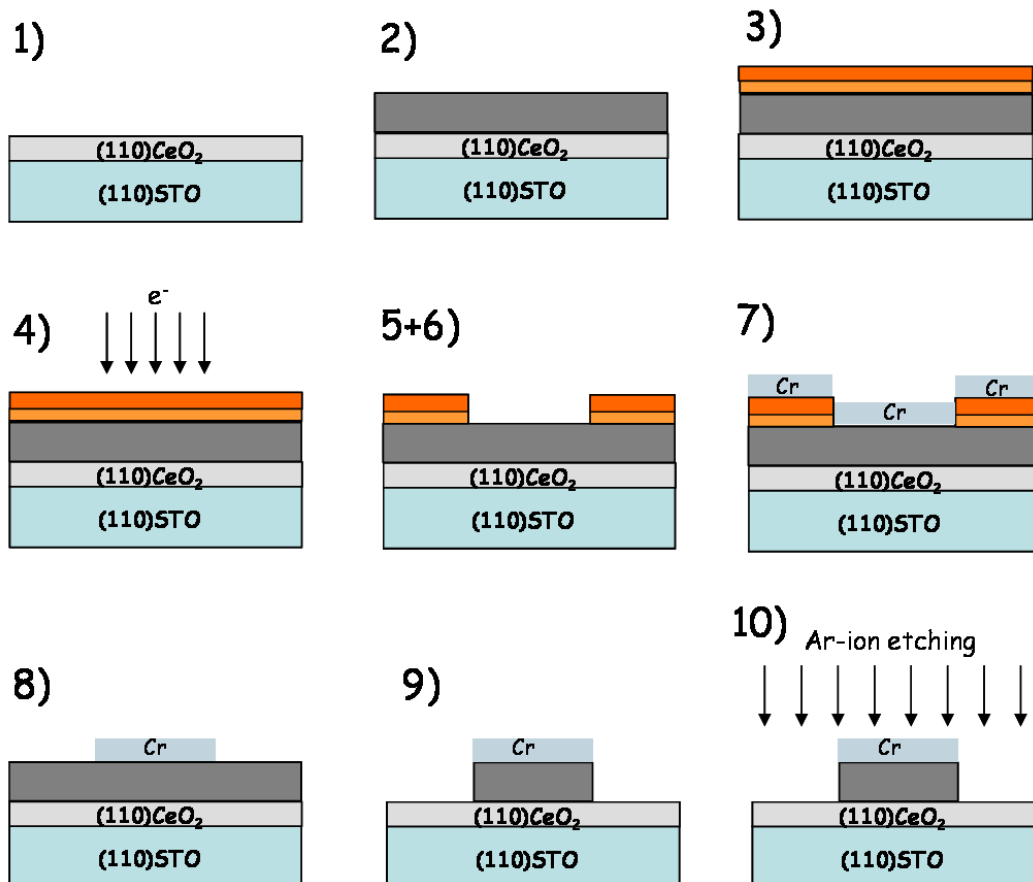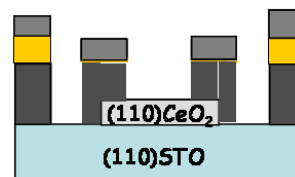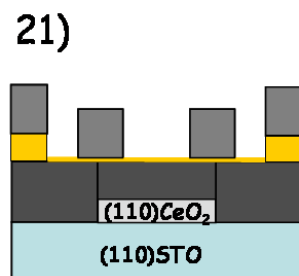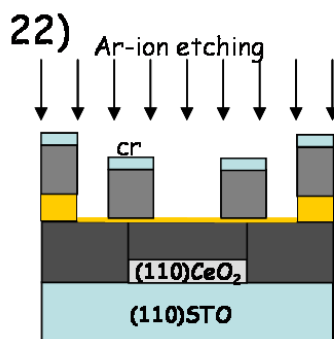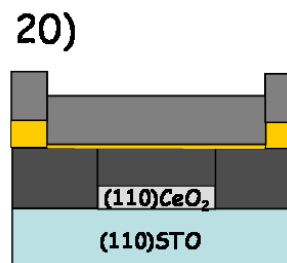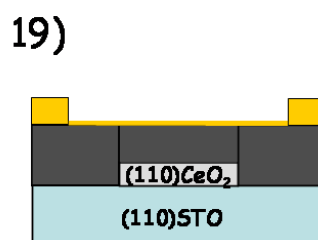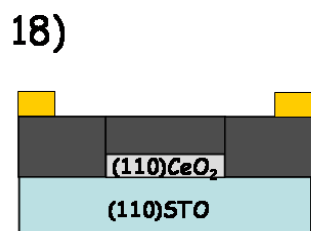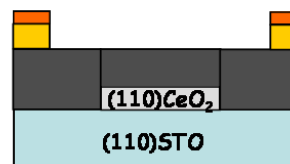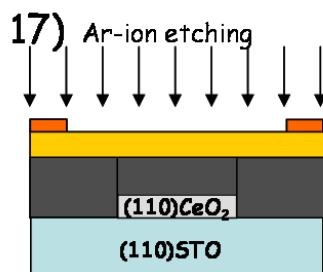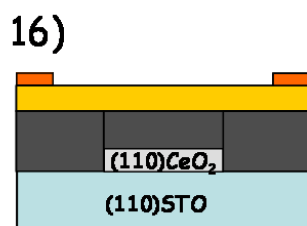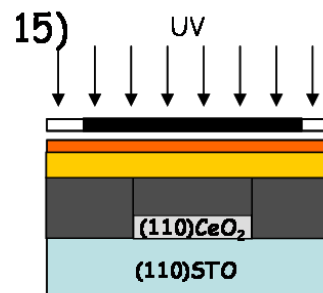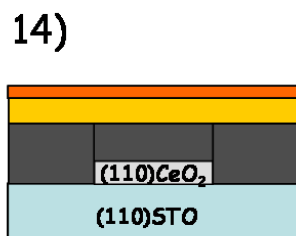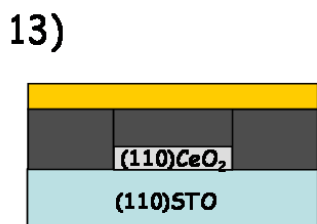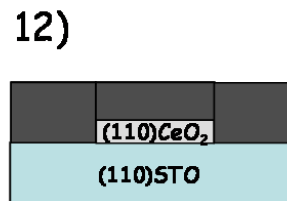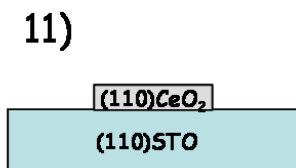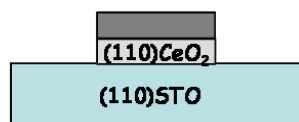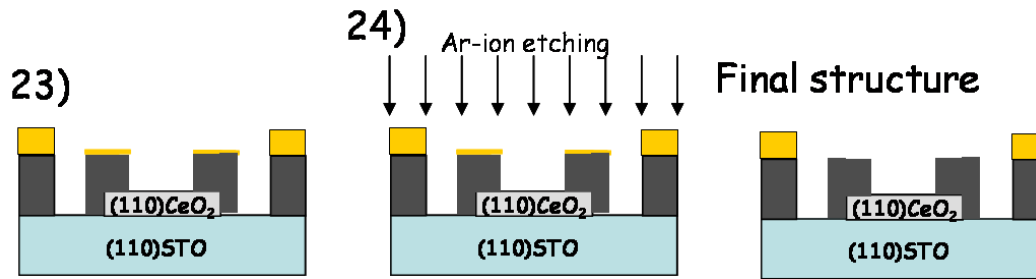
Figure 4.1:   A schematic representation of the steps described in details in paragraph
                4.1.

4.2 Pulsed Laser Deposition

To achieve stoichiometric growth of a complex oxide like YBCO a non equilibrium process has to be used. The Pulsed Laser Deposition technique is a fast and flexible way of growing films and it has become one of the most common methods for thin film deposition. Laser pulses are shot onto a rotating target consisting of a tablet of the material with the right chemical composition. The laser pulses are short, usually around 30ns and are repeated with a rate of 1-10 pulses per second. Each pulse has an energy density of about 2 J/cm^2 and the spot size of the laser beam hitting the target is around 5 mm^2. The energy of the laser pulse is absorbed by the target, but each pulse is too short and high energetic for the energy to be transported into the material by the slow mechanisms of thermal heat transfer. Instead the heating is very local and causes an ejection of material from the surface in the form of a plasma plume. The process is called *laser ablation*. The substrate is glued onto a heater and placed with the surface perpendicular to the plume in a so called *on-axis* geometry. During the deposition the shape of the plume is controlled by the oxygen pressure in the chamber that is typically held between 0.1 to 0.8 mbar by a constant oxygen flow. The disadvantage of the technique is that it is not suitable for large area deposition due to the confined shape of the plasma plume. Typically the substrate has to be < 1cm^2. However, there are PLD systems using a rotating substrate holder that makes it possible to grow films on larger areas.

The ablation process is controlled by the following crucial parameters:

- Energy of the incoming laser beam

- Pressure in the deposition chamber

- Temperature of the substrate

44

- Distance between the target and the substrate (in general fixed for each PLD setup)

- Frequency of the laser pulses

Each of these parameters has to be optimized to achieve high quality films with the correct epitaxy. In general the distance between the target and the substrate is fixed in the deposition setup and not easily changed. Instead the shape and extension of the plume can be tuned by the energy of the laser pulses and the pressure in the chamber. The temperature of the substrate is important and controls the mobility of the atoms on the surface.

In figure 4.2 a schematic picture of the pulsed laser deposition system used in this thesis is shown. The beam enters the chamber via the optics consisting of aperture (not in picture), lens and quarts window. In the particular system used in this thesis an ion gun for Ar and O_2-etching is mounted in the camber. It allows in situ etching of the substrates and films.
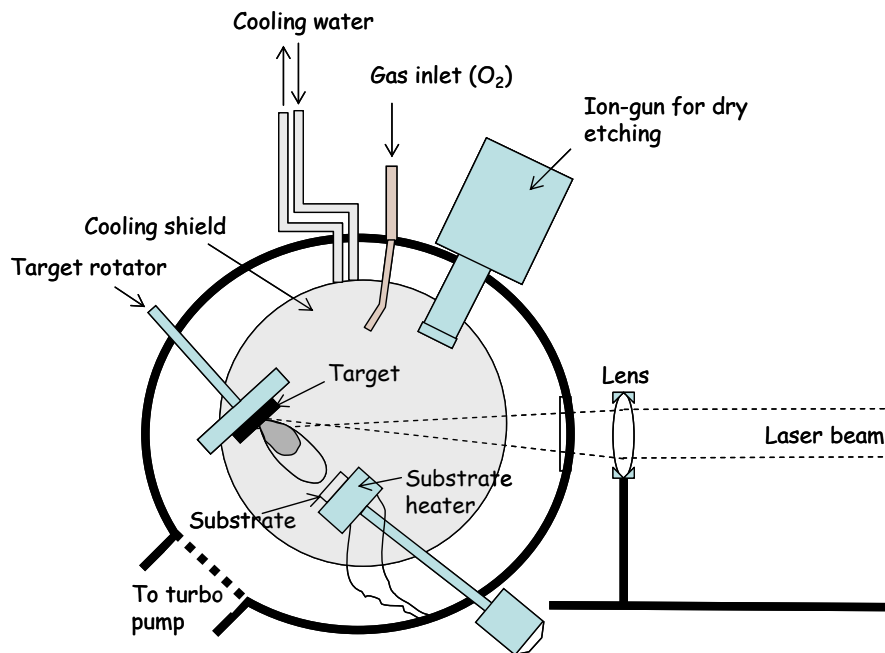
Figure 4.2:   Schematic illustration of the PLD system used in this thesis (known as the "Twin" system). The system is equipped with an ion gun for in situ etching. The heater can be rotated and positioned perpendicular to the ion gun during etching.

4.3 Lithography

The idea of photolithography is to create a protective mask that covers parts of the surface and protects the sample during the Ar-etching of the surrounding parts. A thin film of a UV-sensitive polymer is spun onto the sample and baked on a hotplate to polymerize. The photoresist is exposed to UV-light through a photolithography mask (usually a Cr pattern on a thin glass plate) as seen in figure 4.3. The bondings in the polymer are either weakened (positive resist) or strengthen (negative resist) when exposed to UV-light. In the case of a positive resist, which is the resist used in the fabrication procedure we describe before, the exposed parts can be dissolved in a solvent "the developer", while the non-exposed parts remains unaffected. Once the photoresist-layer is patterned the sample is ready to be etched. After etching the photoresist can be removed by acetone.
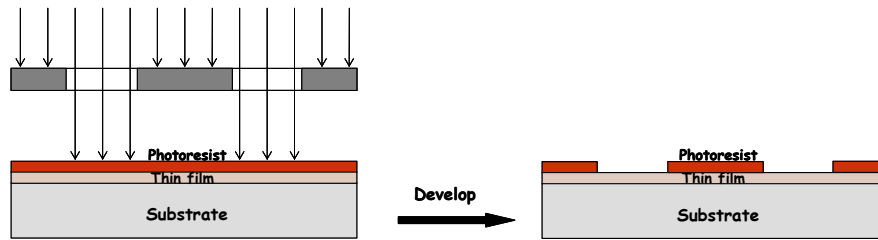
Figure 4.3:   Exposure of photoresist by UV-light through a photolithography mask.

For small features, when a higher resolution is necessary, a similar technique known as electron beam lithography is used. The principles are the same but instead of exposing with photons the exposure is done by electrons.

4.4 Analysis

4.4.1 X-ray diffraction

X-ray diffraction (XRD) can provide structural information of bulk materials and films. A x-ray beam is reflected by the crystal planes in the sample according to Bragg's law:

$$n \cdot \lambda = 2d \sin \theta , \ n = 1,2,3,...$$

where d is the distance between the lattice planes, λ the wavelength of the incoming beam and θ the angle at which reflections can be detected (see figure 4.4) The X-ray

system used in this thesis consists of a X-ray source, primary and secondary optics, and a detector.
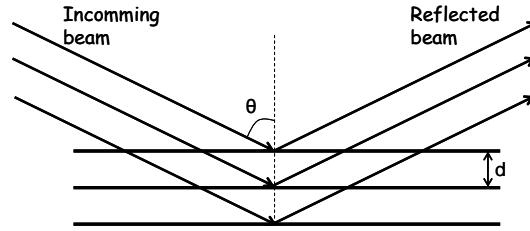
Figure 4.4:   The incoming beam from the X-ray source is reflected against the crystal planes in the sample according to Bragg's law. d is the spacing between the crystal planes in the lattice.

In a θ-2θ (or Bragg-Brentano) scan the angle θ is changed and the reflections detected. The θ-2θ scan gives information about the different crystal orientations in the sample. Depending on the material and it's orientation reflections are given at different θ.

The ω-scan (or rocking curve) provides information about the crystallinity of the film. The detector is kept fixed at a certain angle, but the sample is slightly tilted by changing the angle ω defined in figure 4.5. If a reflection is obtained for a broad range of ω angles it means that the film is polycrystalline and has many domains not completely aligned with each other.
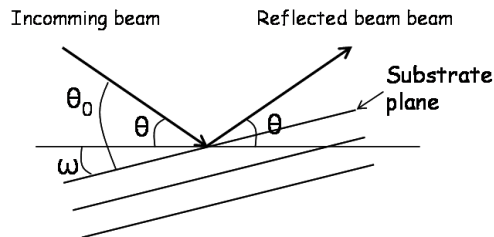
Figure 4.5: ω (or rocking curve) scan.

The phi-scan is used to investigate the in-plane alignment of a film with respect to the in-plane directions of the substrate. The sample and detector is positioned so a certain θ is fixed. The sample is then rotated around it's z-axis (phi-axis) and the reflections are detected.

4.4.2 Atomic Force Microscope
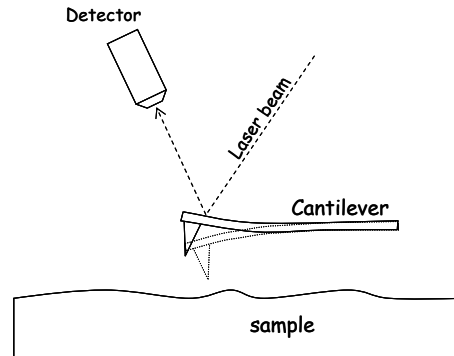
Figure 4.6:   Schematic image of an AFM tip and cantilever in tapping mode. The laser beam focused on the cantilever measures the position and oscillation frequency of the tip.

In an atomic force microscope (AFM) a sharp probe is scanned across the surface. The atomic forces between the tip and sample surface are determined by the sample to tip distance. Close to the sample the repulsive coulomb forces are dominating, while further away from the surface the weak van deer Waal's forces are the dominating ones. In *tapping mode*, which is the one used in this thesis, the tip is oscillating above the surface with a certain frequency and amplitude. In the particular AFM setup used in this thesis the tip is scanned across the surface by a piezoelectric crystal. A laser beam is focused onto the cantilever as seen in figure 4.6 and detects the vertical position of the tip. When the tip is scanned across the surface the vertical position of the tip and the frequency of the oscillations will change according to the surface structure. The position and oscillation frequency of the tip is detected for each spot on the surface and an image of the surface is created. Not only the topology but also chemical composition that changes the forces between surface and tip effects the image. Depending on the data colleted different types of images can be produced. The AFM images in this thesis are height images, showing the topology of the surface.

4.5 Other methods for analysis and characterization

The characterization methods presented here have been employed in cooperation with other research groups.

4.5.1 Scanning Electron Microscope

The scanning electron microscope (SEM) uses an electron beam to scan across the sample. When the beam hits the sample numerous physical processes occur. By detecting the reflected electrons and the secondary electrons (electrons knocked out from the specimen by the incident electron beam) a visual image can be created. The SEM is a fast analysis tool and can provide information about surface topography, chemical composition and crystallography. Unfortunately it cannot be used for the diagnostic of the oxide devices because of the bombardment of electrons that can destroy the tiny structures.

4.5.2 Transmission electron microscopy

Transmission electron microscopy (TEM) is a very advanced imaging technique with atomic resolution. It can provide detailed information about the microstructure of the sample. In our case it has been used primarily to investigate the interfaces of the biepitaxial samples.

A high energy electron beam (the acceleration voltage of the electron gun is usually between 100 to 300 kV) is incident on the sample. The almost parallel beam of electrons are scattered by a crystalline sample according to Bragg's law. After passing through the sample the electron beams are collected by the objective lens and are projected on to a screen (see figure 4.7). The image plane provides an image of the sample with a resolution determined by the objective lens, while the back focal plane simultaneously gives a diffraction pattern of the same area.

To be transparent to electrons the sample has to be very thin, typically less than 100nm. The sample preparation is hence very delicate procedure. To select the interesting area on a sample high precision is important. It might, for example, be a junction of a couple of micrometers that are the interesting part to cut out. The procedure is the following: A protective Pt strip is deposited on the interesting area and after that the sides along the Pt strip are ion milled. A U-shaped cut is mage by the ion milling so the specimen is only attached to the rest of the sample in the short ends. A needle is attached to the specimen before the short sides are finally cut by ion milling and the sample is lifted out. The specimen is welded onto a Cu-grid and then thinned down to electron transparency.
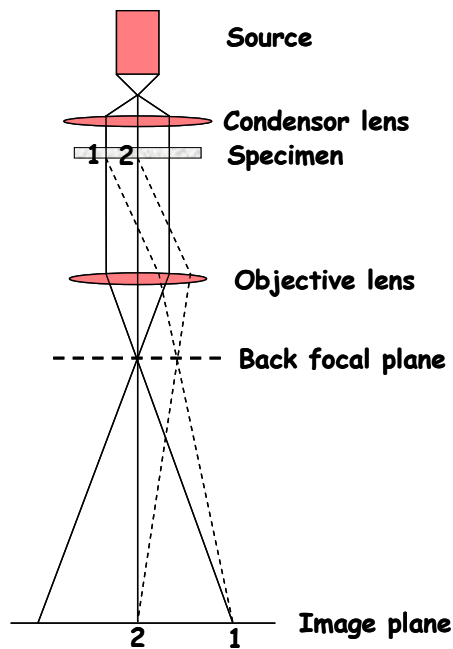
Figure 4.7:   Schematic illustration of a TEM.

4.5.3 Scanning SQUID microscope

A scanning SQUID microscope uses a small SQUID to scan the surface. The SQUID is an extremely sensitive detector of magnetic flux and an image of the magnetic field distribution in the sample is generated. The measurements with SSM have been performed at the University of Twente.

4.6 Measurements

Unless something else is presented, all measurements in this thesis have been performed by current biased four-point measurements. Each device on the chip is connected to gold pads by superconducting electrodes. The sample is glued to a holder and then wedge bonded from the gold pads to the sample holder by thin gold wires. The sample holder is connected to a dip-stick and immersed into liquid helium.

Two types of dip-sticks have been used. A conventional dipstick for measurements at 4.2K and a ^{3}He system for measurements down to 300mK. For the measurements the He-dewar containing the liquid helium can be equipped with both a µ-metal and a

superconducting shield. The measurements are carried out in an electromagnetic interference shielded room.

The measurement setup is the same for both dipsticks used and is presented in the schematic illustration in figure 4.8.
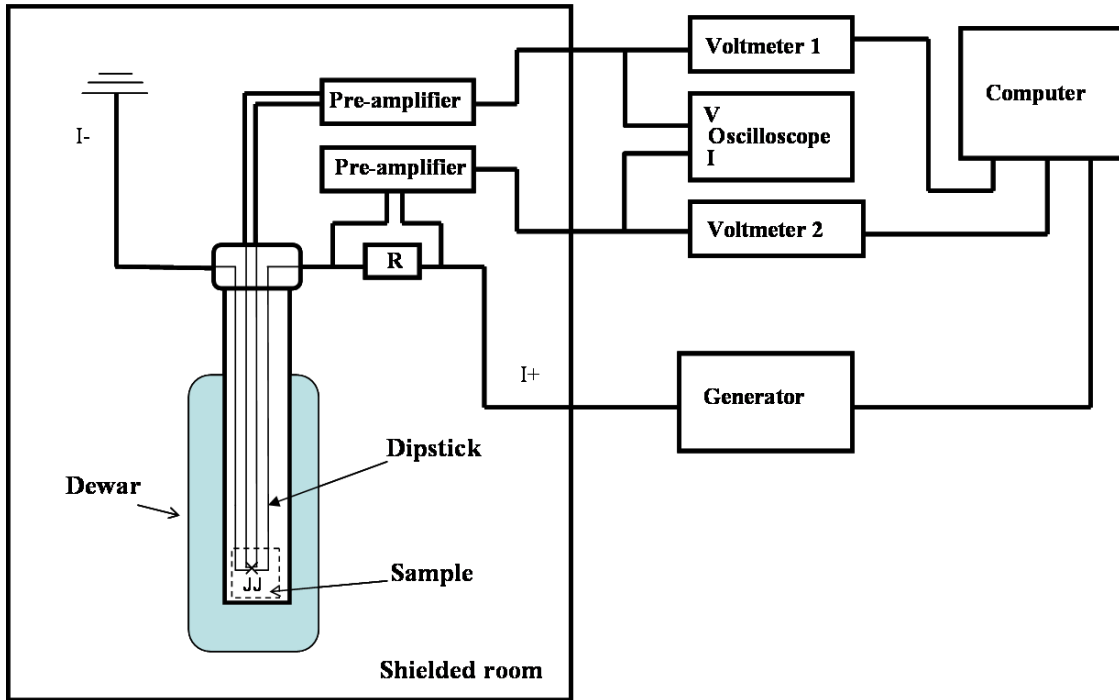
Figure 4.8:   Measurement setup. In this setup the voltage is measured by voltmeter 1 and the current by voltmeter 2.

Biepitaxial STO/CeO2/YBCO structures

The devices presented in this thesis are mainly fabricated by using (110) STO as substrate and CeO$_2$ as seed layer. The reason for using these particular materials is that by choosing the right deposition conditions, the CeO$_2$ film grows (110) oriented on the (110) STO substrate. The YBCO deposited on this bilayer, with the right conditions, will be *c*-axis oriented with the *ab*-planes rotated 45º with respect to the [001] in plane direction of the substrate. The in-plane rotation is crucial for the fabrication of 0-π-junctions, which has been one of the main goals during the work of this thesis. Figure 5.1 presents a schematic illustration of the growth of YBCO on a (110) STO substrate with a patterned (110) CeO$_2$ seed layer. Since YBCO grows (103) on the bare substrate a grain boundary is formed close to the CeO$_2$ step.

(a)

(b)
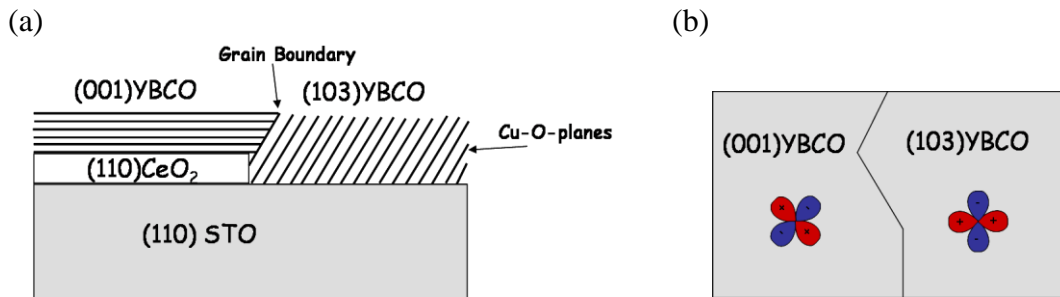
Figure 5.1:   (a) Schematic cross section illustrating the principle of the biepitaxial GB samples. The picture shows the orientation of the Cu-O-planes for the YBCO grown on (110) CeO2 and (110) STO respective. (b) top view of the sample. The (001) YBCO grown on (110) CeO2 have an in-plane rotation of 45° with respect to the [001] direction of the substrate. The top view also shows different orientations of the edge of the CeO2 including the nucleation of structural different GBs compared to that shown in fig 5.1a.

All TEM and SEM images shown in this chapter are from authentic samples fabricated during this thesis with the aim of getting a deeper understanding of the complicated growth mechanisms in this kind of biepitaxial grain boundaries. The imaging has been performed by the group of Microscopy and Microanalysis at Chalmers University of Technology.

During the work of this thesis a lot of effort has been put into achieving the best conditions for the growth of the CeO_2 and YBCO thin films. High quality of the films and grain boundaries are crucial for the fabrication of reliable devices.

The fabrication method was originally invented for thin film samples grown by sputtering [34]. Due to the different nature of the process of sputtering and PLD (used in this thesis) we had to start from the very beginning to study the growth habits of CeO_2 and YBCO that grow on (110) STO substrates.

In this paragraph I will present the epitaxy of CeO_2 on a (110) STO substrate and of YBCO on both the substrate and seedlayer. It is found that more than one orientation for both the seedlayer and the YBCO film is possible. Furthermore I will discuss the details of the growth of the thin films and the parameters that strongest influence which orientation that will be dominating.

5.1 Epitaxy and growth orientation

5.1.1 CeO$_2$ seedlayer on (110) STO substrate

STO is a perovskite with lattice parameter a=3.91Å. The substrates we use are (110) oriented which means that the in plane surface axes are [001] and [1-10]. The (110) STO planes are given by the shaded area in the unit cell in figure 5.2. The substrate can have two different terminations as seen in the figure -- either TiO-plane termination or oxygen-plane termination. CeO_2 can grow (110), (100) or (111) oriented on the (110) STO, but it is only the (110) CeO_2 that introduces the wanted in-plane rotation of YBCO. The lattice

parameters for the different orientations are given in table 5.1 and in figure 5.3 the epitaxy for the different CeO$_2$ orientations on (110) STO are show.
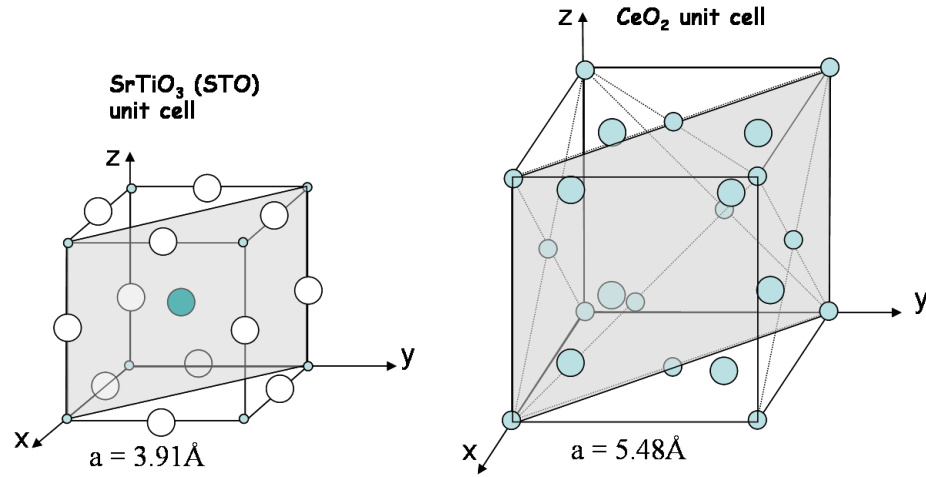
Figure 5.2:   Unit cell for STO and CeO$_2$. The (110) planes are represented by the shaded area.

Orientation	[001] direction, Å	[1-10] direction, Å	[100] direction, Å	[010] direction, Å	[-2 -2 1] direction, Å
(110) STO	3.91	5.54			
(110) CeO$_2$	5.4	7.64			
(001) CeO$_2$			5.4	5.4	
(111) CeO$_2$		7.64			6.62

Table 5.1:   In plane lattice parameters for (110) STO and the possible growth orientations of CeO$_2$.
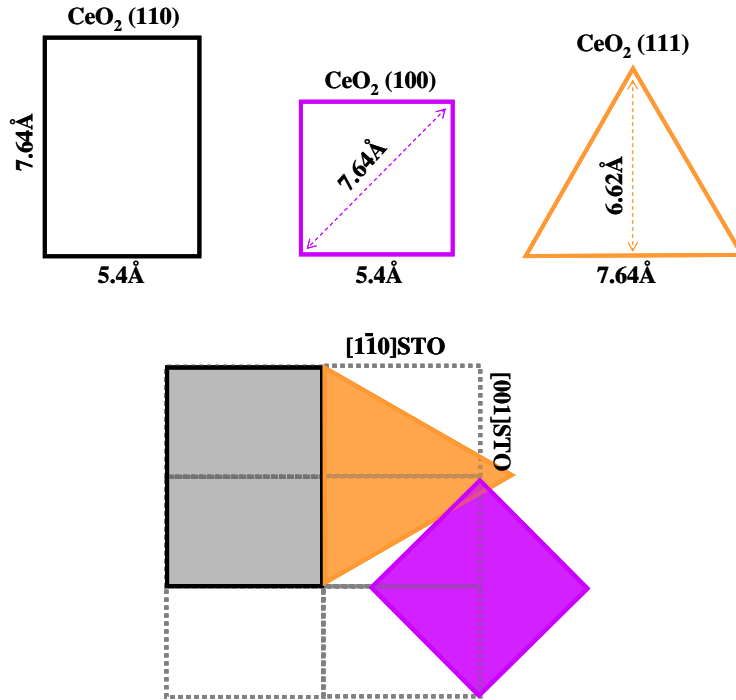
Figure 5.3: The possible growth orientation for CeO$_2$ on (110) STO.

From picture 5.3 it is clear that only (110) CeO$_2$ films have full epitaxy on (110) STO. (100) CeO$_2$ and (111) CeO$_2$ matches the lattice of the substrate only in one crystallographic direction. Consequently (110) CeO$_2$ should be the preferred growth orientation. Unfortunately this is not the case. We have found that the conditions of the surface of the as-delivered substrates play a fundamental role for which orientation that will be favored. CeO$_2$ films grown on substrates that did not undergo a surface treatment always presented a mixture of (111) and (110) CeO$_2$. (111) growth is a low surface energy growth and is favored when impurities or contaminants are present.

5.1.2 YBCO on CeO$_2$ seedlayer

YBCO films grow (001) oriented on all CeO$_2$ orientations presented in previous paragraph. Figure 5.4 shows the possible epitaxial orientations for (001) YBCO on the different CeO$_2$ growths. As seen in the figure only on (110) CeO$_2$ the in plane rotation will take place. However, it is also possible for YBCO to grow non-rotated on (110) CeO$_2$. Both growths result in half epitaxy.

55
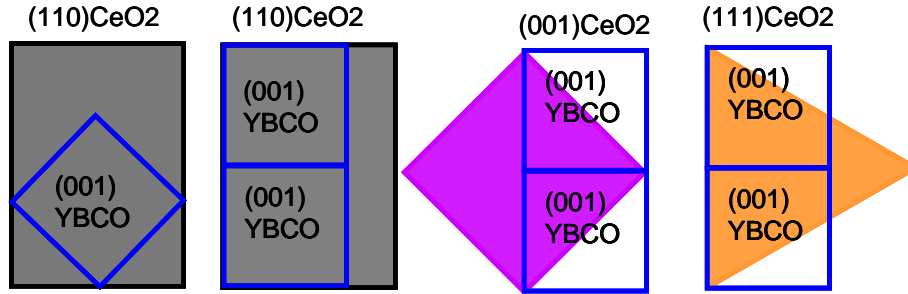
Figure 5.4:   The orientation of YBCO on the three different CeO_2 orientations that can be grown on (110) STO. From the picture it is clear that only (110) CeO_2 can provide the in-plane rotated growth of the (001) YBCO.

5.1.3 YBCO on (110) STO

On (110) STO substrates, (103) oriented YBCO is the preferred growth at high temperatures. On exact substrates a mixture of (103) and (-103) YBCO is possible. The mechanism behind the mixture of the two orientations can be understood by looking at the interface on a microscopic scale. TEM pictures of the (110) STO surface shows that it consists of small microfacets of (100) and (010) orientation as sketched in figure 5.5. On both surfaces YBCO grows *c*-axis oriented with a mismatch of less than 2.5% between the *a*-axis of YBCO and the lattice constant of STO. The YBCO is equally likely to start nucleate on the (100) facets as on the (010) facets so the result will be a growth with a mixed orientation where some grains grow with a 45º tilt of the *ab*-planes in one direction and other grains are tilted in the opposite direction (see figure 5.6) corresponding to (103) or (-103) growths.
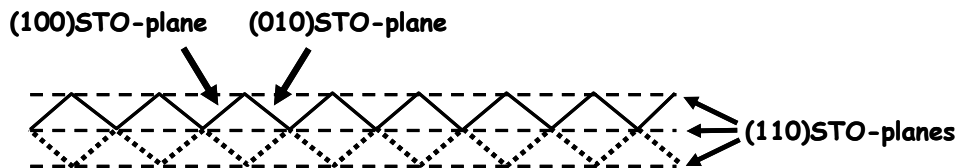
Figure 5.5:   Cross section through the surface of an exact (110) STO substrate. The (110) planes are shown as horizontal dashed lines. The true surface consist of (100) and (010) facets in a zigzag-shaped manner.
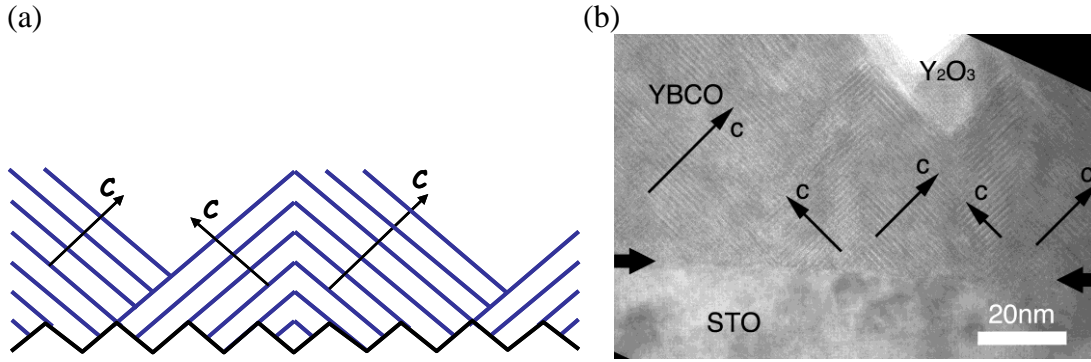
Figure 5.6:   (a) Growth of (103) YBCO on an exact (110) STO substrate. The orientation of the superconducting Cu-O planes is represented by the lines. YBCO grows c-axis oriented on (100) and (010) STO. For an exact (110) STO substrate there is an equal number of (100) and (010) facets resulting in a YBCO film with domains of (-103) and (103) orientation. (b) A TEM image that shows the mixture of the two orientation of the YBCO.

If instead the (110) STO substrate is cut with a vicinal angle of a few degrees along the [1-10] direction the growth will be different (see figure 5.7 and 5.8). The substrate is cut so that the nominal surface is represented by the dashed line in the illustration, with a few degrees angle with respect to the (110) STO planes. The "real" surface will have larger (010) facets than (100) facets and as a result the (103) growth will dominate over the (-103) growth. Close to the interface between the STO and YBCO both orientations can be found but at a certain thickness the favored orientation dominates.
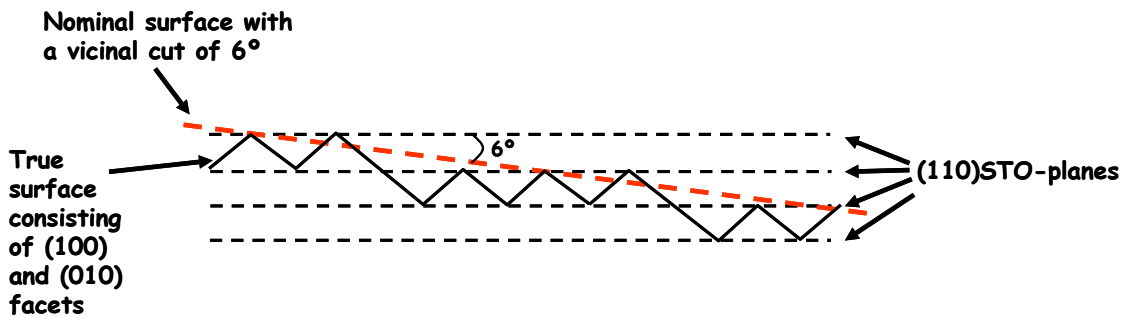
Figure 5.7:   Cross section through the surface of a (110) STO substrate with a 6° vicinal cut towards the [1-10] direction. The "real" surface still consists of (100) and (010) STO facets, but due to the vicinal cut the total area of the (010) facets dominate.
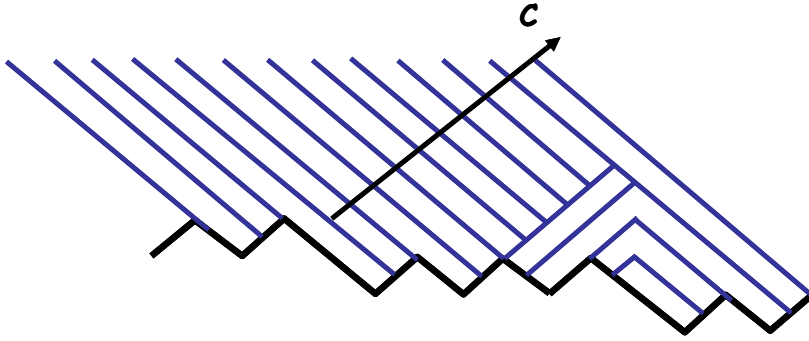
Figure 5.8:   Growth of (103) YBCO on a (110) STO substrate with a vicinal cut of 6º.
As a result of the larger area of (010) facets compared to (100) facets,
which is induced by the vicinal cut, one orientation of the (103) YBCO
growth will dominate.

5.2 Thin film growth

The thin films have been grown by pulsed laser deposition using an excimer laser and a
vacuum chamber with a base pressure of around 7×10^{-7}. The devices are fabricated on 5
$\times$ 5 mm^2 substrates.

5.2.1 Growth of CeO$_2$ films

The CeO$_2$ is deposited at an oxygen pressure of 0.2mbar and a temperature of 790ºC. The
energy of the laser beam measured in the chamber is 102mJ, the spot size is 5.5mm^2 and
we use a frequency of 1Hz for the laser pulses. The right crystal orientation and a smooth
surface are the two important qualities for the CeO$_2$ films. The interface between the
substrate and the CeO$_2$ does not only effect the quality of the CeO$_2$ film itself, but also
the (001) YBCO film grown on top. We have found that CeO$_2$ films grown on as-
delivered substrates, without any further surface treatment than cleaning with solvents,
always present a mixture of (110) and (111) CeO$_2$. This implies a multi-domain YBCO
film growth with a mixture of rotated and non-rotated (001) YBCO. Figure 5.9a shows an
XRD theta-2theta-scan of a CeO$_2$/YBCO bilayer grown on a non treated surface of a
(110) STO substrate. From the diffractogram it is found that the majority of the CeO$_2$ is
(111) oriented. Only a small amount of (110) CeO2 is present in the film. The in plane
orientation of the (001) YBCO film has been investigated by an XRD phi-scan. The
diffractogram from the phi-scan is shown in figure 5.9b and reveals that the growth
indeed is a mixture of rotated and non rotated (001) YBCO.

(a)
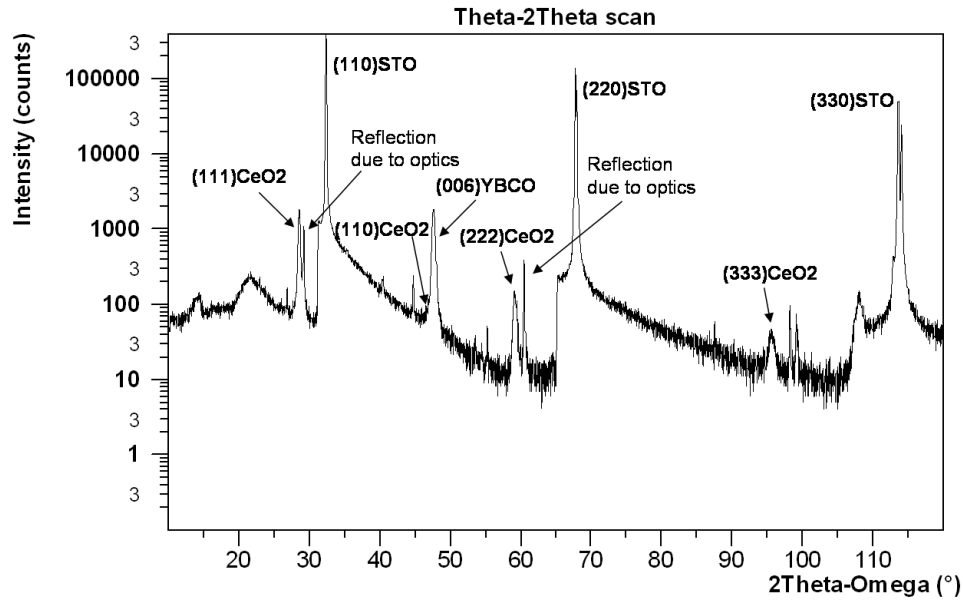
(b)
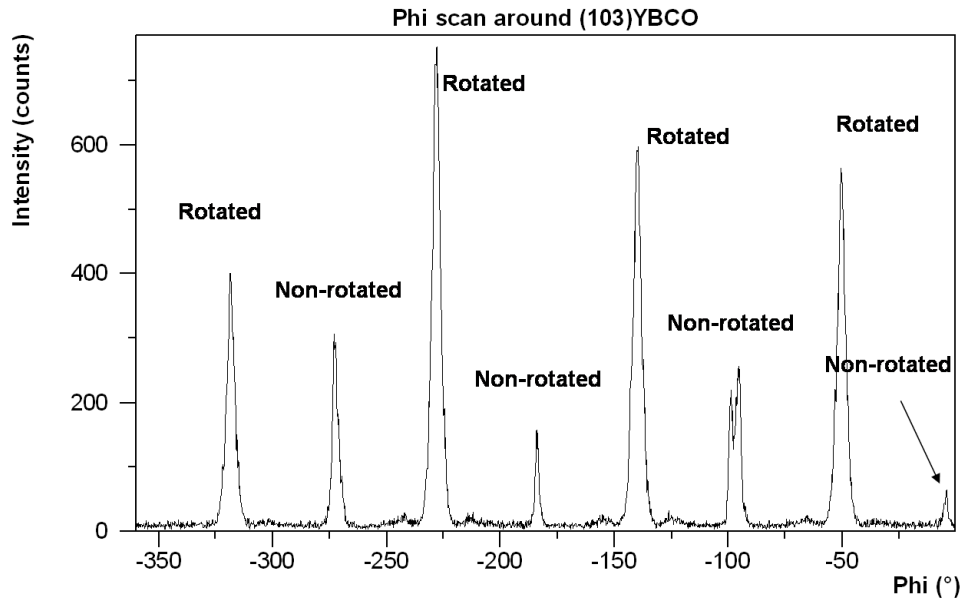
Figure 5.9: (a) Diffractogram for a bilayer CeO2/YBCO film on a non-etched (110) STO substrate. A large amount of (111) CeO2 is present and only a minority of (110) CeO$_2$. (b) A phi-scan for the same sample. Reflections from the {103} planes are obtained and gives information about the in-plane orientation of the (001) YBCO. Here a mixture of rotated and non-rotated (001) YBCO is present.

To enhance the quality of the (110) STO substrate surface we use in situ Ar and O$_2$ ion etching in the deposition chamber before the deposition. The surface becomes amorphous during the etching, which is carried out at 60°C, but recovers its crystalline structure

already at a temperature below 700ºC, well below the deposition temperature of 790ºC. The transition of the surface from amorphous to crystalline has been investigated by Reflection High Energy Electron Diffraction (RHEED). The etching procedure is initiated at V=300V and I=100mA but at the end of the etching sequence both the voltage and current are reduced and only oxygen is used. The procedure was established in order to have a light impact on the surface and to avoid unnecessary surface roughness. Figure 5.10 shows TEM pictures of CeO_2 grown on (110) STO with and without in situ etching. It is clear that the interface is much cleaner and well defined in the etched case.

On etched and re-crystallized surfaces (111) CeO_2 is not present as seen from the XRD data presented in figure 5.11a. Instead the CeO_2 is completely (110) oriented. With a single domain of (110) CeO_2 as seedlayer the (001) YBCO, under the right deposition conditions, grows completely rotated as is shown in the corresponding phi scan in figure 5.11b. In the same graph one can also see reflections for the (110) CeO_2. From the position of the peaks it is found that the CeO_2 is aligned with the in-plane direction of the substrate. Indeed the (103) YBCO and the (200) CeO_2 have close angles. For this reason the phi-scan shows both the in-plane alignment of YBCO and of CeO_2.

(a) **(b)**
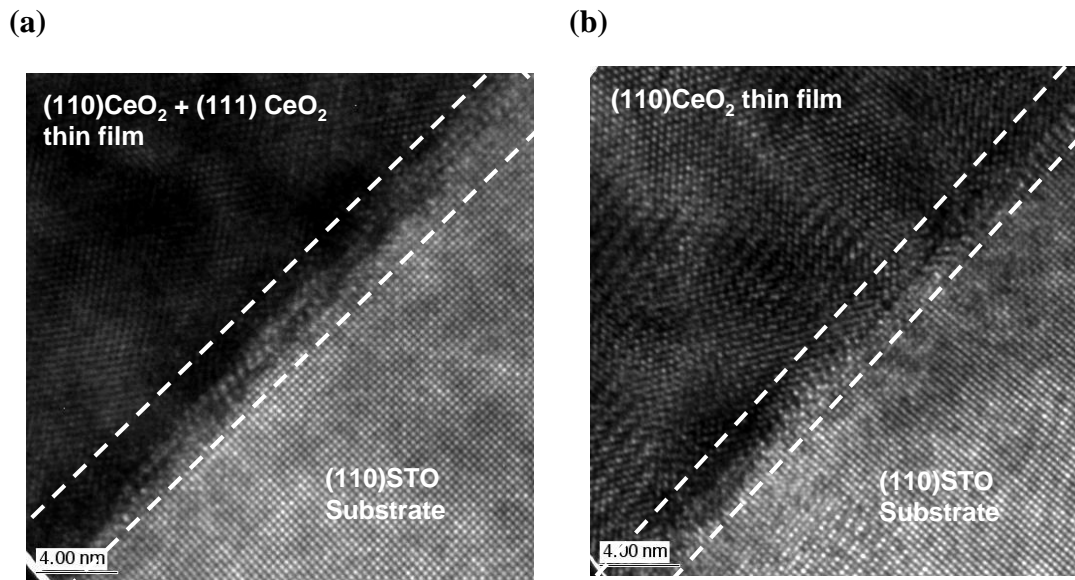
Figure 5.10: Interface between (110) STO substrate and CeO_2 thin film for etched (a) and non-etched (b) surface. The interface between the substrate and seedlayer is found in the area marked by the dashed line in the figure. The etched sample exhibits a much cleaner and more well defined interface, a condition that favors (110) orientation of the CeO_2.
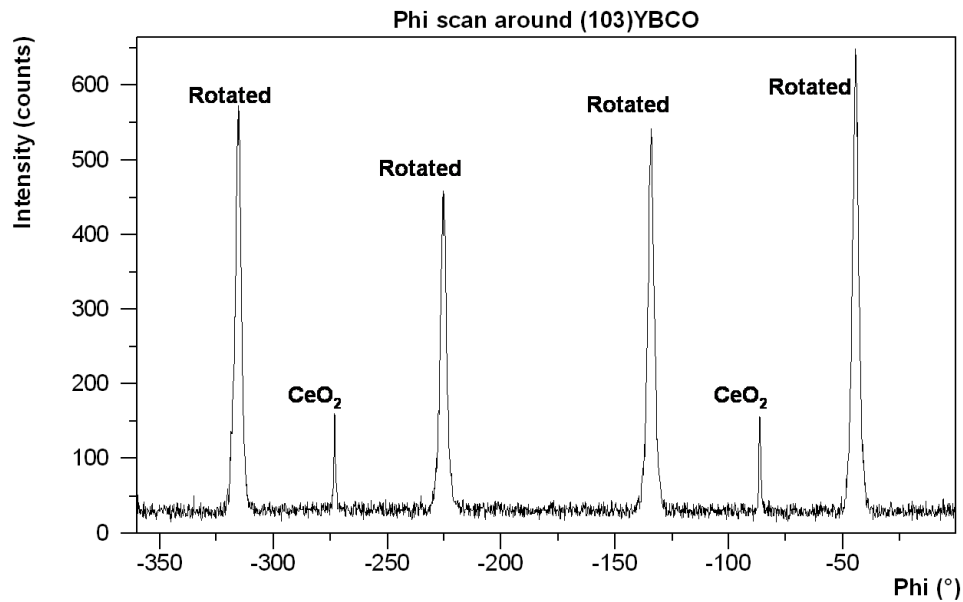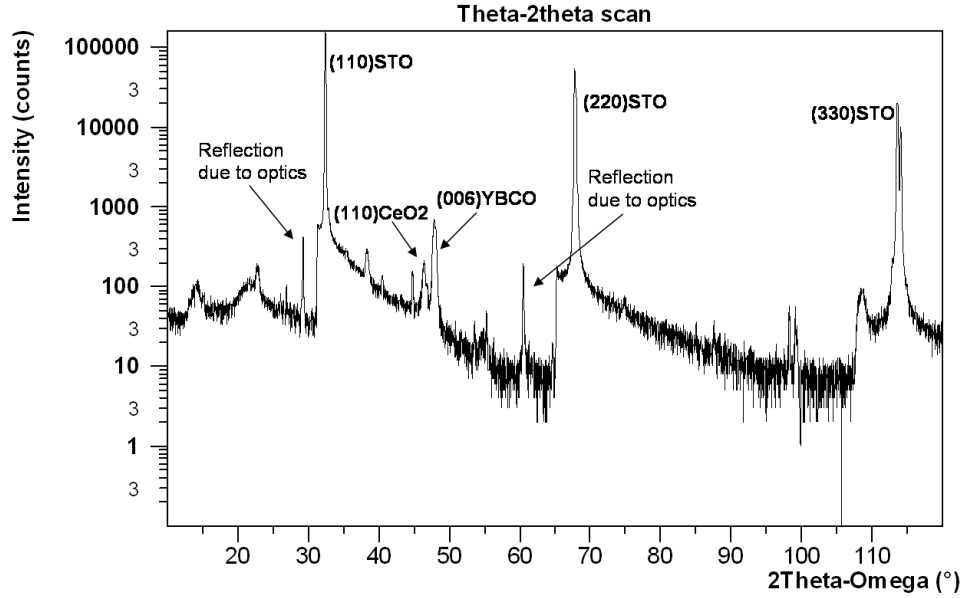
Figure 5.11: (a) Diffractogram for a bilayer CeO2/YBCO film on an etched (110) STO substrate. The CeO2 is completely (110) oriented and in contrary to the film on the non-etched substrate no (111) CeO2 is found.
(b) Diffractogram from a phi-scan of the same sample. Only in-plane rotated (001)YBCO is found.

The surface roughness of the CeO_2 film is another important property for the achievement of good quality (001) YBCO. In general the roughness is <2nm measured peak to peak, but deviations between different samples are found even though the parameters for the deposition are kept the same. In figure 5.12 an AFM picture of a CeO_2

film grown under the conditions presented above is shown together with a topological profile of the surface.

(a)   **(b)**
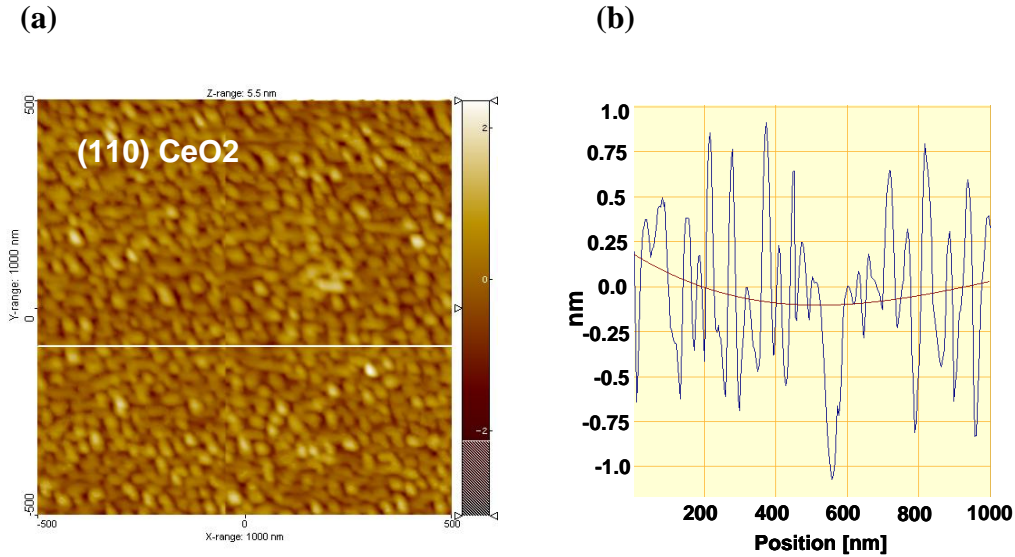
Figure 5.12:   (a) AFM height picture of a (110) CeO2 surface. The scanned area is 1x1 μm^2. (b) A topological profile of the surface in (a) taken along the white line. The peak-to-peak roughness is < 2nm

5.2.2 Growth of YBCO films

To grow fully oriented (001) YBCO films high temperature is required; however, a too high temperature can cause chemical reactions between the CeO_2 and the YBCO at the interface. We have faced this problem by using a template technique. First a YBCO film with a thickness of 20nm is deposited at a lower temperature, then the temperature is raised and the remaining film is deposited at higher temperature to get a fully oriented (001) YBCO film. In our specific case we grow the template at a temperature of 765ºC and the remaining film at 790ºC. At the lower temperature some *a*-axis YBCO grains will be present, but (001) YBCO is still dominating and when the temperature is raised the film grows completely (001) oriented. The oxygen pressure is kept at 0.6 mbar and a frequency of 10Hz for the laser pulses is used. The higher frequency generates smoother films with fewer holes. A possible explanation could be that the faster pulses favor a more uniform nucleation. After deposition of the film it is annealed in 800mbar of oxygen while the temperature is slowly ramped down. Figure 5.13 shows a SEM image of a completely rotated (001)YBCO film with very few holes and a smooth surface. Here it should be emphasized that for the sample in figure 5.13 the CeO_2 and YBCO films were made in situ. For the fabrication of devices the CeO_2 film has to be taken out of the

vacuum chamber and patterned before depositing the YBCO. During the etching of the unwanted parts of the CeO_2 a carbon mask is used to protect the seedlayer that should be left on the substrate. After pattering and removal of the mask the YBCO thin film is deposited. During the patterning procedure the CeO_2 surface is strongly affected by the interaction with the carbon mask and the YBCO film on a patterned seedlayer exhibits more holes and a rougher morphology than the in-situ grown films. Contamination of the CeO_2 surface from the carbon mask plays a large role and it seems like the patterning procedure together with the time the mask is kept on the CeO_2 seedlayer is a crucial factor. The faster the carbon mask is removed the more likely it is to have a clean CeO_2 surface after patterning. However, a full understanding of the mechanism behind the deterioration of the surface properties of CeO_2 films because of patterning is still lacking. Figure 5.14 shows the patterned STO/CeO_2 step after removal of the mask for two different samples. In figure 5.14c the carbon mask has been kept on the CeO_2 film for less than 24h and in figure 5.14a the mask has been left on the film for several days. On a contaminated seedlayer like the one shown in figure 5.14a the (001) YBCO film has a very rough morphology and the GB is characterized by a faceted interface full of holes. The non-contaminated seedlayer can instead provide high quality YBCO films and GBs. The YBCO film grown on the STO/CeO_2 structure in figure 5.14c&d is shown in figure 5.15. Note that due to the granular structure of the (103) YBCO the microstructure of the GB is changed when changing the GB angle θ.
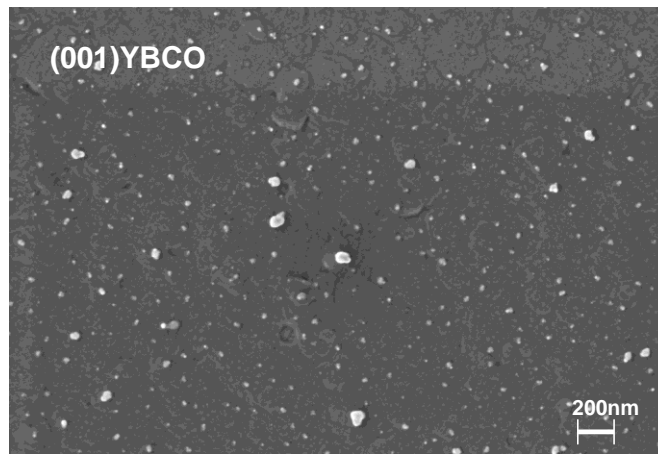
Figure 5.13:   SEM image of a in-plane rotated (001)YBCO film grown in situ on a (110) CeO2 seedlayer.

(a)

(b)

(c)

(d)
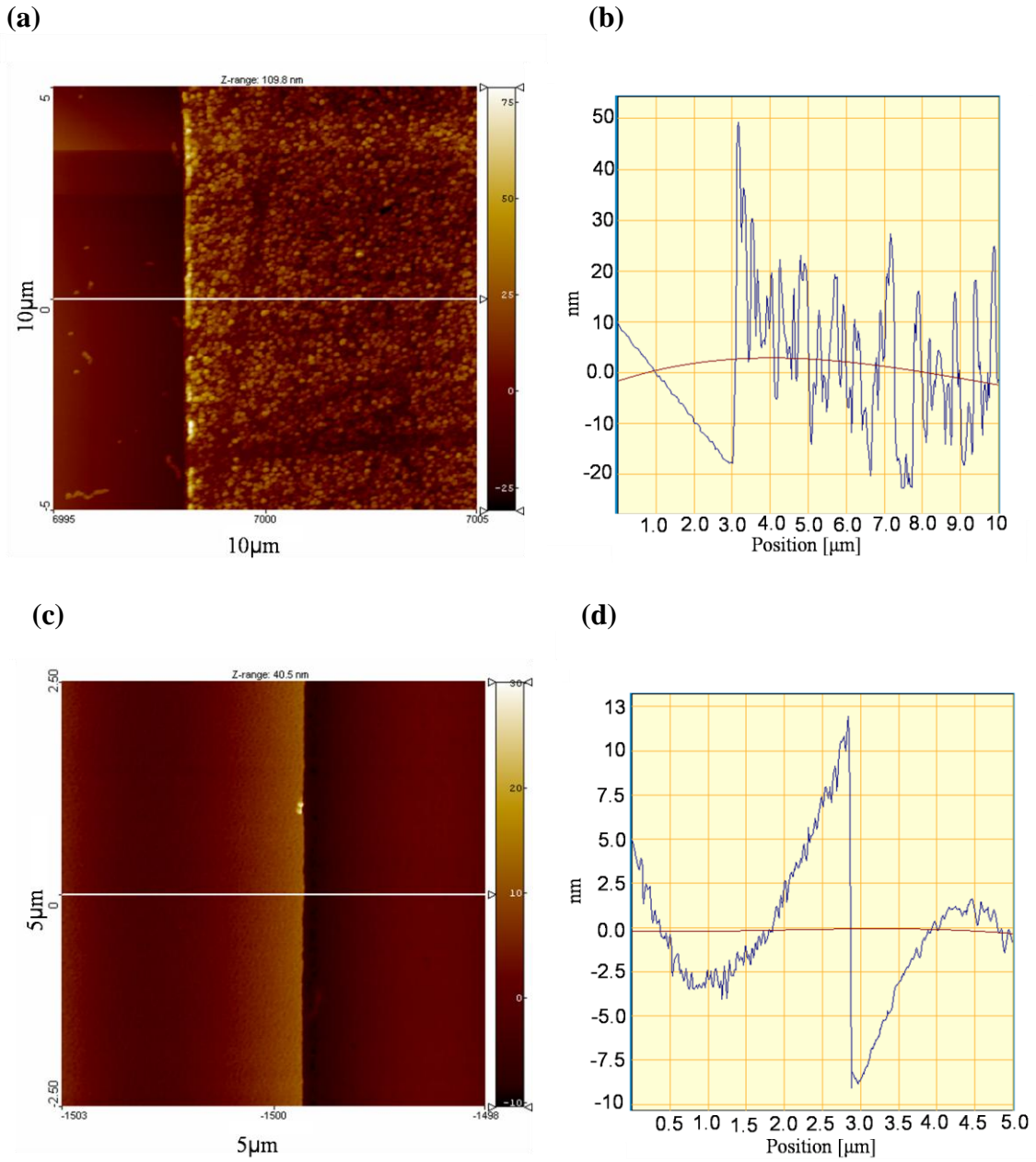
Figure 5.14: AFM images of STO/CeO$_2$ steps. In (a) and (b) the height picture and topological profile for a sample where the carbon mask was removed after several days. The surface of the CeO$_2$ is covered with contaminants from the carbon mask. In (d) and (e) AFM images of a sample where the carbon mask was removed in less than 24 h after its deposition. The surface is smooth and contaminants from the carbon mask appear to be absent.
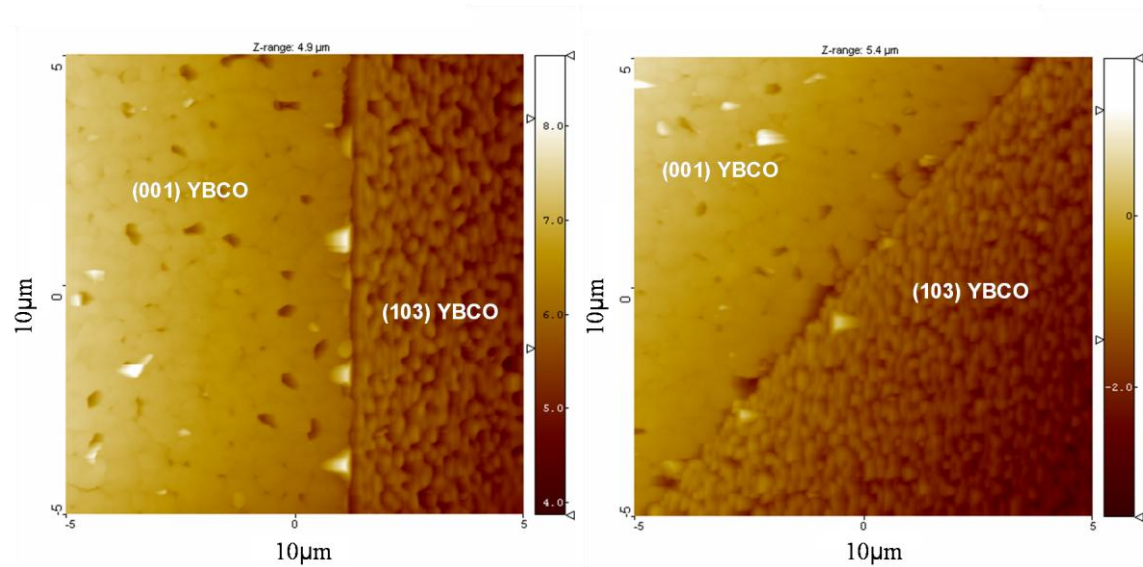
Figure 5.15:   AFM images of the GB between the (103) and (001) oriented YBCO on a patterned (110)STO/(110)CeO$_2$ structure.

5.3 Microanalysis of YBCO growth on patterned CeO2/STO structures

5.3.1 Ideal YBCO growth on (110) STO / (110) CeO$_2$ step structures

On a (110) STO substrate with a vicinal cut and patterned (110) CeO$_2$ seedlayer the preferred growth is a single orientation of (103) YBCO on the substrate and (001) YBCO on the seedlayer. Due to the kinetic of the growth the [100] and [010] directions of the YBCO are fast-growing directions and [001] is the slow-growing direction. This fact determine the characteristic elongated shape in the [010] orientation of (103) grains.

The fast growing directions is indicated by the arrows in figure 5.16. Ideally the single orientation of the (103) YBCO leads to the situation shown in the figure. On one side the Cu-O planes are tilted towards the CeO$_2$ step, on the other side away from the CeO$_2$ step. On the side where the Cu-O planes are tilted away from the CeO$_2$ step a basal plane GB should be formed i.e. the Cu-O planes of the (001) oriented film meet one single *ab*-plane plane of the (103) oriented film, leading to a very well defined and uniform GB (GB1 in figure 5.16). On the other side instead, the two films grow towards each other and meet forming an irregular and rough interface (GB 2).

65
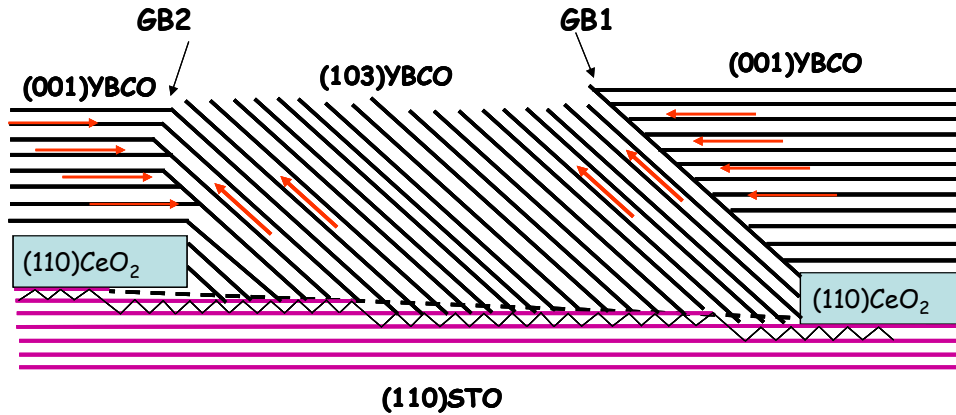
Figure 5.16: Ideal growth on a (110) STO substrate with patterned (110) CeO$_2$ seed layer. The two grain boundaries show fundamentally different structure.

5.3.2 Real YBCO growth on (110) STO / (110) CeO$_2$ step structures

In reality the picture is much more complicated than the ideal model presented above. We have not yet a complete understanding for where and how the nucleation starts and how the film growth evolves, but by performing SEM and TEM analysis on the samples some important conclusions can be made:

1. For samples with big over-etching of the CeO$_2$ film into the STO substrate the YBCO can nucleate on the formed step surface. The nucleation on the surface is always in favor of a flipped orientation of the YBCO. When the etching of the CeO2 seed layer is continued into the STO substrate a new surface is created with a certain angle as seen in figure 5.17. If we consider the side where the basal plane growth is expected in figure 5.16 the situation is as follows. The step slope has in our samples typically an angle of 70º. The microstructure on the surface on the STO slope consists of (100) and (0-10) microfacets. The area of (100) facets will dominate over the area of the (0-10) facets and favor the growth of YBCO with the *ab*-planes tilted towards the step as seen in the schematic picture in figure 5.17. Figure 5.18 shows a TEM image of an over etched step.
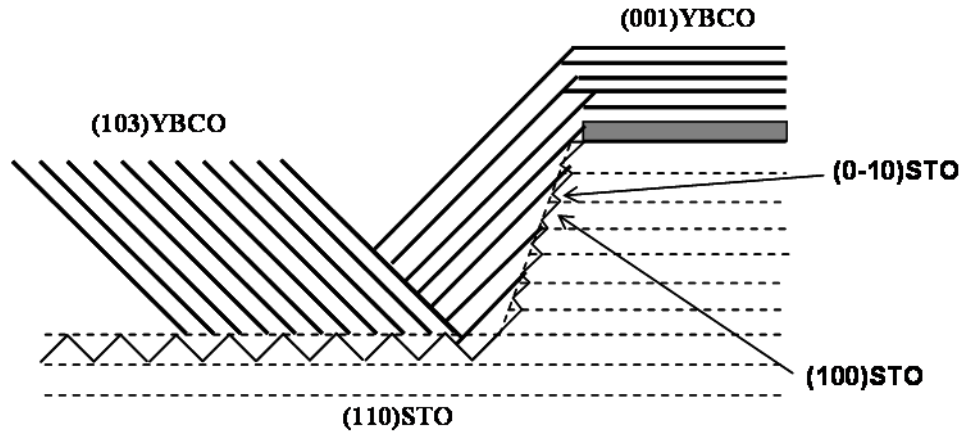
Figure 5.17: Schematic picture of the YBCO growth on an over etched sample. On the slope the (100) STO facets are dominating over the (0-10) STO facets. As a result the (103) YBCO will always grow tilted towards the GB.
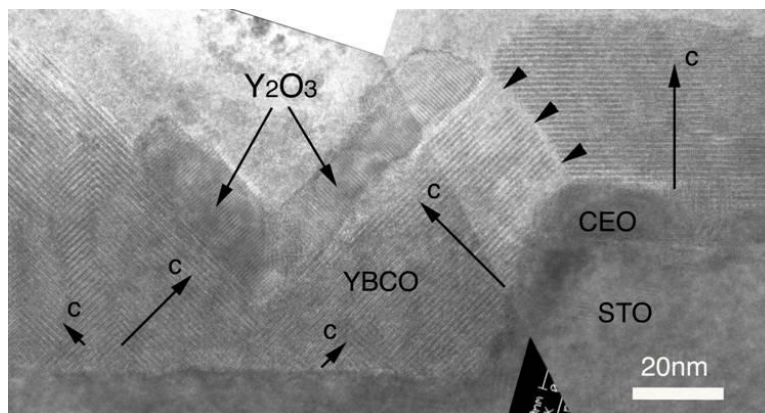
Figure 5.18: TEM image of an over-etched sample where nucleation starts on the step. The situation is identical to the one showed in the schematic picture. Note that in this particular case a certain roughness on the STO surface have caused flipping of the YBCO growth on the horizontal surface. For this sample the vicinal cut was 3.5° and by increasing the vicinal cut to 6° this situation with flipping YBCO growth can be avoided.

2. Re-deposition during etching of the seedlayer forms a new (110) STO surface close to the step. The angle between the surface and the (110) STO plane increases further on one side of the CeO_2 while on the other side the re-deposition reverses the angle between the surface and the (110) STO planes (see figure 5.19). As a result the effective vicinal cut is influenced by the formation of the "new" re-deposited surface. Consequently the *ab*-planes of the (103) YBCO always grows tilted towards the CeO_2 seed layer.
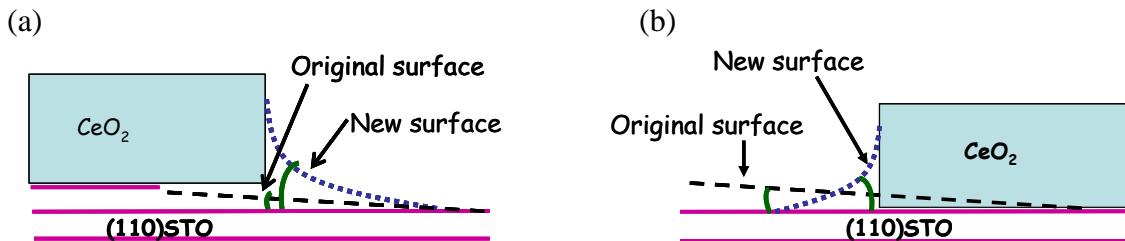
Figure 5.19:   In (a) the "new" surface formed close to the step due to re-deposition increases the effective vicinal cut. In (b) instead, the "new" surface reverses the angle of the vicinal cut and the YBCO will grow with the *ab*-planes tilted towards the step.
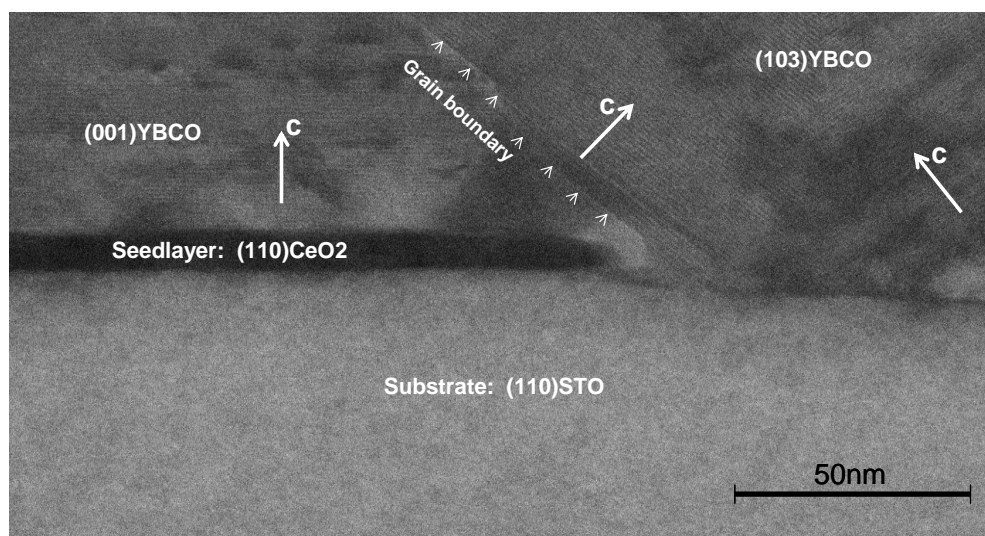
Figure 5.20:   TEM image that shows the flip of the (103)YBCO close to the CeO2 step. The flip is due to the formation of a new surface close to the step possible from re-deposited material during the etching.

3. In some cases the nucleation of YBCO on the CeO_2 film seems to be delayed close to the step. A reason could be that the nucleation are favored on the *ab*-planes of the (103) oriented YBCO rather than on the CeO_2. As a result the (103) YBCO film has time to grow up over the height of the step before the GB are formed. That is in favor of a basal plane growth. The TEM picture in figure 5.21 shows formation of a basal plane up to a certain thickness.
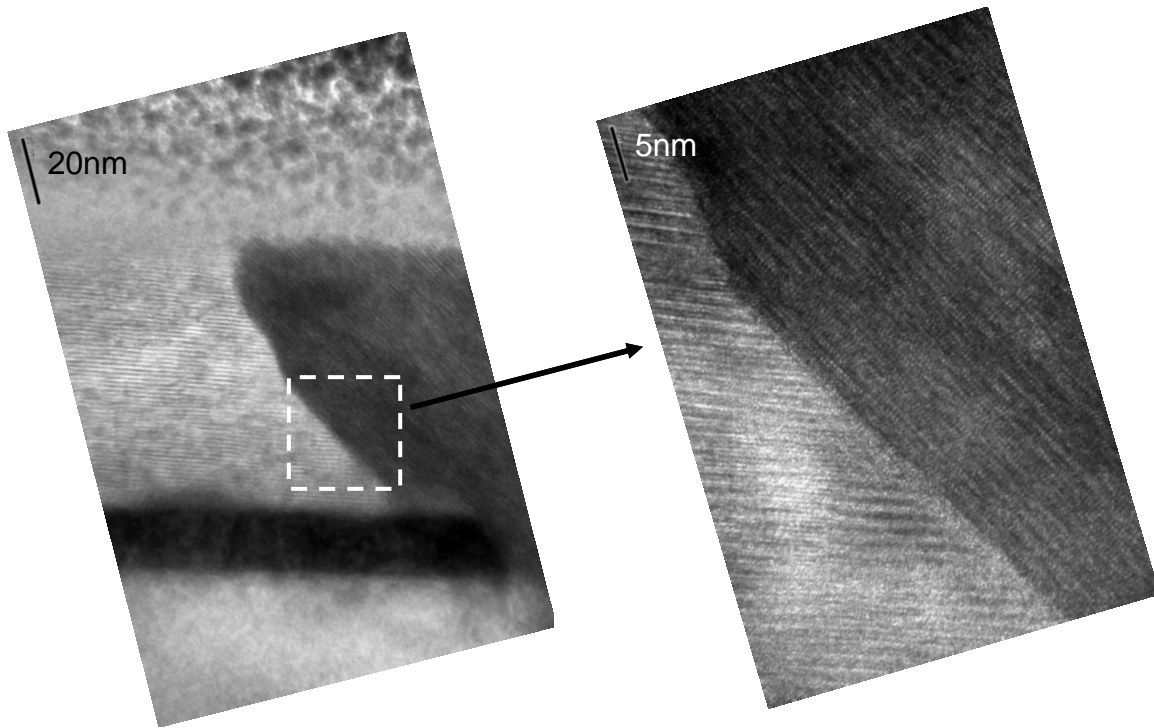
Figure 5.21:   TEM image of the GB. The basal-plane growth is around 50nm. Above that height the fast growing directions of the two domains meet forming a more irregular interface.

5.3.3 Conclusions

From the considerations above it follows that the desired ideal basal-plane GB is not possible to achieve since the YBCO always grows with the *ab*-planes tilted towards the seedlayer. However, if the over-etching is not severe so no nucleation takes place on the step itself a basal plane will still be formed as shown in figure 5.21. The basal plane growth has only a certain thickness that in our samples has been found to be around 60nm. Above that thickness the (001) YBCO and the (103) YBCO will meet while growing towards each other and form an irregular surface. The basal plane growth found here could be the key for producing reproducible GB Junctions in the future. Figure 5.22 shows a sketch of a real sample with optimized conditions. From this picture it appears more favorable to pattern the devices on the GB where there is no flip for the (103) YBCO and hence avoid extra grain boundaries in the (103) YBCO domain.
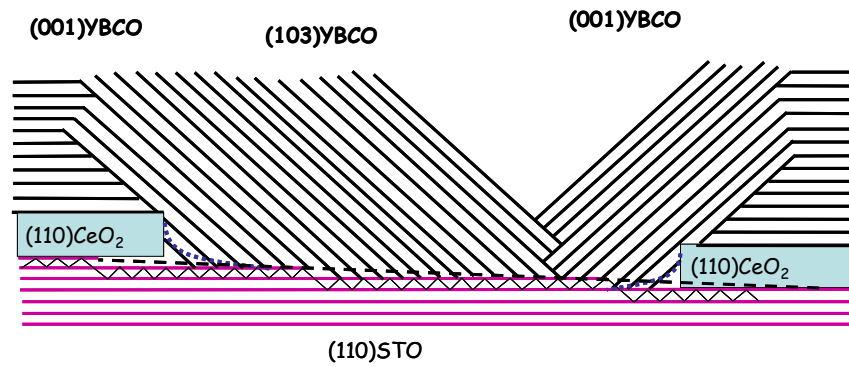
Figure 5.22: A schematic picture of the real YBCO growth on a (110) STO / (110) CeO$_2$ step structure. One orientation of the (103) YBCO is selected on the major part of the sample, but close to the CeO$_2$ step it flips orientation so both sides present the same growth-behavior. Note the basal-plane growth at the GB up to a certain thickness.

London penetration depth and kinetic inductance

The London penetration depth was introduced in chapter 1. It is defined as the distance a magnetic field can penetrate into a superconductor and it is an important property of the material. Not only does it determine the "confinement" of the cooper pairs in a superconducting electrodes, but it also influences the magnetic filed dependence of the critical current in single junctions by effecting both the Josephson penetration depth, λ_J, and the effective area [23]. In applications like SQUIDs the effect is even more pronounced. The value of the London penetration depth influences the effective loop area in the SQUID and also the loop inductance, due to a kinetic contribution. Indeed the SQUIDs sensitivity to magnetic field makes it very responsive to any contribution to the total inductance. Moreover recent measurements of the plasma frequency in a biepitaxial YBCO junction fabricated on STO/CeO$_2$ clearly showed that the phase dynamics in such junctions could not be described by the usual RCSJ model (see chapter 2). Instead one has to use an extended model, where the junction is shunted by a series LC circuit [35,36] The shunting capacitance can be attributed to the large relative permittivity of the STO substrate. The stray inductance of the YBCO electrodes, instead, may have different origins related to the microstructure of the grain boundary (filamentary transport [37]), intrinsic Jospehson effect between *ab*-planes and/or to the anisotropy of charge transport [38]. This last point is particularly important when the current transport has a significant *c*-axis component in the (103) electrode. Since YBCO has a large London penetration depth in the *c*-axis direction, the stray inductance may have a quite significant contribution coming from the kinetic term $L_{kin} \propto \lambda^2$ [7].

This chapter is dedicated to experiments carried out in order to investigate the London penetration depth and the kinetic inductance in our kind of biepitaxial samples. We have measured the inductance in the (103) electrode of SQUIDs designed for this purpose. Numerical simulations have been carried out to account for the inhomogeneous current distribution in the electrodes and by fitting the numerical simulations to the measured

total inductance, the London penetration depth and the kinetic contribution to the total inductance can be obtained.

6.1 London penetration depth as a function of GB angle

As a consequence of the anisotropic unit cell in YBCO the value of the London penetration depth strongly depends on the direction of the screening currents with respect to the crystallographic axes. For optimally doped YBCO bulk samples the penetration depth is typically 130-140nm for screening currents in the *ab*-plane (λ_{ab}) [39,40] and around 1µm for screening currents in *c*-axis direction (λ_c) [39-41]. The penetration depth is highly dependent on the doping level and for thin films values as large as 550nm for λ_{ab} and 7.80 µm for λ_c have been reported for samples with a critical temperature of 42K and 53K respectively [41,42].

The kinetic inductance is associated with the kinetic energy of the current carriers and is dependent on the London penetration depth. When the current transport has a component in the c-axis direction, which is typically the case for biepitaxial (103) electrodes, the kinetic contribution to the total inductance can be substantial.

The relation between a dc supercurrent and the phase gradient in a superconductor is given by the London equation according to: $\nabla \varphi = (\lambda_L^{\,2} \vec{J} \mu_0 + \vec{A}) 2\pi / \Phi_0$. In the following we consider only the kinetic contribution to the phase gradient by setting the vector potential $\vec{A} = 0$. This relation is valid when the penetration depth λ_L is isotropic. For an arbitrary direction of the current in a superconductor with anisotropic penetration depth the London penetration depth has to be described by a tensor resulting in an expression for the phase gradient [43,44] :

$$\vec{\nabla} \varphi = \begin{pmatrix} \lambda_a^{\,2} & 0 & 0 \\ 0 & \lambda_b^{\,2} & 0 \\ 0 & 0 & \lambda_c^{\,2} \end{pmatrix} \begin{pmatrix} J_x \\ J_y \\ J_z \end{pmatrix} \frac{2\pi\mu_0}{\Phi_0} , \tag{6.1}$$

where λ_a, λ_b and λ_c are the London penetration depth in the a, b and c directions defined in figure 6.1 and J_x, J_y and J_z are the current density in direction x, y and z, also defined in figure 6.1.
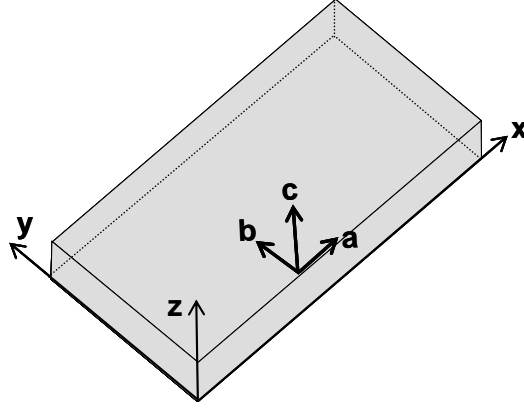
Figure 6.1:   Electrode with the crystallographic axes a, b and c aligned with the
              coordinates of the electrode x, y and z.

The electrode is fixed to the coordinate system so x gives the length, y the width and z the thickness of the electrode. When the electrode is rotated on the sample the crystallographic axes a, b and c are rotated with respect to the x, y, z axes. In a (103) YBCO electrode the crystallographic orientation is characterized by a 45° rotation around the x-axis as pictured in figure 6.2a. In our case the orientation of the electrode on the sample is defined by an angle θ which is chosen to correspond to the GB angle for junctions patterned on the sample. To account for a varying θ, as defined in figure 6.2b an additional, arbitrary, rotation of the crystallographic axes by an angle θ around the z-axis has to be included. Hence the general expression for the phase difference induced by the inductance for a current of arbitrary direction is given by a 45° rotation of the λ^2 tensor around the x-axis followed by a rotation of θ of the λ^2 tensor around the z-axis. If the current is sent in the x-direction and is considered to be uniformly distributed and without deviation from the initiated trajectory the phase gradient can be written:

$$\vec{\nabla}\varphi = \begin{pmatrix} \cos^2\theta \cdot \lambda^2_{ab} + \sin^2\theta\left(\frac{1}{2}\lambda^2_{ab} + \frac{1}{2}\lambda^2_{c}\right) \\ -\sin\theta\cos\theta \cdot \lambda^2_{ab} + \sin\theta\cos\theta\left(\frac{1}{2}\lambda^2_{ab} + \frac{1}{2}\lambda^2_{c}\right) \\ \sin\theta\left(-\frac{1}{2}\lambda^2_{ab} + \frac{1}{2}\lambda^2_{c}\right) \end{pmatrix} \mathbf{J}_x \frac{2\pi\mu_0}{\Phi_0} \qquad (6.2)$$

Form equation 6.2 an analytical expression for the effective London penetration depth can be derived according to:

$$\lambda^2_{eff} = \lambda^2_{ab}\cos^2\theta + \frac{1}{2}\left(\lambda_c^2 + \lambda_{ab}^2\right)\sin^2\theta \qquad (6.3)$$

Note that this expression is only valid when the current flow is confined to the x-axis direction. The kinetic inductance of an anisotropic superconductor can now be written as [7]:

$$L_{kin} = \mu_0 \lambda_{eff}^2 \frac{l}{wd},$$

(6.4)

Where l is the length, w is the width, and d is the thickness of the electrode.
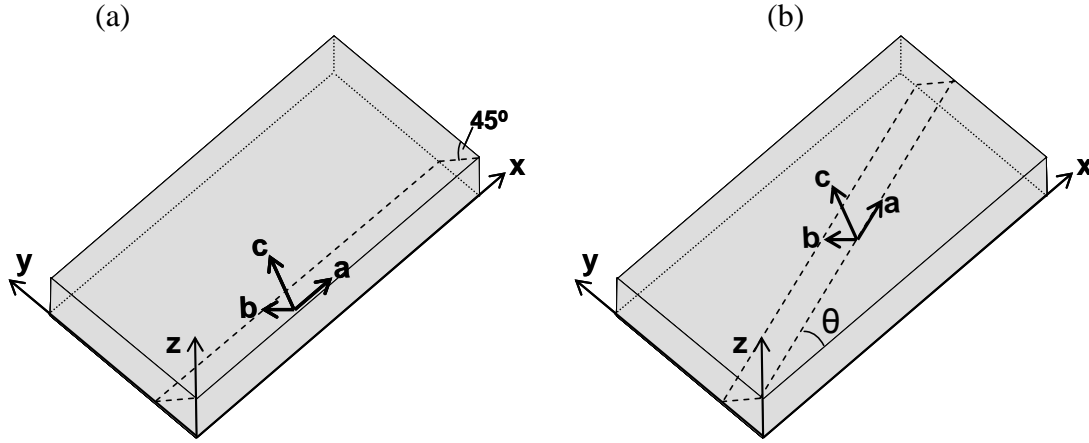
Figure 6.2:   (a) The 45° rotation around the x-axis accounts for the [100]-45° tilt of the *ab*-planes in the (103) electrode. (b) An arbitrary rotation θ around the z-axis introduce a directionality of the current with respect to the crystallographic axes.

6.2 Experimental determination of the kinetic inductance and London penetration depth

One method to measure the inductance of a superconducting strip is to implement it into a SQUID configuration. In figure 6.3 a schematic of the SQUID used for the inductance measurements is depicted. By sending a current through the lower electrode via the two injection leads one induces a phase difference between the two junctions according to:

$$\Delta \varphi = L_{103} \cdot I_{ctrl} \frac{2\pi}{\Phi_0}$$

(6.5)
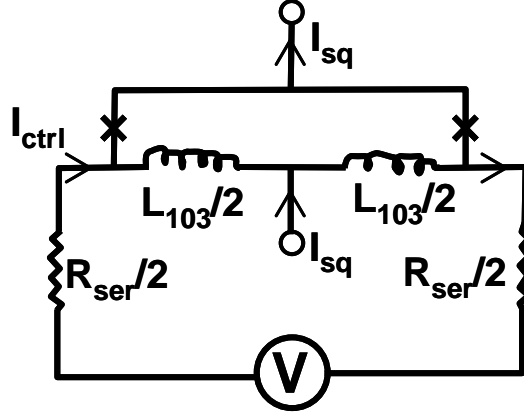
Figure 6.3:   The corresponding circuit for the SQUID with injection lines. A control current I_{ctrl} sent through the injection lines induces a phase difference in the electrode that in turn modulates the critical current of the SQUID.

For Josephson devices with the biepitaxial structure discussed in chapter 5, only the kinetic inductance of the (103) electrode is effected by a change of θ. In the (001) electrode the current transport will always be in the *ab*-plane regardless of θ, keeping the kinetic inductance unchanged.

To determine the inductance in the (103) electrode a known current was sent through the electrode via the injection lines while the IV-curves of the SQUID were recorded. The critical current of the SQUID is a 2π periodic function of the phase difference between the two Josephson junctions [7]. Hence, if the control current needed to modulate the phase difference one period is ΔI, the electrode inductance can be extracted from the period of the critical current pattern: $L_{103} = \Phi_0 / \Delta I_{ctrl}$. The inductance measured here corresponds to the total inductance of the electrode given by:

$$L_{103} = L_{geo} + L_{kin} = L_{geo} + \mu_0 \frac{l}{wd} \lambda^2_{eff} \tag{6.6}$$

where L_{geo} is the geometric inductance related to the magnetic field generated by the current flowing through the electrode.

6.2.1 SQUID design

To enhance the inductance in the 103 electrode we used a SQUID geometry elongated in the direction parallel to the GB (see figure 6.4). The SQUID hole is $24 \times 1 \mu m^2$, the width of the Josephson junctions 2.7 μm and the width of the (103) electrode is 11 μm. The two injection lines connected to the (103) electrode have a width of 2.7 μm. A set of SQUIDs with θ ranging from 0° to 90° with a spacing of 10° was patterned, all on the same sample. An optical image of a SQUID with θ = 30° is shown in figure 6.4. In figure 6.5 schematic pictures of how the current is transported with respect to the *ab*-planes for 0° and 90° GB angle is shown.
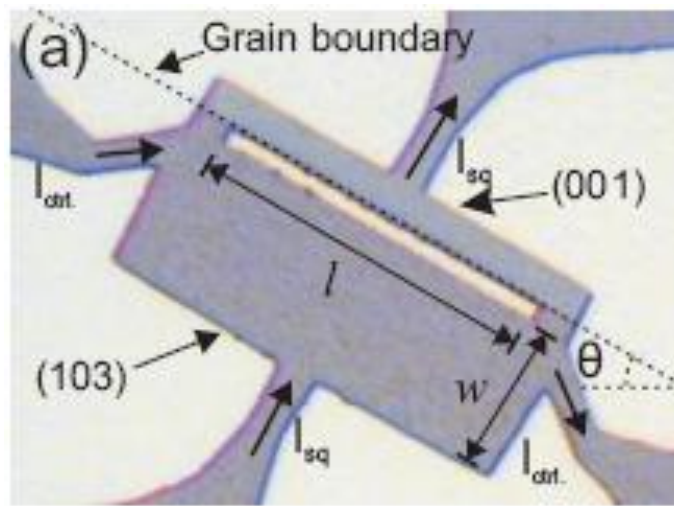
Figure 6.4:   Optical micrograph of a SQUID with θ=30°. The grain boundary is indicated by the dotted line. The distance *l* between the junctions is 24μm and the (103) electrode width is *w* =11μm
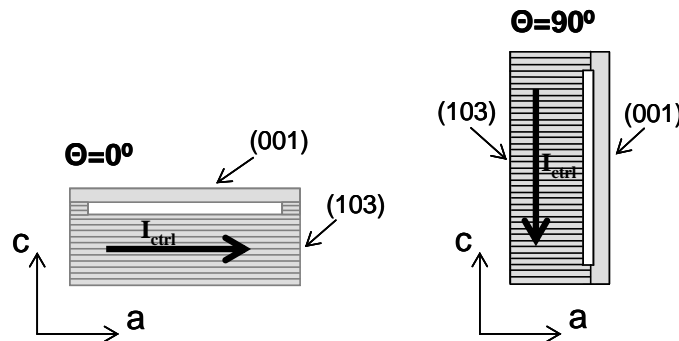
Figure 6.5:   Schematic sketch of the current transport in the two extreme orientations of the SQUIDs when θ = 0° and θ = 90°. The lines in the (103) electrode represents the YBCO Cu-O planes (here it should be noted that the Cu-O planes have a 45° tilt around the a-axis). For θ = 0° the control current

through the (103) electrode flows in the *ab*-plane while for θ = 90º the current flow has equal contributions in *c*-axis direction and b-direction (due to the 45º tilt around the a-axis).

6.2.2 Simulations of current distribution

The analytical expression for the total inductance given in equation 6.6 is only valid for a uniform current distribution in the electrode. In our geometry, with current coming from the narrow injection leads, the current will redistribute along the (103) electrode having components both parallel and perpendicular to the GB line. Therefore the current distribution has to be numerically calculated taking into account the anisotropy of the London penetration depth and the finite width of the current injection leads. Here we followed the approach developed by M. M. Khapaev Jr descibed in [44]. We extended the approach taking into account an anisotropic London penetration depth to calculate the current distribution in the (103) electrode. The software COMSOL was used to perform the numerical finite element calculations. From the numerically determined current distribution in the (103) electrode we can extract both the kinetic and geometric inductance.

In figure 6.6 the numerical simulations for the current distribution in the (103) electrode for different angles θ is presented. The left row represents the geometry used in the experiment where the position and width of the injection lines are represented by the black marks on the first electrode. The color scale is the absolute value of the current density and the arrows correspond to the direction of current flow. From the simulations one can see that the current density is rather uniform for angles θ ≥ 40º. For smaller angles the position of the injection lines becomes increasingly important since the current tend to follow the *ab*-planes of the electrode rather than distribute across the full width. In the graph right below the current distribution maps the solid symbols corresponds to the kinetic inductance extracted from the current distribution and the solid line is the kinetic inductance calculated by using the analytical expression for λ_{eff}. In the column to the right in figure 6.6 the same simulations have been done for a geometry where the injection lines are equally broad as the electrode. In this case the direction of the current flow is in x-axis direction and the analytical expression coincides very well with the numerically obtained one as can be seen in the bottom right panel of figure 6.6.

Figure 6.6   The current distribution for the (103) electrode for different angles. The color scale corresponds to the absolute value of the current and the arrows indicate the direction. The simulations have been carried out for narrow

injection lines (left column) and broad injection lines (right column). In the graphs the kinetic inductance extracted from the numerical simulation (solid symbols) and the analytical expression (solid line) is plotted for the two different geometries.

6.2.3 Results from measurements

The modulation of the critical current as a function of the injection current was measured for SQUIDs with GB angles ranging from $\theta = 0^\circ$ to $\theta = 90^\circ$. From the periodicity the total inductance was calculated according to the relation: $L_{103} = \Phi_0 / \Delta I_{ctrl}$. Figure 6.7a shows the critical current as a function of the injection current for two SQUIDs with $\theta = 40^\circ$ and $\theta = 90^\circ$. As expected the modulation period is shorter for the higher GB angle due to the larger inductance. The measured inductance versus GB angle is plotted in figure 6.7b. The inductance changes from 13pH at $\theta = 0^\circ$ to 265pH at $\theta = 0^\circ$, which is an increase by a factor of 20.

To extract the London penetration depth as a function of angle from the measurements the numerical simulations have been used. From the current distribution the kinetic and geometric parts of the total inductance can be calculated and by finding the best fit with the total inductance measured in the experiment we obtain a value for λ_{ab} and λ_c.

The best fit to the measured inductance values is given by $\lambda_{ab} = 270nm$ and $\lambda_c = 4.4\mu m$ and is shown by the solid line in figure 6.7b. Both values are considerably larger than the reported values for optimally doped films. This is in accordance with the fact that the transition temperature for the film after fabrication of the devices was 71K which is a strong indication that the large penetration depths are due to oxygen depletion. If the reduced T_c is taken into account λ_{ab} and λ_c are in good agreement with the values reported in $\lambda_{ab} = 250nm$ for Tc=70K and which reports $\lambda c = 3.4$ and $5.5\,nm$ for a film with Tc of 78 and 58K respectively. In figure 6.7c the effective London penetration depth is plotted as a function of the GB angel θ for $\theta \geq 40^\circ$.

The geometric inductance extracted from the numerical simulations is $L_{geo}= 6.3$pH. The dashed line in the figure corresponds to the analytical expression of the total inductance as a function of θ. For θ larger than 40° the correlation is very good while it deviates at lower angles due to the non uniform current distribution.

(a)

(b)   **(c)**
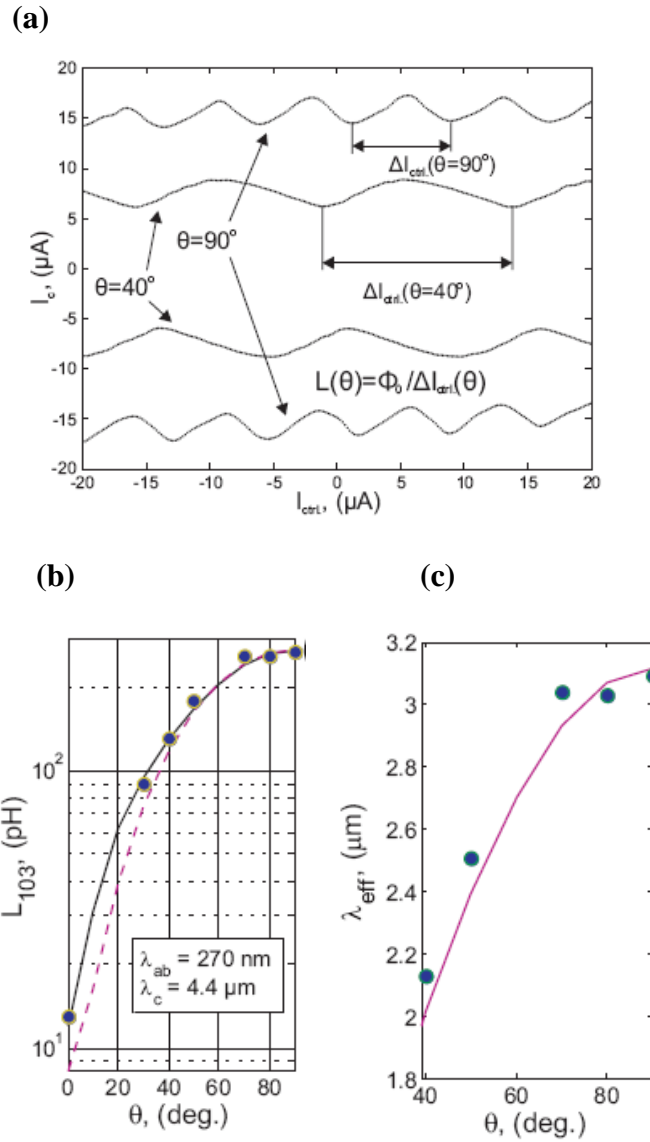
Figure 6.7:   (a) The modulation of the critical current as a function of the control current I_{ctrl} for two SQUIDS with GB angle $\theta = 40°$ and $\theta = 90°$. The measurements were carried out at 280mK. (b) The total inductance in the (103) electrode, $L_{(103)}$, plotted as a function of θ. The solid line represents the best fit of the inductance with respect to angle θ by numerical calculation of the current distribution in the (103) electrode. The best fit is

given with $\lambda_{ab} = 270nm$ and $\lambda_c = 4.4\mu m$. The dashed line is the inductance calculated from the analytical expression given in equation 6.3. (c) Extracted values of the London penetration depth for $\theta \geq 40°$. The solid line is the analytical expression given in equation 6.3.

6.3 Influence of θ on the SQUID diffraction pattern

The period (with respect to the externally applied magnetic field) of the modulations in the diffraction pattern of a SQUID is determined by the effective loop area. The modulation period is equal to one flux quantum and each time an integer number of flux quanta enters through the loop a maximum in critical current is reached. The flux through the loop is given by: $\Phi = A_{eff} \cdot B$, where A_{eff} is the effective loop area and B is the external magnetic field. If the effective loop area is increased due to a larger London penetration depth the magnetic field required to reach $\Phi = \Phi_0$ is smaller and the modulation period is reduced with respect to the applied field B. As a first approximation the effective loop area is given by the geometric loop area plus the area of the electrodes that are penetrated by the magnetic field. The last part is determined by the London penetration depth.

In figure 6.8a the Ic(B) pattern for four SQUIDs at different GB angles θ are shown. The geometric loop area for the SQUIDS is $10\mu m^2$ and since the London penetration depth in c-direction can reach several microns the influence of the London penetration depth on the effective area is considerable. 6.8b shows a sketch of the geometry of the SQUIDs and their orientation at θ=25° and θ=75°. The scale of the external magnetic field is the same in all four graphs but the grain boundary angle and hence the orientation of the electrodes is changing. Note that the effect will only be important in geometries where the dimensions of the geometrical loop are small enough for the London penetration depth to have a substantial impact on the total effective area.
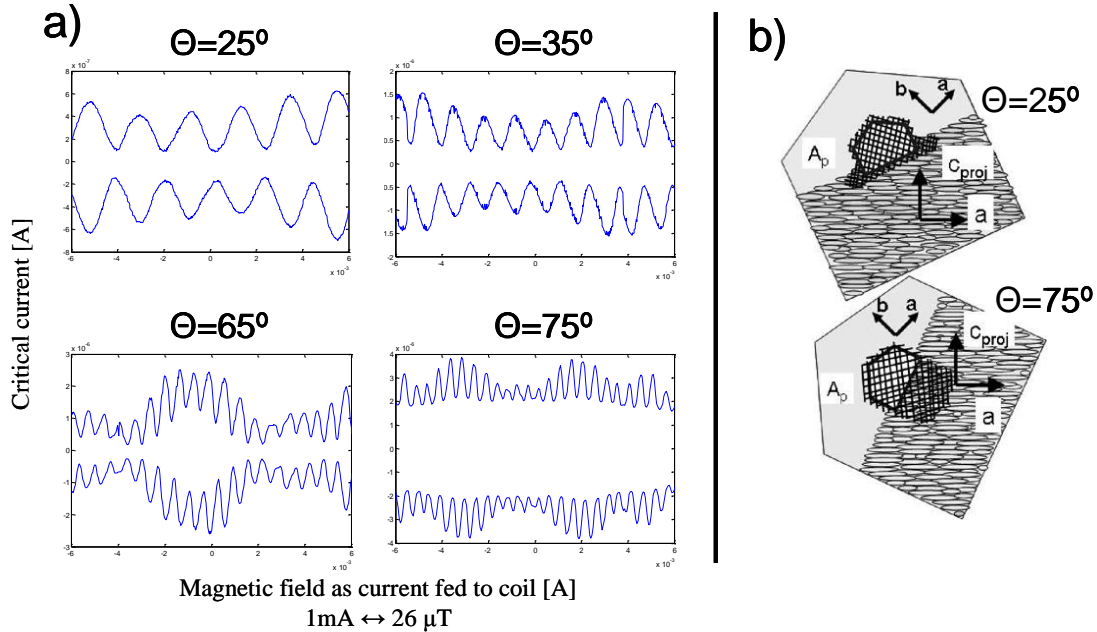
Figure 6.8: a) Critical current as a function of applied magnetic field for four SQUIDs with different grain boundary angle θ. The number of modulations increases with increasing θ due to the enlargement of the effective area. The larger effective area is a result of an increased effective penetration depth when, for increasing θ, the current through the (103) electrode increases its component in the *c*-axis direction. In b) a sketch of the devices and the orientation of the crystallographic axis of the YBCO films are presented. The granular electrodes represent the (103) oriented YBCO film and the dark grid the effective area.

6.4 Conclusions

We found that the inductance of the (103) electrode varies by a factor of 20 as a function of the in-plane angle. This is due to the large anisotropy of the London penetration depth in YBCO. It is an important result since it shows that the kinetic inductance gives a very large contribution to the total inductance for certain orientations of the electrodes. In applications like SQUIDs this has to be considered when designing the samples. A large loop inductance may shift the $I_c(B)$ pattern of the SQUID making it difficult to distinguish for example between 0-SQUIDs and 0-π-SQUIDs. We have also seen that the anisotropy of the London penetration depth effects the effective area of a SQUID loop which can give a significant change in modulation period for SQUIDs that are identical in the design but with different orientations on the chip.

0-π-Junctions

The fabrication of 0-π-junctions was one of the main goals during this thesis. Such junctions have been suggested as a complement to conventional Josephson junctions in a new family of logic circuits based on the Josephson effect [45]. New ideas to implement 0-π-junctions in Rapid Single Flux Quantum (RSFQ) circuits suggest that they could reduce the need for bias lines and therefore reduce the dissipation [46]. It is possible to fabricate π-junctions also from LTS materials by introducing a ferromagnetic layer in the barrier [9]. For such junctions an arbitrary intrinsic phase shift can be achieved by choosing the right thickness of the ferromagnetic barrier. In the ferromagnetic π-junctions the phase shift depends on temperature [10]. In 0-π-junctions based HTS instead, the phase shift is stable in temperature since it is a fundamental property of the d-wave OP.

7.1 Sample design

The design of the sample was decided in the view of a number of important aspects:

- The magnetic length of the junctions have to be short enough to show the complementary behavior for the $I_c(B)$ pattern with a maximum versus a minimum in critical current at zero magnetic field for a 0-junction and a 0-π-junction respectively.

- Junctions with different GB angles should be measured to investigate the influence of the GB microstructure on the transport properties of 0-π-junctions.

- For each 0-π-junction a reference 0-junction has to be made with the same GB angle for comparison. It has been an important goal to prove that it is possible to fabricate 0-π-junctions by will, in spite of the random micro-faceting.

The final design of the sample is shown in figure 7.1. The GB angle is altered 5° between each row of junctions and range from 5° to 80°. For each angle two 0-π-junctions and two reference 0-junctions were patterned. Each junction is 10 μm wide and the 0-π-junctions consist of two 5 μm long facets, while the 0-junctions have one single 10 μm facet. The 0-π-junctions are patterned so both facets have the same type of GB interface. The thickness of the film is estimated to be around 1600Å. The critical temperature was around 89K which indicates a good film quality.
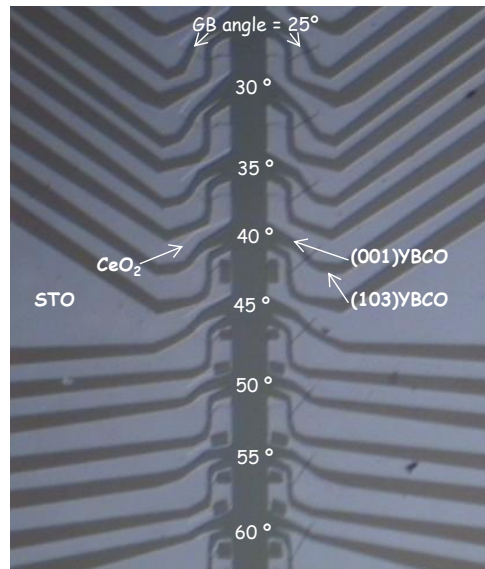
Figure 7.1:   Optical microscopy image showing the layout of the sample. The CeO_2 is patterned in such a way that the grain boundary angle is changes by 5° between each row of junctions. Two 0-π-junctions (corner junctions) and two 0-junctions (edge junctions) are patterned for each GB angle.
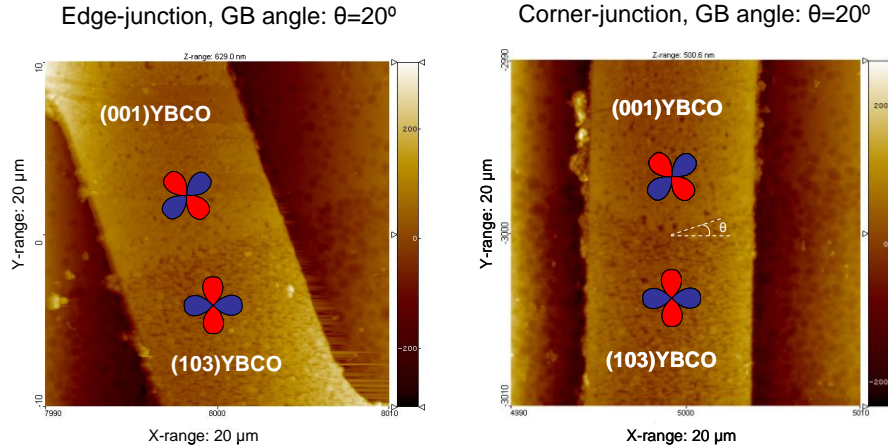
Figure 7.2:   Atomic force microscopy images of a 0-junction and a 0-π-junction respectively.

7.2 Results

7.2.1 0 vs. 0-π behavior

The measurements of the critical current as a function of magnetic field clearly show the expected complementary behavior for a majority of the junctions. The 0-π-junctions show a reduction of the critical current at zero magnetic field while the reference 0-junctions show a maximum.

In total 57 junctions were measured for different GB angles. 43 of them behaved in consistence with their design giving a yield of 75% successfully fabricated junctions on this sample. It should also be noted that the junctions that are deviating from the expected behavior, to a majority, can be found in areas where the GB angle is close to "tunneling in the node"- angles. For such angles also small deviations from the nominal GB angle may cause a change from a 0 to a π facet. Selecting angles far away from such orientation would, without doubts, increase the percentage of successful devices. Figure 7.3 shows the plots of the $I_c(B)$ measurements for the junctions shown in figure 7.2 at a temperature of 40K. The junctions have a GB angle of 20º.
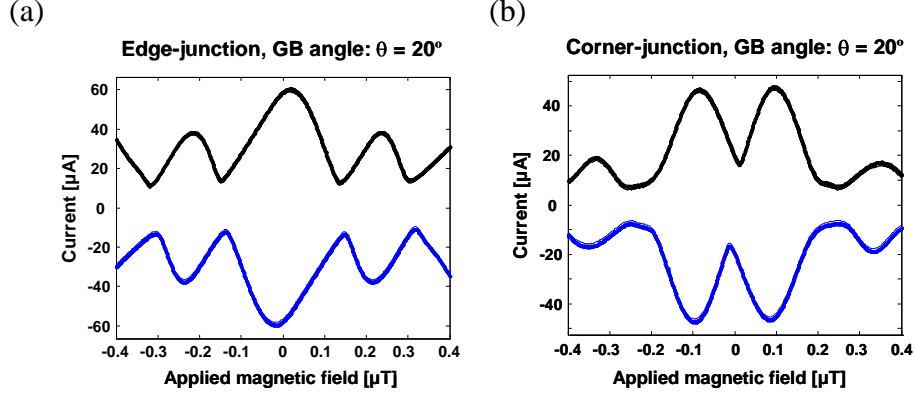
Figure 7.3:   Critical current versus applied magnetic field for a 0-junction (a) and a 0-π-junction (b). The expected behavior with a maximum respective a minimum of the critical current for zero magnetic field is clearly shown here. The junctions were measured at 40K.

7.2.2 Critical current as a function of GB angle

The critical current as a function of the GB angle for d-wave junctions follows the Sigreist-Rice formula presented in equation 2.20. In the biepitaxial junctions presented here equation 2.20 can be rewritten in terms of GB angle [47]:

$$I_c = I_{c0}\left[\frac{\sin 2\theta(2-\cos^2\theta)(1-3\sin^2\theta)}{(1+\sin^2\theta)}\right] \tag{7.1}$$

Where θ is the GB angle measured with respect to the in plane [001] direction of the substrate and I_{c0} the maximum critical current density (i.e. the critical current density for tunneling lobe to lobe).

In figure 7.4a the $I_c(\theta)$ values are plotted for the 0-junctions. The solid line is the theoretical expression 7.1. It is clear that the GB angle has an influence on the critical current and the Sigreist-Rice dependence is followed rather well especially for higher angles. However, for junctions close to 35° the measured values deviate from the theoretically predicted and show higher critical current than expected. This might be due to microfaceting and indeed an anomalous Fraunhofer pattern is often found for these angles.

A somewhat unexpected result was that the 0-junctions and the 0-π-junctions respond quite differently to the change in GB angle. While the 0-junctions follow the Sigreist-Rice dependence on the GB angle the 0-π-junctions dependence appears to be quite scattered. The critical current as a function of the GB angle is plotted for the 0-π-junctions in figure 7.4b. Note that for lower angles the critical current lies in the same interval as that for the 0-junctions. For higher angles instead the correspondence is

86

completely lost. A possible explanation lies on the fact that the lithography is more difficult for the sharp corners and hence the quality of the seed layer edges and therefore of the GB can vary by changing the angle.

(a)

(b)
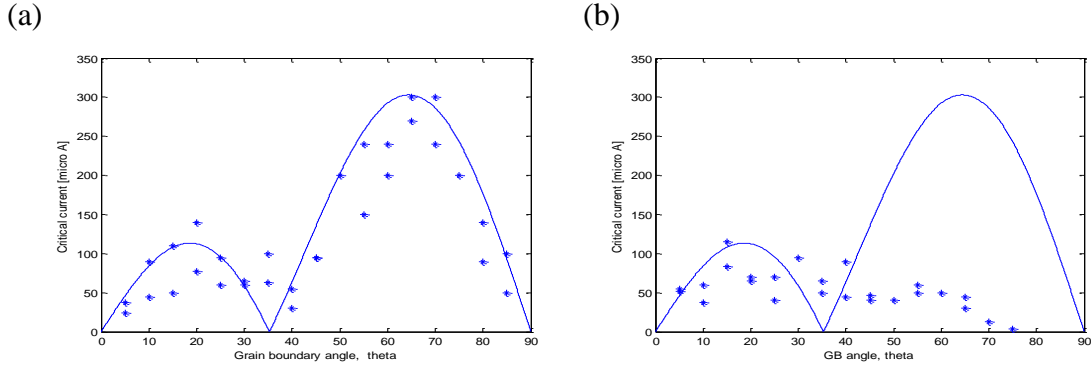
Figure 7.4:   Critical current as a function of the angle for the 0- junctions. The solid line represents the theoretical angle dependence of the critical current. (a) A quite good agreement with the theoretical predictions is shown. (b) Critical current as a function of the GB angle for the 0-π-junctions.

7.2.3 Magnetic length

The magnetic length of the junction is an important measure since it will determine how the junction behaves under the influence of an external magnetic field. The Josephson penetration depth, $\lambda_J = \sqrt{\Phi_0/2\pi\mu_0 t J_c}$, gives the length scale of the penetration of the external magnetic field into the junction. If $L/\lambda_J < 2$, where L is the length of the junction, the junction is said to be magnetically short and the external field will penetrate the junction in a homogenous way. The Fraunhofer patterns presented in chapter 2 for junctions in magnetic field were derived for short junctions. With increasing length, self fields generated by the Josephson current become increasingly important and non-uniformities in the current density will modify the magnetic field dependence of I_c.

The magnetic length of the 0-junctions changes with the GB angle. For the junctions at 20º the Josephson penetration depth is in the range 2 to 3µm while at 70º it goes down to 1 µm. The explanation for this is twofold. The critical current (and hence the current density) changes with the GB angle and around 70º there is a maximum in critical current (see figure 7.4). The other contribution comes from the variation of the London penetration depth. When the GB angle increases, the screening currents generated to expel the magnetic field from the interior of the junction will, to a larger extent, be transported along the *c*-axis direction of the (103)YBCO film (see fig 7.5). The London penetration depth for the *c*-axis direction is considerably larger than the one in the *ab*-plane. Given the high critical temperature for the YBCO film (around 89K) we have

assumed the London penetration depth for current transport in c-axis direction, λ_c, to be 2 μm [41], while λ_{ab} is taken to be 130 nm. Both values, taken from literature, are considered to be reasonable for YBCO films with a critical temperature in the range of ours.

The London penetration depth for the (001) YBCO electrodes do not change with the angle since the current transport in this case is always in the *ab*-plane regardless of GB angle. For the (103) YBCO electrodes the current transport depends strongly on the GB angle. For low angles, close to the tilt-case, the current transport across the junction has a substantial component in *c*-axes direction for the (103) electrode. However, the screening currents along the GB are transported along the *ab*-planes (see figure 7.5) resulting in an effective London penetration depth close to λ_{ab}. For high GB angles the opposite is true. The current across the junction is in the *ab*-planes, while the screening currents have a considerable component in *c*-axis direction along the GB (in the (103) electrode) resulting in a London penetration depth closer to λ_c.
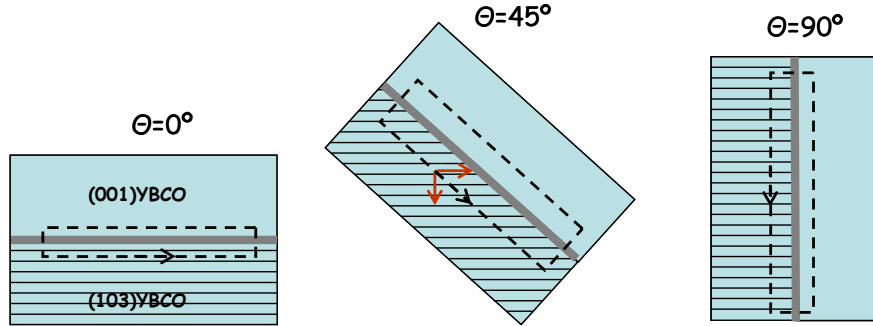
Figure 7.5:   The path of the screening currents with respect to the crystal orientation for three different GB angles. For θ=0º the screening current in the (103) electrode are mainly in the *ab*-planes, while for θ=90º the transport along the c-axis (interplane) direction plays a fundamental role.

In figure 7.6 the $I_c(B)$ pattern of junctions with a GB angle of 20º (a) and (b), and with a GB angle of 70º (c) and (d) are shown. From equation 6.3 it is found that the effective London penetration depth for θ=20º is 0.50μm and for θ= 70º is 1.33 μm. The junctions corresponding to (a) and (b) have the same θ but different λ_J. This is due to the difference in critical current. Figure 7.6 illustrates the influence of the magnetic length on the $I_c(B)$ pattern. Typical behavior for very long junctions is a $I_c(B)$ pattern with a large main peak and smaller side peaks. The $I_c(B)$ pattern of the junctions presented in figure 7.6 shows such a trend, with a more pronounced main peak, for magnetically longer junctions. All junctions measured here have a length, L, of 10μm. It should be noted that even though the values of λ_{ab} and λ_c used in the calculations are estimations taken from

literature and may differ from our experimental situation the comparison for the junctions shown in figure 7.6 are still valid.
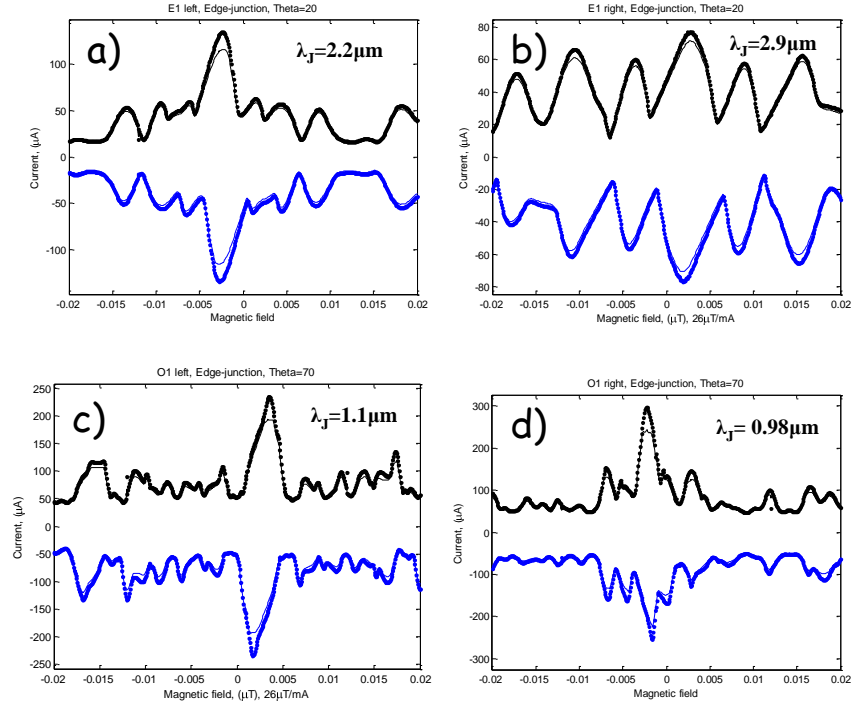
Figure 7.6:   Critical current versus applied magnetic field for (a) and (b) 0-junctions at GB angle 20º, (c) and (d) 0-junctions at GB angle 70º. The London penetration depth is a function of both the angle and the critical current. (Here the field is measured in mA current fed to the coil. 1mA corresponds to 26µT.)

7.2.4 Temperature dependence of the Josephson penetration depth

Both the London penetration depth and the critical current depend on the temperature. According to the Gorter-Casimir two fluid approximation the London penetration depth changes with the temperature as [48,49]:

$$\lambda(T) = \lambda(0)\frac{1}{\sqrt{1-\left(\dfrac{T}{T_c}\right)^n}}$$

(7.2)

Where the exponent n = 2.1-2.5. Hence the London penetration depth increases with increasing temperature and from the formula for the Josephson penetration depth in expression 2.16 it can be found that such a change in London penetration depth works in favor of a decreasing Josephson penetration depth. However, the critical current decreases rapidly with increasing temperature and gives a much larger contribution to the Josephson penetration depth. The result is an increasing Josephson penetration depth with increasing temperature and the junctions undergo a transition to a shorter limit at higher temperatures. An example is given in figure 7.7 for a 0-π-junction at a GB angle of 10º. At 8K the I_c(B) pattern is irregular with respect to the zero field. This is the result of self field effects in a junction with non-uniform current density (note that the I_c(B) pattern, even though it is irregular it is still point-symmetric. When the Josephson penetration depth increases self field effects become negligible and the I_cB pattern becomes symmetric.

Figure 7.7 shows the temperature dependent transition of a 0-π-junction with a non-uniform current distribution from the long to short regime. By using the same values for the London penetration depth as before and considering equation 7.2 to account for the influence of the temperature the estimated Josephson penetration depth changes from 4µm at 8K to 7.5µm at 70K

It is worth nothing that for the junction in figure 7.7 microfaceting causes the Ic(B) pattern to deviate from the ideal (for comparison see fig 2.7)

If magnetic flux is trapped in the junction or in the film close to the junction the I_c(B) pattern can be shifted. Under the influence of trapped flux the point symmetry is typically lost. It is therefore valuable to plot both the positive and the negative critical current as a function of magnetic field to ensure that there is no trapped flux in the devices.
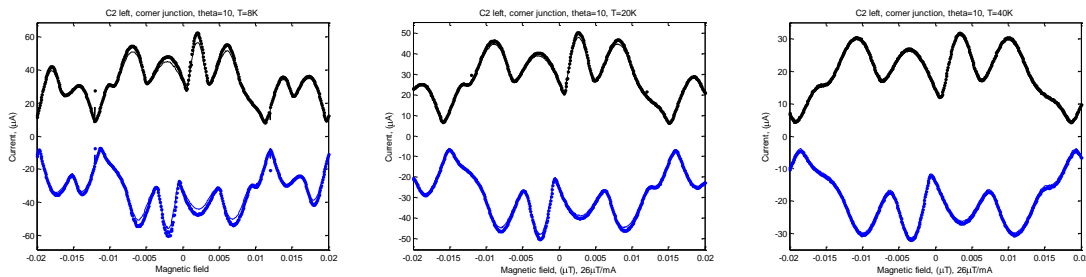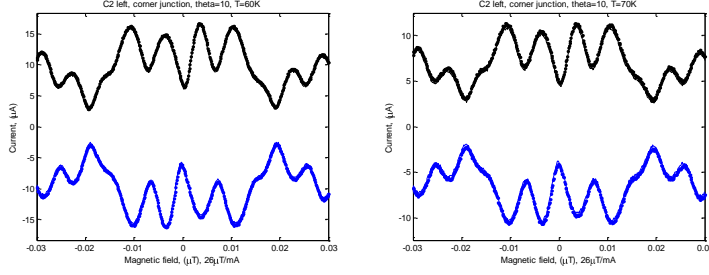
Figure 7.7: $I_c(B)$ pattern for the same junction at different temperatures. The junction changes from magnetically long to short as a function of temperature. (Here the current is measured in mA current fed to the coil. 1mA corresponds to 26μT.)

7.2.5 Modulation period

The changing London penetration depth will also influence the effective magnetic area of the junction which in turn effects the modulation period of the $I_c(B)$ pattern. The external flux through the junction area (Φ) is given by the effective junction area, A_{eff}, times the magnetic field, B. The effective magnetic area is defined as the barrier thickness plus the sum of the London penetration depth in each electrode (in GB junctions the barrier thickness is negligible. The first minimum in the Fraunhofer pattern is found when the flux through the junction area corresponds to one flux quantum. Since $\Phi_0 = B \cdot A_{eff}$ the modulation period is smaller for a junction with larger effective area. Since the effective London penetration depth increases by increasing the grain boundary angle θ we expect a monotonic reduction of the modulation period ΔB=Φ_0 going from θ=0 to θ=90. This is indeed observed in our 0-junctions. For the 0-π-junctions the angular dependence of the modulation period evolves in the opposite direction. The modulation period becomes larger for higher angles. In figure 7.9 the $I_c(B)$ pattern for 0-π-junctions at different GB angles are shown.

A possible explanation for the unconventional behavior could be related to the specific design of the samples. The electrodes for the 0-π-junctions become narrower for higher GB angle. Instead the 0-junctions keep the same width for all electrodes. In a paper by Rosenthal et al [23] the modulation period for the critical current for junctions in magnetic field is investigated. In their experiments a dependence of ΔB on 1/w² instead of the usual 1/w was found due to flux focusing effects.

The relation between the modulation period and the width of the junction is given by:

$$\Delta B \approx \Phi_0 \frac{1.84}{w_2} \tag{7.3}$$

where w is the width of the junction. The relation is valid for very thin films where the phase difference across the width becomes independent of thickness [23].

In our 0-π-junctions the width of the electrodes becomes narrower with GB angle for the even though the junction width is the same. Using a similar approach as [1] but using the width of the electrodes instead of the width of the junctions a very good agreement between the experimental data and the theoretical dependence of the modulation period given in equation 7.3. In figure 7.8 the modulation period as a function of GB angle is shown for 0-π-junctions together with the theoretical predictions according to equation 7.3.
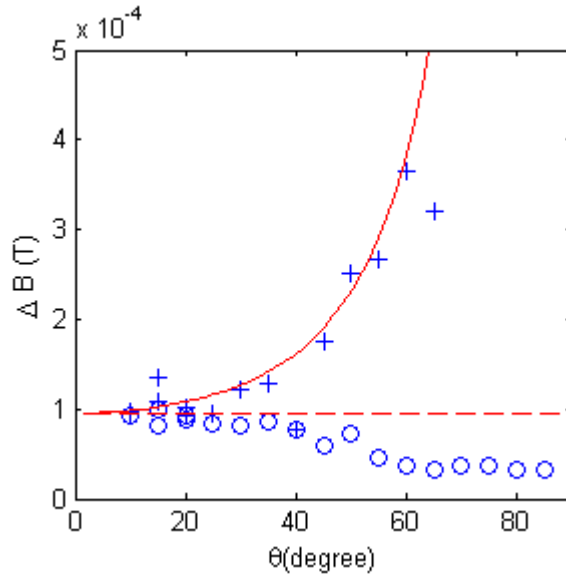
Figure 7.8:   Modulation period as a function of GB angle. The crosses correspond to the 0-π-junctions and the circles to the 0-junctions. The red lines correspond to the theoretical predictions according to equation 7.3 for 0-π (solid) and 0 (dashed) junctions respective. The 0-π-junctions follow the theoretical model well, while for the 0-junctions the effect from the larger effective area influences the modulation period.
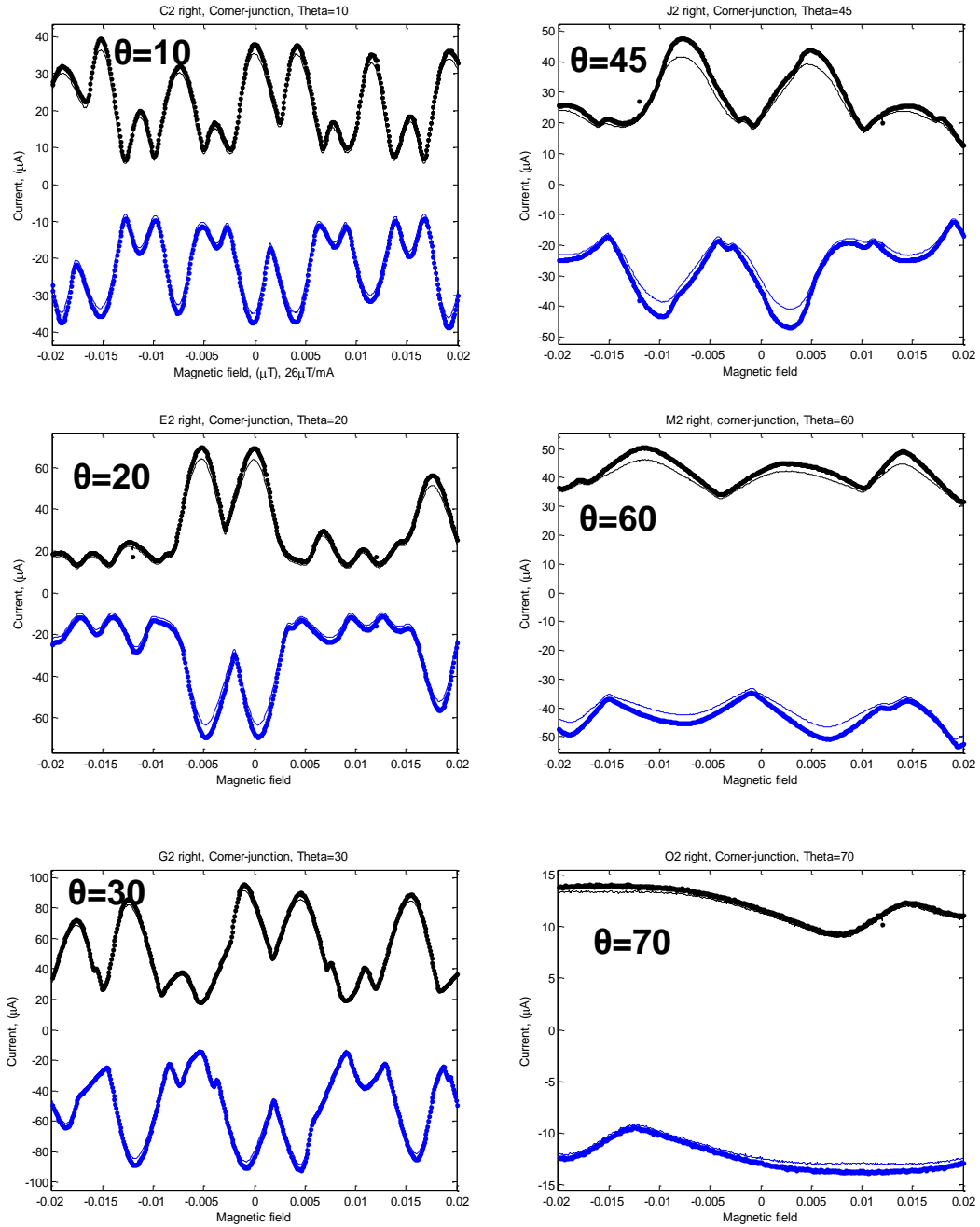
Figure 7.9: $I_c(B)$ pattern for 0-π-junctions with different GB angles. Due to the design of the junctions the width of the electrodes are proportional to cos θ. (Here the current is measured in mA current fed to the coil. 1mA corresponds to 26μT.)

Semifluxon dynamics in 0-π-Junctions

Josephson junctions with a π phase discontinuity along the barrier may have a ground state where spontaneous flux is generated at the discontinuity point. As described in chapter 2 this flux is quantized corresponding to a half flux quantum (semifluxon). It is due to spontaneous currents originated to compensate the π discontinuity.

In this chapter we have focused on the feasibility of the biepitaxial technique to study the static and dynamics properties of a semifluxon in corner like junctions. As we have discussed in chapter 7 the transport properties of biepitaxial grain boundaries are strongly affected by the presence (unavoidable) of faceting at submicron and nanometer scale. The existence of 0-π facets along the grain boundary line modifies the otherwise net step-like profile of the phase along the interface. It is therefore an issue to establish if in such conditions the spontaneous nucleation of a semifluxon still occurs at the corner of a nominal 0-π GB Josephson junction.

This chapter deals with the first combined study of static and dynamic properties of semifluxons in all-$YBa_2Cu_3O_{7-\delta}$ HTS grain boundary junctions. We have fabricated corner 0-π-junctions by the biepitaxial technique and imaged them with Scanning Superconductive Quantum Interference Device Microscope (SSM). For these junctions, in Chapter 7 we have discussed in detail, the response of the maximum critical current as a function of an external magnetic field. Here we will address the dynamics of the junctions. This study is the first which allows to correlate in an unambiguously way the new features of the dynamics of 0-π-junctions with the presence of a semifluxon (visualized by SSM) at the discontinuity point.

8.1 Investigation by Scanning SQUID Microscope

To investigate whether spontaneous flux is present in the 0-π-junctions we have used a Scanning SQUID Microscope (SSM) which is a powerful technique to visualize the distribution of magnetic flux along the surface of a superconductor. Both reference "0" and "0-π" junctions have been investigated.

The SSM operates in a magnetically screened environment. The sample and the scanning SQUID itself is immersed in liquid helium. A small pickup loop, made by Focused Ion Beam etching [50] is directly coupled to the SQUID. The magnetic flux ϕ_{loop} threading the pickup loop is converted by the SQUID into a voltage signal V_{out}. In order to calibrate the transfer function $dV_{out}/d\phi_{loop}$ we scanned an Abrikosov vortex in the (001) YBCO film. Since the Abrikosov vortex contains exactly one flux quantum ϕ_0 we could determine the transfer function $dV_{out}/d\phi_{loop}$. Furthermore one can extract both the size of the pickup loop and the distance between the pickup loop and the sample surface. In our case the distance between sample was found to be 1.4 μm and the size was 4.8 x 4.8 (μm)^2 A more detail report on how this is done can be found in [51].

Indeed the SSM analysis shows that spontaneous flux is present in some of the corner junctions. The junctions where spontaneous flux was detected had GB angles between 15º-35º. Due to low resolution of the measurements at lower angles we can't rule out that semifluxons exist also there. For angles >35º no spontaneous flux was detected. This could be due to the geometry with narrower electrodes for the high-angle 0-π-junctions (see chapter 7). All semifluxons were found in 0-π-junctions while the reference 0-junctions didn't show any similar signals. The I$_c$(B) characteristics for the junctions with detected semifluxons show a clear 0-π-behaviour with a minimum in critical current at zero magnetic field. Here it is interesting to note that the only reference 0-junction that had spontaneous flux generated in the grain boundary also showed a typical 0-π pattern from the I$_c$(B) measurements. Figure 8.1 shows a SSM image of a 0-π-junction with GB angle $\theta = 20^0$ with spontaneous flux generated in the GB. The dashed lines are a guide for the eye and outline where the edges of the electrode are supposed to be. Due to a mechanical drift in the system the electrode appears to be bent. Figure 8.2 shows a close up of the junction region from two different cool down occasions. One can clearly see that for both cool downs the semifluxon is present. The only difference is the topology of the measured signal. This can be attributed to the interaction of the pickup loop with the semifluxon, which causes random flips of the semifluxon polarization during each single line scan.

For the particular junction from which the SSM images in figure 8.1 have been taken the calculated Josephson penetration depth is 3μm at a temperatute T= 4.2K. This value has been obtained from equation 2.6 using jc=4.4x10^7 A/m^2 and assuming: a) that the London penetration depth is 2μm in the *c*-axis direction and 150nm in the *ab*-planes, which is

consistent with a critical temperature of around 89 K for the YBCO film and b) by considering that for a GB angle of 20° degrees the effective London penetration depth in the [103] film is 500nm due to the relation given in equation 6.3. This results in a normalized junction length $L/\lambda_J = 3.3$. The junction can be regarded to be in an intermediate regime between long and short at T=4.2 K. This is consistent with the fact that the junction shows a minimum at zero magnetic field in the $I_c(B)$ pattern. If the junction had been very long $L/\lambda_J \gg 1$ the minimum in the $I_c(B)$ pattern would have been lost [19].
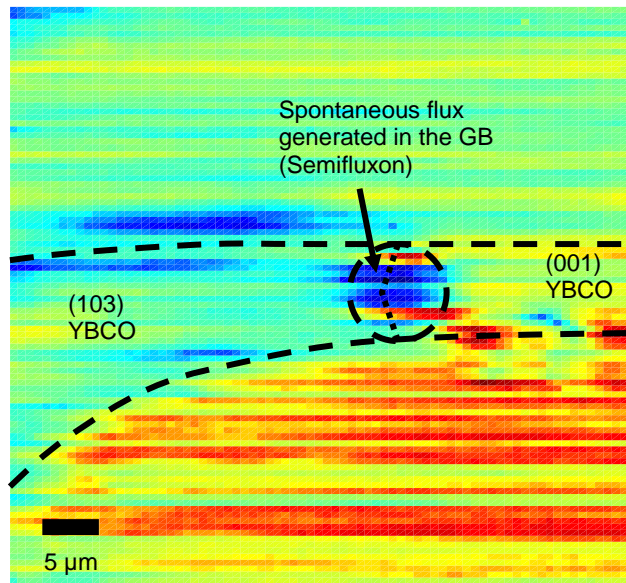
Figure 8.1:   SSM image of a YBCO 0-δ-junction with GB angle $\theta = 20^0$ taken at T= 4.2 K. The dashed line represents the boundary of the electrodes. The dotted line indicates the GB and the circle highlights the magnetic flux signal of the semifluxon.
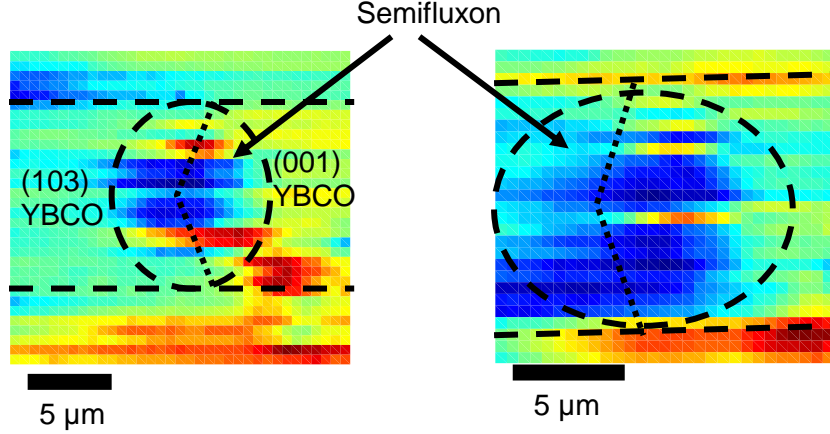
Figure 8.2:   SSM images of a YBCO 0-π-junction with GB angle $\theta = 20^0$ taken at T= 4.2 K. The two images of the same 0-π-junction have been taken during two different cool downs of the sample. The dotted line indicates the GB and the circle highlights the magnetic flux signal of the semifluxon.

To model the predicted signal from a semifluxon the static Sine-Gordon equation is solved numerically for the GB in order to calculate the spontaneous flux that is generated. The Sine-Gordon equation is a differential equation for the time dependent local phase difference $\varphi(x,t)$ in a long Josephson junction and can be written as:

$$\frac{\partial^2}{\partial t^2}\varphi(x,t) - \frac{\partial^2}{\partial x^2}\varphi(x,t) + \alpha\frac{\partial}{\partial t}\varphi(x,t) + \varepsilon(x)\sin\varphi(x,t) = \gamma \tag{8.1}$$

with boundary conditions given in terms of the normalized magnetic field η:

$$\varphi(0,t) = \varphi(t) = \eta \tag{8.2}$$

Here the time t is normalized to the plasma frequency $\omega_P = \sqrt{2\pi I_0/C\phi_0}$, with I_0 the critical current, C the capacitance of the junction and ϕ_0 the superconducting flux quantum. The space is normalized to the Josephson penetration depth λ_J, and $l = L/\lambda_J$ is the normalized length of the junction. The normalized magnetic field is given by $\eta = (2\pi\mu_0\lambda_L\lambda_J/\phi_0)B$, with λ_L the London penetration depth. The normalized conductance is give by $\alpha = 1/Q = 1/\omega_P RC$. The coefficient $\varepsilon(x)$ is related to the critical current density distribution along the GB. It is positive for 0-facets and negative for pi-facets.

In order to calculate the static magnetic flux in a 0-π-junction we set all time derivatives in equation 8.1 zero. The numerically determined magnetic flux is then considered at a distance of 1.4µm from the sample surface and integrated over the calculated SQUID

pickup loop area to get the predicted signal that should be picked up by the SSM. We found that the expected signal, $\Phi/\Phi_0 = 0.1$ from an ideal 0-π-junction is much higher than the signal we have measured experimentally $\Phi/\Phi_0 = 0.03$. We can attribute this effect to the micro faceting along the grain boundary. An AFM picture of a 0-π-junction is shown in figure 8.3. One can clearly identify the micro facets along the GB line. The micro facets influence the spontaneous flux that is generated in two ways. First, if the GB angle for the micro facet deviates enough from the nominal value, the sign of the critical current density may change. Consequently there will be a reduction in the total phase change along the whole junction length. This result in a decreased value of the spontaneous magnetic flux generated compared to the case of an ideal 0-π-junction without micro facets. The other effect is the non-uniformity of the absolute value of the critical current density that is induced also by a random distribution of micro facets along the GB line of the junction. Since the critical current across the junction is dependent on the GB angle according to equation 7.1 all micro facets will contribute to a more non-uniform critical current distribution resulting in a decreased absolute value of the spontaneously generated magnetic flux. By making an estimation of the facets lengths, GB angles and relative phase for the facets from AFM images we can prove by solving the Sine-Gordon equation that the micro faceting can explain the reduction of the magnetic flux value we observe in the measured signal compared to the expected signal from an ideal 0-π-junction. Here we want to point out that from the AFM images we can determine the sign of the critical current density for each micro facet. Unfortunately we can not determine unambiguously the critical current density, which makes an exact calculation of the expected magnetic flux signal impossible.
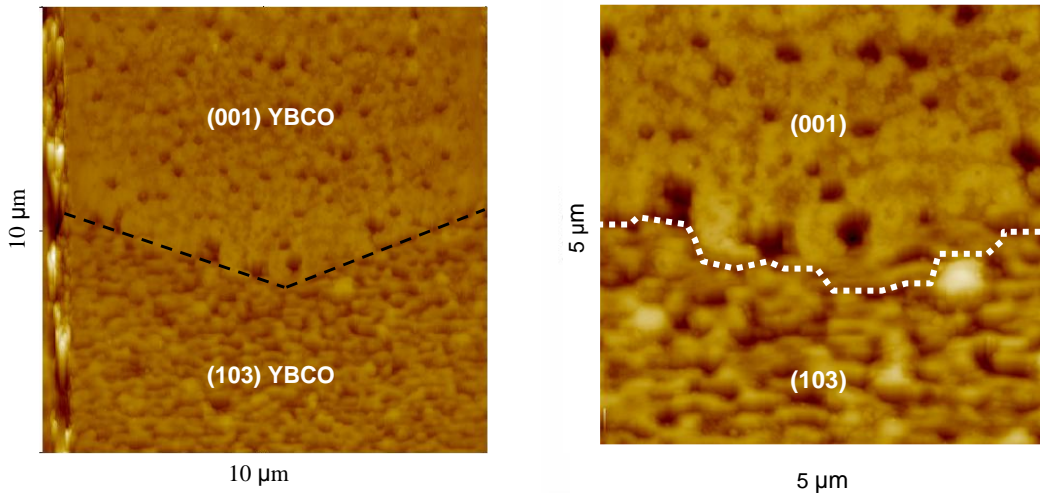
Figure 8.3:   AFM micrograph of the junction. The nominal GB is marked by the dotted line. The true GB consists of a large number of microfacets, which is indicated by dotted line in the right panel.

8.2 Measurements of resonances in the IV characteristics

8.2.1 Zero Field Steps

The phase dynamics of a Josephson junction at finite bias voltages reflects itself as distinct features in the current voltage characteristic (IVC). We first discuss the signatures in the IVC of two types of phase dynamics which can occur in standard 0-junctions. Thereafter we will describe the effect of a semifluxon in a 0-π-junction on the phase dynamics and accordingly on the IVC.

0-junction in the short limit $L/\lambda_J < 1$:

For a finite external applied magnetic field current steps at certain bias voltages appear in the IVC. These steps, also called Fiske steps, result form the junction acting as a transmission line. In an external magnetic field, when the Josephson frequency matches the frequencies of the electromagnetic cavity modes the current across the junction is enhanced, this happens at voltage values according to:

$$V_n^F = \frac{n\Phi_0 \bar{c}}{2L} \tag{8.3}$$

Where L is the length of the junction, $\bar{c}$ is the Swihart velocity and Φ_0 the flux quantum and n is an integer, which determines the number of wave length of the standing electromagnetic wave. The Swihart velocity is given by $\bar{c} = c_0 \sqrt{t_d / \varepsilon_r d}$, where c_0 is the vacuum speed of light, t_d is the thickness of the tunneling barrier at the GB, ε_r is the relative permittivity of the tunneling barrier, and $d = t_d + 2\lambda_L$ is the magnetic thickness of the junction. Here it is important to note that Fiske resonances appear only at a finite externally applied magnetic field.

0-junction in the long limit $L/\lambda_J > 1$:

At finite external applied magnetic field also here one observes Fiske resonances in the IVC. In this case a moving Josephson vortex chain synchronizes with the standing electromagnetic waves along the junction length. Contrary to the short junction limit one can detect current steps in the IVC of a long Josephson junction also for zero applied magnetic field. These steps, which are called zero field steps (ZFS), have a different underlying phase dynamics.

ZFSs are the result of fluxons traveling along the junction. If the junction is considered to work as an open ended transmission line a fluxon that reaches one end will be reflected and travel back as an antifluxon. A fluxon coming from one side, traveling along the whole length of the junction where it is reflected and travels back as an antifluxon makes once cycle during the time, $\Delta t = \frac{2L}{\bar{c}}$. The total transferred magnetic flux during one period corresponds to $2\Phi_0$. The ZFS will consequently occur at voltages:

$$V_n^{ZFS} = \frac{\Delta\Phi}{\Delta t} = n \cdot \frac{\Phi_0 \bar{c}}{L},$$ (8.4)

where the integer n corresponds to the number of fluxons moving in the Josephson junction. The voltage spacing of the ZFSs is twice larger than for Fiske steps.

In the following we consider the phase dynamics for the case of a junction with a 0-π discontinuity.

0-π-junction in the short limit $L/\lambda_J < 1$:

Also here at finite bias voltages all current steps in the IVC are caused by Fiske resonances. For finite magnetic field the current steps appear at the same voltages as for the 0-junction (see equation 8.3). In contrast to the 0-junction case Fiske steps are now also observable at zero externally applied magnetic field [52]. Calculations by Nappi et al. [52]) show that at zero magnetic field current steps appear on the IVC only for odd values of n while at finite magnetic field current steps appear at all values of n.

0-pi-junction in the long limit $L/\lambda_J > 1$:

In the case of a long 0-π-junction the first ZFS appears at exactly half of the standard 0-junction ZFS voltage spacing, which corresponds to the same voltage as the first Fiske step. The first current step is caused by the flipping of the semifluxon. During one period $\Delta t = 2L/\bar{c}$ the semifluxon flips twice causing a change of $1\Phi_0$. The next ZFS step happens at $n = 3/2$ using equation 8.4. Here the total flux change during on period is $3\Phi_0$, where $1\Phi_0$ is caused by the flipping of the semifluxon and $2\Phi_0$ are generated by a fluxon/antifluxon moving back and forth in the junction. The following step would occur for $n = 5/2$ involving the flipping of the semifluxon and the moving of two fluxons in the junction. Therefore such current steps are also called half-integer ZFSs.

8.2.2 Measurements

A typical current voltage characteristic of a biepitaxial YBCO 0-junction, with GB angle $\theta = 20^0$, measured at 4.2 K and zero externally applied magnetic field is shown in figure 8.4. From the IVC measurement data of the same junction recorded at various magnetic fields we plot in figure 8.5 the current through the junction as a function of magnetic field for various fixed bias voltages (voltage contours). The first Fiske step appears at V≈0.5 mV. The first ZFS should hence be found at twice that voltage, around V=1 mV. From the voltage contours plotted in figure 8.5 a resonance step is indeed found at that voltage but at a small finite field. In order to understand the occurrence of the ZFS at a finite magnetic field we numerically solved equation 8.1 considering some asymmetry in the bias current density distribution. From such simulations we can determine the voltage contours, which are presented in figure 8.6. One can clearly see that ZFSs occur at finite magnetic field for long junctions with some asymmetry in the bias current distribution where self fields are generated by the junction itself. The ZFS is supposed to be found where the external magnetic field exactly cancels out the intrinsically generated one.
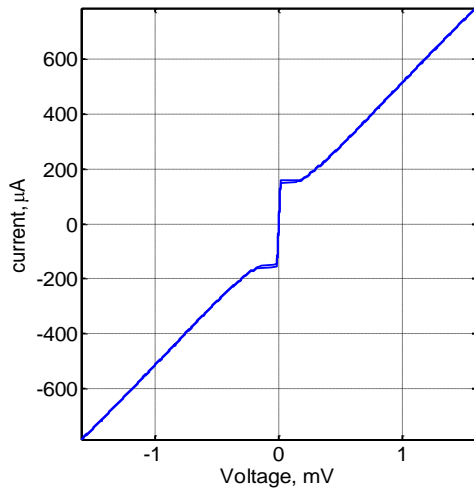
Figure 8.4   Current voltage characteristic of a biepitaxial 0-junction measures at 4.2 K and zero externally applied magnetic field. The GB angle of the junction is 20^0
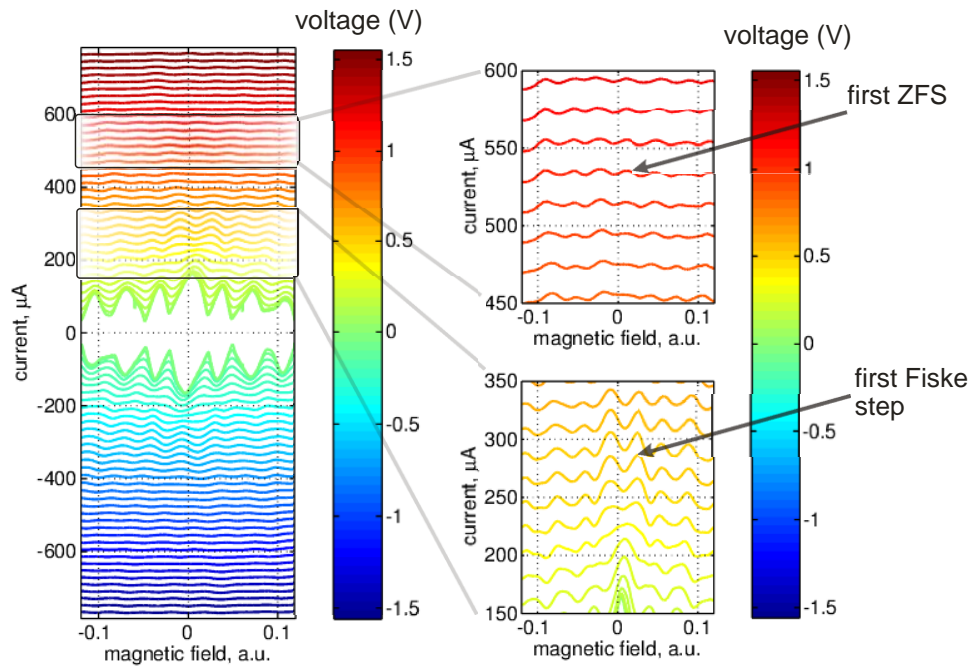
Figure 8.5:   Voltage contours extracted from measured current voltage characteristics of a 0-junction at various magnetic fields and T = 4.2 K. The GB angle of the junction is 20^0

101
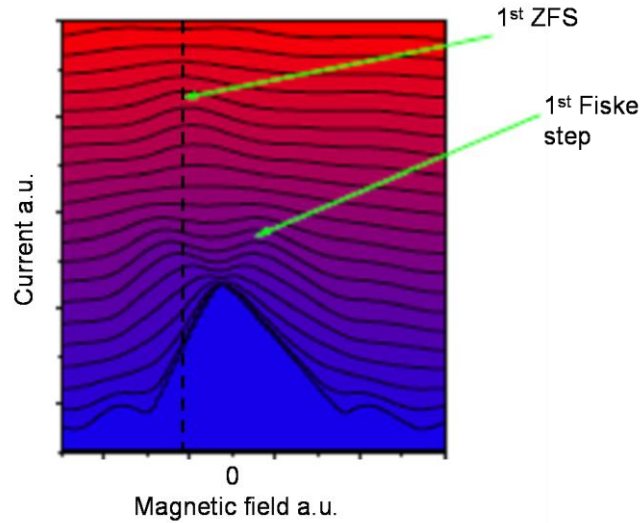
Figure 8.6:   Voltage contours of simulated current voltage characteristics of a 0-π-junction for various externally applied magnetic fields. The dissipation parameter is 0.75, the normalized length is 5 and the asymmetry of the bias current density is 15%.

For the 0-π-junction, where we show the measured voltage contours in figure 8.7, the identification of the different current steps in the IVCs is slightly more complicated. Nappi et al [52] have theoretically shown that it is possible to have Fiske resonances at zero magnetic field for a short junction with a single 0-π discontinuity. It can therefore be difficult to distinguish between a Fiske step in a short 0-π-junction and a semi-integer ZFS in an intermediate 0-pi-junction. However the $I_c(B)$ pattern is slightly tilted, showing that the junction is in the long regime (or rather intermediate). This is strengthened by the fact that the estimated Josephson penetration depth is around 3 microns while the junction length is 10 microns. Together with the SSM images that shows that the semifluxon is present at the phase discontinuity we have very strong indications that the resonance found in figure 8.7 is indeed a semi-integer ZFS. Also for this case we simulated the voltage contours as a function of external magnetic field of a 0-π-junction having a slight asymmetry in the bias current density, which are shown in figure 8.8. One can clearly identify the first half integer zero field step emerging at a small finite magnetic field. Here the finite external magnetic field is compensated by the self field effect of the junction, similar to the case of the 0-junction.
In the following section we will discuss the phase dynamics in our 0- and 0-π-junctions causing integer ZFSs and half-integer ZFSs in the IVCs, respectively.
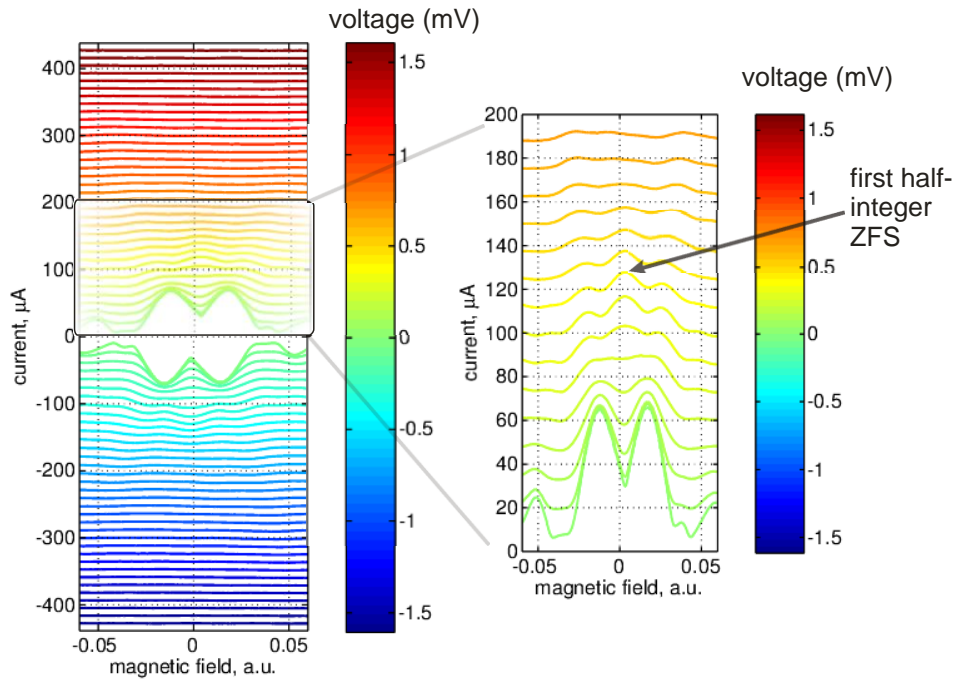
Figure 8.7: Voltage contours of measured current voltage characteristics of a 0-π-junction at various magnetic fields and T = 4.2 K. The GB angle of the junction is 20^0
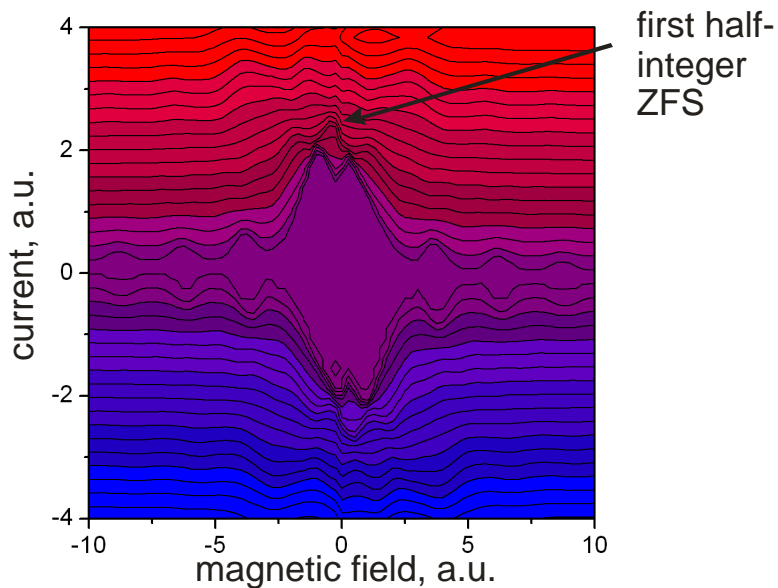
Figure 8.8: Voltage contours of simulated current voltage characteristics of a 0-π-junction for various externally applied magnetic fields. The dissipation

parmeter α is 0.75, the normalized length is 5 and the asymmetry of the junction is 15%.

8.2.3 Dynamics

To simulate the dynamics of the junction, i.e. the distribution of the field and phase over time we have to estimate the dissipation of the junction since it is a parameter that strongly influences the phase dynamics. If we consider the first Fiske step of the 0-junction at V=0.5mV (see figure 8.5), and a thickness of the film around 1600Å the resulting capacitance for the junction is 65fF using equation 8.3. The quality factor of the junction is given by $Q = \omega_p RC$ where R is the normal resistance, C the capacitance and ω_p is the plasma frequency and is given by: $\omega_p = 1/\sqrt{L_J C}$, where L_J is the Josephson inductance. For the junction in question the critical current at 4.2K is 85 μA and the normal resistance 5Ω and hence for the quality factor we get $Q = 0.65$. With such a low quality factor the dissipation α is high: $\alpha = 1/Q = 1.5$. If instead the small hysteresis that is present is considered the dissipation α will be nearly one. Not only does the dissipation differ depending on how it is calculated, it is also too large for any steps to be visible according to simulations. However, in our junctions the steps are indeed weak, but still visible. Therefore in the simulations we adjusted the dissipation parameter α, in order to reproduce the experimental IVCs. Using this approach we get for both the 0-junction and the 0-π-junction considered here a dissipation parameter $\alpha \sim 0.75$. Using this value of dissipation we simulated the phase dynamics for a 0- and a 0-π-junction including a slight asymmetry in the bias current density distribution.

In Fig. 8.9 (left panel) we show the dynamics of the local magnetic field (local derivative of phase) in the 0-junction at the first ZFS (see figure 8.6). During one period a fluxon and an antifluxon enter the junction from opposite sides and annihilate at the center of the junction. The asymmetry of the junction causes that the two fluxons propagate only to the center of the junction, instead of moving along the whole length of the junction. The total flux change during one period $\Delta t = L/\overline{c}$ is $1\Phi_0$ resulting in a voltage position of the current step corresponding to the first ZFS (see equation 8.4). The simulated dynamics of the magnetic field in a 0-π-junction at the first half integer ZFS (see figure 8.8) is shown in the right panel of Fig. 8.9. Also in this case we used an asymmetry in the critical current distribution in order to obtain a ZFS at a finite external magnetic field. During one half period $\Delta t = L/\overline{c}$ a fluxon enters the junction and flips the semifluxon in the center. During the next half period an antifluxon enters the junction from the other side, moves to the center and flips the semifluxon again. During the full period $\Delta t = 2L/\overline{c}$ we obtain a flux change of $1\Phi_0$. This corresponds to the voltage position of the first half integer ZFS ($n = 1/2$). The simulations clearly show that the zero field steps observed in our 0- and 0-π-junction are dominated by the dynamics of fluxons, representative for integer ZFS in 0-junctions, and the interaction of fluxons with semifluxons, which is typical for the dynamics of half integer ZFS in 0-π-junctions.
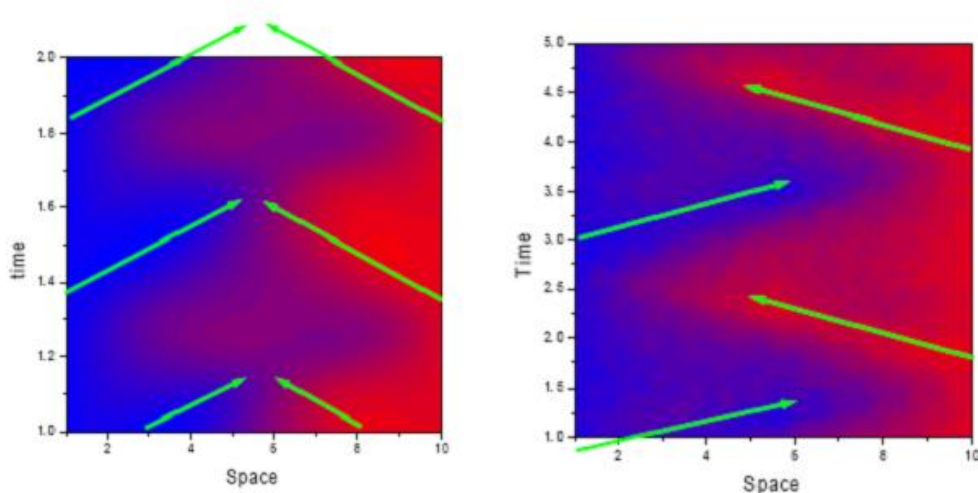
Figure 8.9:   Local magnetic flux in a 0-junction (left) and 0-π-junction (right) as a function of time and position along the length of the junction. The blue color corresponds to a fluxon and the red color corresponds to an antifluxon. The green arrows indicate the propagation of the fluxons.

8.2.4 Conclusions

We detected semifluxons in 0-π YBCO Josephson junctions by using a scanning SQUID microscope. Moreover we observed half integer zero field steps in the IVCs of this junctions, which are a signature of the semifluxon dynamics. In control junctions which consisted only of one 0-facet neither of those signatures (semifluxon and half integer ZFS) were observable. This fact clearly proves that the biepitaxial technique is suitable for the fabrication of well defined 0-π-junctions. Such junctions are very attractive for novel applications in information storage and processing both in classical and quantum regime. From our measurements we can further conclude that the meandering of the biepitaxial GB line is small enough (for GB angles 15^0-35^0) to ensure the spontaneous generation of a semifluxon in a nominal 0-π-Josephson junction.

Acknowledgements

There are many people that have been important during the four years I have worked with this thesis. My supervisor Floriana Lombardi has been a great source of inspiration. I admire your enthusiasm and all the time you put into all your students work. Your never-ending support in all situations has been fantastic. My supervisor Francesco Tafuri for the best possible support for my work in Naples. Your optimism and positive approach to everything you do is something to learn from. A special thanks to Thilo Bauch for your incredible patience with any kind of question I have had and for all your help throughout my time as a PhD student. Your knowledge in the field is impressive and I have appreciated to work with you. Daniela Stornaiuolo for making my time in Naples so much easier. I'm happy we both ended up in the same group! Guido Celentano who has been a great help for me in Naples. Without you everything would have been much more complicated for me as a foreign student in Italy. Ann-Marie Frykestig for the same support in Sweden. Tord Claesson for creating such a nice environment to work in and for always having time to stop by and give a little bit of advice or just some nice words.

It's impossible to name everybody who I would like to acknowledge here. So many of my colleagues and friends in Gothenburg and in Naples have contributed to making my years as a PhD student fun and rewarding. Thank you all!

Bibliography

[1]   E. Goldobin, D. Koelle, and R. Kleiner, "Ground states of one and two fractional vortices in long Josephson 0-kappa junctions," *Physical Review B (Condensed Matter and Materials Physics)*, vol. 70, Nov. 2004, pp. 174519-9.

[2]   E. Goldobin et al., "Dynamics of semifluxons in Nb long Josephson 0-pi junctions," *cond-mat/0311610*, Nov. 2003; http://arxiv.org/abs/cond-mat/0311610.

[3]   T. Gaber et al., "Nonideal artificial phase discontinuity in long Josephson 0-kappa junctions," *Physical Review B (Condensed Matter and Materials Physics)*, vol. 72, 2005, pp. 054522-8.

[4]   T. Gaber et al., "Nonideal artificial phase discontinuity in long Josephson 0-kappa junctions," *Physical Review B (Condensed Matter and Materials Physics)*, vol. 72, 2005, pp. 054522-8.

[5]   E. Goldobin et al., "Oscillatory eigenmodes and stability of one and two arbitrary fractional vortices in long Josephson 0-kappa junctions," *Physical Review B (Condensed Matter and Materials Physics)*, vol. 71, Mar. 2005, pp. 104518-8.

[6]   J. Waldram, *Superconductivity of Metals and Cuprates*, Taylor & Francis, 1996.

[7]   T.V. Duzer and C.W. Turner, *Principles of Superconductive Devices and Circuits*, Prentice Hall PTR, 1998.

[8]   M. Tinkham, *Introduction to Superconductivity: Second Edition*, Dover Publications, 2004.

[9]   T. Kontos et al., "Josephson Junction through a Thin Ferromagnetic Layer: Negative Coupling," *Physical Review Letters*, vol. 89, 2002, p. 137007.

[10]   V.V. Ryazanov et al., "Coupling of Two Superconductors through a Ferromagnet: Evidence for a pi Junction," *Physical Review Letters*, vol. 86, Mar. 2001, p. 2427.

[11]   W. Guichard et al., "Phase Sensitive Experiments in Ferromagnetic-Based Josephson Junctions," *Physical Review Letters*, vol. 90, Apr. 2003, p. 167001.

[12]   E. Il'ichev et al., "Degenerate Ground State in a Mesoscopic YBa2Cu3O7-x Grain Boundary Josephson Junction," *Physical Review Letters*, vol. 86, Jun. 2001, p. 5369.

[13] S. Yip, O.F. De Alcantara Bonfim, and P. Kumar, "Supercurrent tunneling between conventional and unconventional superconductors: A Ginzburg-Landau approach," *Physical Review B*, vol. 41, Jun. 1990, p. 11214.

[14] S. Yip, "Josephson current-phase relationships with unconventional superconductors," *Physical Review B*, vol. 52, 1995, p. 3087.

[15] E. Goldobin et al., "Josephson junctions with second harmonic in the current-phase relation: Properties of phi junctions," *Physical Review B (Condensed Matter and Materials Physics)*, vol. 76, Dec. 2007, pp. 224523-13.

[16] A. Barone and G. Paterno, *Physics and Applications of the Josephson Effect*, John Wiley & Sons Inc, 1982.

[17] V. Schmidt, *The Physics of Superconductors: Introduction to Fundamentals and Applications*, Springer, 2002.

[18] D. Van Harlingen, "Phase-sensitive tests of the symmetry of the pairing state in the high-temperature superconductors-Evidence for d(x2-y2) symmetry," *Reviews of Modern Physics*, vol. 67, Apr. 1995, pp. 515-35.

[19] J.R. Kirtley, K.A. Moler, and D.J. Scalapino, "Spontaneous flux and magnetic-interference patterns in 0- pi Josephson junctions," *Physical Review B*, vol. 56, Jul. 1997, p. 886.

[20] E. Goldobin, D. Koelle, and R. Kleiner, "Semi-fluxons in long Josephson 0-pi-junctions," *cond-mat/0207742*, Jul. 2002; http://arxiv.org/abs/cond-mat/0207742.

[21] C.C. Tsuei and J.R. Kirtley, "Pairing symmetry in cuprate superconductors," *Reviews of Modern Physics*, vol. 72, Oct. 2000, p. 969.

[22] M. Sigrist and T.M. Rice, "Unusual paramagnetic phenomena in granular high-temperature superconductors—A consequence of d- wave pairing?," *Reviews of Modern Physics*, vol. 67, Apr. 1995, p. 503.

[23] P. Rosenthal et al., "Flux focusing effects in planar thin-film grain-boundary Josephson junctions," *Applied Physics Letters*, vol. 59, Dec. 1991, pp. 3482-4.

[24] R. Humphreys and J. Edwards, "YBa2Cu3O7 thin film grain boundary junctions in a perpendicular magnetic field," *Physica C: Superconductivity*, vol. 210, May. 1993, pp. 42-54.

[25] V.G. Kogan et al., "Josephson junction in a thin film," *Physical Review B*, vol. 63, Mar. 2001, p. 144501.

[26] E.H. Brandt and G.P. Mikitik, "Meissner-London Currents in Superconductors with Rectangular Cross Section," *Physical Review Letters*, vol. 85, Nov. 2000, p. 4164.

[27] J. Gao et al., "Controlled preparation of all high-Tc SNS-type edge junctions and DC SQUIDs," *Physica C: Superconductivity*, vol. 171, Oct. 1990, pp. 126-130.

[28] F. Tafuri et al., "Microstructure and Josephson phenomenology in 45° tilt and twist YBa2Cu3O7- delta artificial grain boundaries," *Physical Review B*, vol. 59, May. 1999, p. 11523.

[29] F. Tafuri et al., "Feasibility of biepitaxial YBa2Cu3O7-x Josephson junctions for fundamental studies and potential circuit implementation," *Physical Review B*, vol. 62, Dec. 2000, p. 14431.

[30] R.R. Schulz et al., "Design and realization of an all d-wave dc pi-superconducting quantum interference device," *Applied Physics Letters*, vol. 76, Feb. 2000, pp. 912-914.

[31] B. Chesca et al., "d-Wave Induced Zero-Field Resonances in dc pi - Superconducting Quantum Interference Devices," *Physical Review Letters*, vol. 88, Apr. 2002, p. 177003.

[32] C. Jia et al., "Microstructure of epitaxial YBa2Cu3O7 films on step-edge SrTiO3 substrates," *Physica C: Superconductivity*, vol. 175, May. 1991, pp. 545-554.

[33] C. Jia et al., "The microstructure of epitaxial YBa2Cu3O7 films on steep steps in LaAlO3 substrates," *Physica C: Superconductivity*, vol. 196, Jun. 1992, pp. 211-226.

[34] F. Miletto Granozio et al., "Structure and properties of a class of CeO2-based biepitaxial YBa2Cu3O7- delta Josephson junctions," *Physical Review B*, vol. 67, May. 2003, p. 184506.

[35] T. Bauch et al., "Quantum Dynamics of a d-Wave Josephson Junction," *Science*, vol. 311, Jan. 2006, pp. 57-60.

[36] F. Lombardi et al., "Dynamics of a LC Shunted YBa2Cu3O7-δ Josephson Junction," *Applied Superconductivity, IEEE Transactions on*, vol. 17, 2007, pp. 653-658.

[37] B.H. Moeckly and R.A. Buhrman, "Josephson properties of basal-plane-faced tilt boundaries in YBa[sub 2]Cu[sub 3]O[sub 7 - delta] thin films," *Applied Physics Letters*, vol. 65, Dec. 1994, pp. 3126-3128.

[38] T. Bauch et al., "Dynamics of d-wave YBa2Cu3O7−x dc SQUIDs," *Superconductor Science and Technology*, vol. 20, 2007, pp. S98-S104.

[39] D.N. Zheng et al., "Magnetic susceptibilities, critical fields, and critical currents of Co- and Zn-doped YBa2Cu3O7," *Physical Review B*, vol. 49, Jan. 1994, p. 1417.

[40] A. Porch et al., "Temperature dependent magnetic penetration depth of Co and Zn doped YBa2Cu3O7 obtained from the AC susceptibility of magnetically aligned powders," *Physica C: Superconductivity*, vol. 214, Sep. 1993, pp. 350-358.

[41] C.C. Homes et al., "Coherence, incoherence, and scaling along the c axis of YBa[sub 2]Cu[sub 3]O[sub 6 + x]," *Physical Review B (Condensed Matter and Materials Physics)*, vol. 71, May. 2005, pp. 184515-5.

[42] J. Lee et al., "Penetration depth in oxygen depleted YBCO thin films," *Synthetic Metals*, vol. 71, Apr. 1995, pp. 1605-1606.

[43] V.G. Kogan and V.L. Pokrovsky, "Current in Narrow Channels of Anisotropic Superconductors," *Physical Review Letters*, vol. 90, Feb. 2003, p. 067004.

[44] M.M.K. Jr, "Extraction of inductances of plane thin film superconducting circuits," *Superconductor Science and Technology*, vol. 10, 1997, pp. 389-394.

[45] E. Terzioglu and M. Beasley, "Complementary Josephson junction devices and circuits: a possible new approach to superconducting electronics," *Applied Superconductivity, IEEE Transactions on*, vol. 8, 1998, pp. 48-53.

[46] T. Ortlepp et al., "Flip-Flopping Fractional Flux Quanta," *Science*, vol. 312, Jun. 2006, pp. 1495-1497.

[47] F. Lombardi et al., "Intrinsic d-Wave Effects in YBa2Cu3O7- delta Grain Boundary Josephson Junctions," *Physical Review Letters*, vol. 89, Oct. 2002, p. 207001.

[48] A. Hosseini et al., "ccirc-Axis Electrodynamics of YBa2Cu3O7- delta ," *Physical Review Letters*, vol. 81, 1998, p. 1298.

[49] A. Hosseini et al., "Survival of the d-Wave Superconducting State near the Edge of Antiferromagnetism in the Cuprate Phase Diagram," *Physical Review Letters*, vol. 93, 2004, p. 107003.

[50] *. Aico G. P. Troeman et al., "NanoSQUIDs Based on Niobium Constrictions," Jun. 2007;
http://pubs.acs.org/doi/abs/10.1021/nl070870f?prevSearch=nano+SQUIDS&search HistoryKey=.

[51] J.R. Kirtley et al., "High-resolution scanning SQUID microscope," *Applied Physics Letters*, vol. 66, Feb. 1995, pp. 1138-1140.

[52] C. Nappi et al., "Fiske modes in 0-pi Josephson junctions," *Physical Review B (Condensed Matter and Materials Physics)*, vol. 74, Oct. 2006, pp. 144504-9.